EAST EUROPEAN JOURNAL OF PHYSICS. 2. 4–16 (2025)
DOI: 10.26565/2312-4334-2025-2-01 ISSN 2312-4334

APPLIED SUPERSYMMETRY

V.P. Berezovoj[a], **A.J. Nurmagambetov**[a,b,c*]
[a] *Akhiezer Institute for Theoretical Physics of NSC KIPT, 1 Akademichna St., Kharkiv, 61108, Ukraine*
[b] *V.N. Karazin Kharkiv National University, 4, Svoboda Sq., Kharkiv, 61022, Ukraine*
[c] *Usikov Institute of Radiophysics and Electronics, 12 Ak. Proskury, Kharkiv, 61085, Ukraine*
[*] *Corresponding Author e-mail: ajn@kipt.kharkov.ua*
Received March 1, 2025; revised April 30, 2025; accepted May 8, 2025

Supersymmetry is one of the most important and indispensable ingredients of modern theoretical physics. However, the absence, at least at the time of publishing this review, of experimental verification of supersymmetry in elementary particle/high-energy physics casts doubt on the viability of this concept at the energies achievable at the LHC. The more unexpected are either already experimentally verified or proposed for verification manifestations of supersymmetry at the level of low (condensed matter physics, quantum optics) and medium (nuclear physics) energies where standard quantum mechanics works. Using examples of various systems from completely different areas of physics, we discuss the isospectrality of quantum Hamiltonians, hidden and explicit supersymmetry, the advantages of the supersymmetric quantum mechanics approach and its role in quantum engineering.

Keywords: *Supersymmetric Quantum Mechanics; Isospectrality; Exactly-solvable models*

PACS: 03.65.-w, 12.60.Jv, 02.30.lk

1. INTRODUCTION

On July 3, 2025, we celebrate 100 years since the birth of Dmitry Volkov, academician of the National Academy of Sciences of Ukraine, the founder of one of the scientific schools of the Kharkov Institute of Physics and Technology, one of the inspirers of the creation of the O.I. Akhiezer Institute for Theoretical Physics of NSC KIPT. During his 45-year activity at UFTI-KFTI-NSC KIPT [1] Volkov made a number of discoveries that completely overturned our understanding of fundamental physics. Among them are: the Green-Volkov-Greenberg-Messiah parastatistics [2–5]; Volkov's (jointly with V.N. Gribov) discovery of the "Redge Pole Conspiracy" [6] and the subsequent development of dual models (see the review [7] and references therein); phenomenological Lagrangians of fundamental interactions [8] (and Refs. therein); supersymmetry [9–13]; supergravity [14–16]; supersymmetric quantum mechanics [17–21], spontaneous compactification of extra dimensions [22], twistor approach in supersymmetric theory of particles [23–25], strings [26] and branes [27,28]. Volkov's scientific school members also played an important role in the above-mentioned works, but, of course, he himself set the tone for the research.

Among the above-mentioned scientific inventions of D.V. Volkov, perhaps the main one is the discovery and development of Supersymmetry – a symmetry of a new type, unifying in *supermultiplets* particles of the same quantum numbers, but different statistics. In the end of 60th it was already known that a non-trivial unification of space-time symmetries with gauge symmetries is forbidden within the formalism of the standard quantum field theory [29, 30]. Supersymmetry (the historical retrospective of the discovery and development of supersymmetry is given in [31]) was one of the tools that allowed to overcome this obstacle, which finally led to the appearance of supergravity as a unified theory of space-time and internal (gauge) symmetries. Being a part (to be precise, a low-energy limit) of string theory, the development of supergravity made it possible to take a different look at the Dual Models of strong interactions, and to make two superstring revolutions on their basis (see [32] for a brief review). At present string theory, transformed into M-theory, is considered the most probable candidate for building a unified theory of all fundamental interactions. Although, certainly, the program of construction of the Theory of Everything is still far from its final completion.

It is usually accepted to consider that supersymmetry, growing from particle physics, has a relation to (ultra)high energies, beyond the reachable energies of modern particle colliders. Indeed, the renormalizability property of supersymmetric theories immediately attracted the attention of theorists in the field of high energy physics. But the absence of experimental evidence of supersymmetry on the LHC energy scale clearly indicates a strong violation of supersymmetry. The idea about spontaneous supersymmetry breaking on scales of TeVs is not new. In order to investigate the properties of the supersymmetric vacuum and spontaneous supersymmetry breaking Witten [18, 19] initiated the development of supersymmetric quantum mechanics [17], which was a significant step for the application of supersymmetry in low- and medium-energy physics.

Nowadays Supersymmetry [9–13] plays an important role not only in the world of elementary particle physics, but also in nuclear, solid states and condensed matter physics, quantum mechanics, quantum optics and many other areas of contemporary physics. In this brief review we are aimed at pointing out some features of supersymmetry in

Cite as: V.P. Berezovoj, A.J. Nurmagambetov, East Eur. J. Phys. 2, 4 (2025), https://doi.org/10.26565/2312-4334-2025-2-01

the description of various physical systems, which favourably distinguish this approach from the conventional ones. To recap supersymmetric quantum mechanics (SQM), the approach we promote to describe quantum objects, in Section 2 we recall main points of the construction of isospectral quantum-mechanical Hamiltonians within the standard and extended schemes. In Section 3 we give examples of models from different areas of physics in which supersymmetry is hidden. On the contrary, in Section 4 we consider the situation with exact supersymmetry of stationary Hamiltonians and outcomes arising therefrom. The recently obtained non-trivial connection of CPT-invariant stationary and PT-invariant non-stationary supersymmetric Hamiltonians is discussed in Section 5. Application of the SQM technique for open quantum systems with mixed states and the Lindbladian dynamics of the density matrix is the subject of Section 6. Conclusions contain a brief discussion on the results and further directions of studies.

2. A BRIEF RECAP OF SUPERSYMMETRIC QUANTUM MECHANICS

Let's refine main steps in constructing supersymmetric Hamiltonians. We can follow the factorization method proposed by Dirac and Schrödinger in the mid of 20th of the last century. For the sake of simplicity, we will apply the Dirac-Schrödinger formalism to one-dimensional stationary Hamiltonians, when generally the Hamiltonian operator is presented by

$$H_0 = -\frac{d^2}{dx^2} + V_0(x). \tag{1}$$

According to the formalism, one presents the initial Hamiltonian (1) as

$$H_0 = A^\dagger A + \epsilon, \tag{2}$$

with an analog of the creation/annihilation operators

$$A = \frac{d}{dx} + \beta(x), \qquad A^\dagger = -\frac{d}{dx} + \beta(x). \tag{3}$$

The unknown function $\beta(x)$, entering eq. (3), can be found from the Riccati equation

$$-\frac{d}{dx}\beta(x) + \beta^2(x) = V_0(x) - \epsilon. \tag{4}$$

Though this construction is general, and can be applied to any quantum-mechanical Hamiltonian, the general solution to the Riccati equation is absent in the analytic form. Put it differently, one cannot resolve eq. (4) for an arbitrary potential $V_0(x)$, as well as the Schrodinger equation with Hamiltonian (1).

However, there is a set of quantum-mechanical potentials, for which the exact solutions to the Riccati equation exist. These potentials are referred to as exactly-solvable potentials of Quantum Mechanics (QM). And in this case, we can apply the factorization scheme and determine the operators (3) and the factorization energy ϵ explicitly [33].

But it is not the end of the story. In 1984 Mielnik [34] proposed the way of constructing a new Hamiltonian from the original one, if a particular solution to the Riccati equation has known (see [35]). If we denote this particular solution as $\beta_0(x)$, then the new Hamiltonian will receive the structure of

$$H_1 = AA^\dagger + \epsilon = -\frac{d^2}{dx^2} + V_1(x) \tag{5}$$

with the new potential

$$V_1(x) = V_0(x) + 2\frac{d}{dx}\beta_0(x). \tag{6}$$

The new potential can be absolutely different in shape. However, the spectra of Hamiltonians H_0 and H_1 turn out to be related to each other via the so-called intertwining relations:

$$H_1 A = A H_0, \qquad H_0 A^\dagger = A^\dagger H_1. \tag{7}$$

When the starting Hamiltonian H_0 is an exactly-solvable one, we can choose

$$\beta_0 = -\frac{\varphi_\epsilon'(x)}{\varphi_\epsilon(x)}, \tag{8}$$

and the still arbitrary factorization energy ϵ becomes a part of the spectrum of one of the paired Hamiltonians. Specifically, as $\epsilon < E_0$ (where E_0 is the ground state energy of H_0), the factorization energy is the ground state energy of the new Hamiltonian H_1. As a result, the intertwined Hamiltonians H_0 and H_1 are (almost) isospectral; their spectra are different just in the ground energy state (see Figure 1).

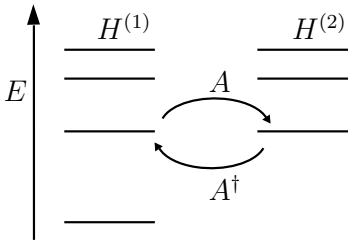

Fgure 1. Schematic spectra of two intertwined Hamiltonians related by (7). Here $H^{(1)} \equiv H_1$, $H^{(2)} \equiv H_0$.

So far, we did not even mention Supersymmetry. However, there is a very close connection [18,36] between operators A and $A^\dagger$ of (3) and the so-called supercharges Q and $Q^\dagger$ forming the part of the minimal Supersymmetry algebra:[1]

$$\left\{Q, Q^\dagger\right\} = H. \tag{9}$$

Then, the paired from the point of view of relations (7) Hamiltonians form the so-called *supermultiplet*. Since properties of a (super)multiplet members have to be the same, it is not surprising that the spectra of the Hamiltonians-superpartners are (almost) the same. It is important to note, the difference in the spectra of the superpartner Hamiltonians in the ground state signals the exact supersymmetry. Restoring the complete equivalence between two spectra corresponds to the supersymmetry breaking [18].

One may wonder, does the presence of Supersymmetry turn out to be so important? We know that experimentally Supersymmetry is still a hidden symmetry of the Nature. However, the fact of absence of superpartners in the realm of particle physics tells us, first of all, about the breaking the Supersymmetry on the LHS action scale. So that, Supersymmetry (SUSY) may be hidden, and this fact can be illustrated by several examples.

3. SYSTEMS WITH HIDDEN SUSY

First example of hidden isospectrality is borrowed from gravitational physics. It is well known that gravitational waves are spin-2 fluctuations over a gravitational background. If, for simplicity, the non-trivial background is chosen to be that of a Schwarzschild black hole, it is determined by the so-called red-shift factor $f(r)$. In the linear approximation, dynamics of spin-2 fluctuations h_s over the Schwarzschild gravitational background is determined by a Schrödinger-type equation [37, 38]

$$\left[\frac{\partial^2}{\partial r_*^2} + \omega^2 - V_s(r)\right] h_s = 0 \tag{10}$$

with the Wheeler coordinate $r_* \in (-\infty, +\infty)$; $s = \pm 2$. The effective potential of the axial perturbations over the background metric (linearly polarized gravitational waves) comes as follows:

$$V_{+2}(r) = -\frac{3f(r)\,\partial_r f(r)}{r} + l(l+1)\frac{f(r)}{r^2}. \tag{11}$$

For the circularly polarized gravitational waves the effective potential becomes

$$V_{-2}(r) = \frac{2f(r)}{r^3}\frac{9M^3 + 3c^2Mr^2 + c^2(1+c)r^3 + 9M^2cr}{(3M+cr)^2}, \quad c = \frac{l(l+1)}{2} - 1. \tag{12}$$

Apparently, in eqs. (11)-(12) l are integers, starting from $l = 2$.

If we insert into eqs. (11) and (12) the red-shift factor for the Schwarzschild black hole, $f(r) = 1 - r_+/r$, we encounter the difference between the effective potentials from (11) and (12). However, the effective Hamiltonians are (almost) isospectral, that can be find from the analysis of the effective potential shapes. (See Figure 2.) There are a lot of debates on the origin of such an isospectrality. It is shown for simple backgrounds [40]; for more exotic configuration of gravitational field the approach fails [41].

Another example of dealing with physical systems with hidden SUSY comes from Quantum Optics. Quantum Optics by itself describes the natural interaction of bosonic (photons) and fermionic (electrons) subsystems of a medium. In the space of parameters of the light-matter interaction it may arise the Bose/Fermi Duality, that transforms, under some

[1] We will return to the specifics of Supersymmetric Quantum Mechanics in Section 4 in more detail.

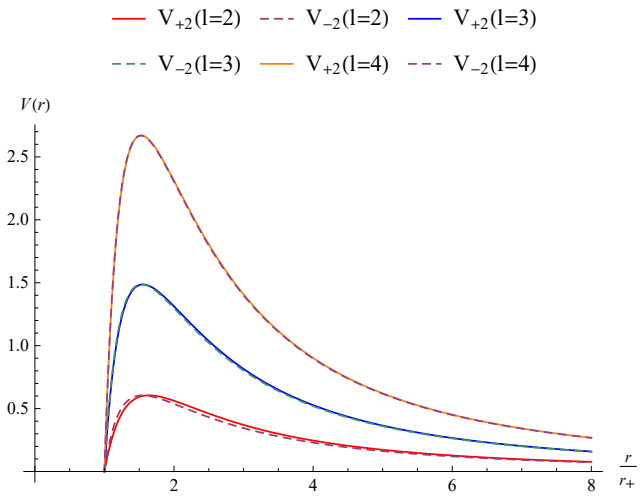

Fgure 2. The shapes of effective potentials for axial and polar spin-2 perturbations over the Schwarzschild background. Borrowed from Ref. [39].

specific conditions, into SUSY [42]. Following [42], let's consider the generalized Rabi model, which is determined by the following Hamiltonian describing a 2-level system interacting with a monochromatic wave:

$$H = \hbar\omega a^{\dagger}a + \frac{\Delta}{2}\sigma_z + g_1\left(a^{\dagger}\sigma_- + a\sigma_+\right) + g_2\left(a^{\dagger}\sigma_+ + a\sigma_-\right). \tag{13}$$

In (13), Δ is the levels gap; ω is the boson field frequency; $a^{\dagger}$ and a are the bosonic ladder operators; and, finally, $g_{1,2}$ are arbitrary constants of the light-matter interaction.

In framework of Quantum Optics, the generalized model with Hamiltonian (12) describes the dipole interaction of a monochromatic wave with the bi-level emitter. In the limit of zero-valued constants of interaction, the considered generalized model turns into the Jaynes-Cummings model. When two constants are the same, we get the Rabi model. If one of the interaction constants is small (say, $g_2 \to 0$), the near-resonant consideration (at $\omega \sim \Delta$) corresponds to the rotating-wave approximation (RWA). In the strong interaction constants regime both interaction terms (co- and contra-rotating) should be taken into account.

As it has been proved in [42], SUSY is a symmetry of the generalized Rabi model under the following condition:

$$g_1^2 - g_2^2 = \Delta \cdot \omega. \tag{14}$$

Then, the supercharge is realized by 4×4 matrix

$$Q = \begin{pmatrix} 0 & \hat{q} \\ 0 & 0 \end{pmatrix}, \qquad \hat{q} = \begin{pmatrix} g_1/\sqrt{\omega} & \sqrt{\omega}\,a \\ \sqrt{\omega}\,a & g_2/\sqrt{\omega} \end{pmatrix}. \tag{15}$$

As usual for SUSY (cf. eq. (9)),

$$\left\{Q, Q^{\dagger}\right\} = H. \tag{16}$$

For $g_1 = g_2$, SUSY is realized with $\Delta = 0$. And Hamiltonian (12) turns into the standard Harmonic Oscillator with a shift.

The next example comes from Condensed Matter Physics. It turns out that SUSY is a hidden symmetry in a topological insulator with Josephson junctions [43]. Such a system can be described by the Bogoliubov-de Gennes equations, which, after the appropriate simplifications (see [43] for details), can be reduced to the system of differential equations (here and in what follows we use $\partial_x \equiv d/dx$ and $\partial_x^2 \equiv d^2/dx^2$)

$$\begin{aligned} \left(E + iv\partial_x\right) f(x) + \Delta(x)\phi(x) &= 0, \\ \left(E - iv\partial_x\right) \varphi(x) + \Delta^{*}(x) f(x) &= 0. \end{aligned} \tag{17}$$

In (17), E is the energy of moving with the velocity v in the positive x direction spinning mode; $\Delta(x)$ is the complex energy gap. It is easy to transform this system of equations in the equation of Witten's Supersymmetric Quantum Mechanics [18]

$$E^2\psi(x) = \left(-v^2\partial_x^2 + \hat{W}^2(x) + iv\sigma_z\frac{\partial\hat{W}(x)}{\partial x}\right)\psi(x), \quad \sigma_z = \begin{pmatrix} 1 & 0 \\ 0 & -1 \end{pmatrix}, \tag{18}$$

where $\psi(x)$ is the spinning mode state

$$\psi(x) = \begin{pmatrix} f(x) \\ \varphi(x) \end{pmatrix} \tag{19}$$

and the *superpotential* $\hat{W}(x)$ is given by

$$\hat{W}(x) = \begin{pmatrix} 0 & \Delta(x) \\ \Delta^*(x) & 0 \end{pmatrix}. \tag{20}$$

This series of examples could be continued by notable systems with hidden SUSY in Quantum Mechanics [44], nuclear physics [45] and mesoscopy [46].

4. EXACTLY-SOLVABLE MODELS OF SQM WITH MULTI-WELL POTENTIALS

In this part of the review, we will focus on the supersymmetric generalization of the Mielnik [34] construction and its extension to N=4 Supersymmetric Quantum Mechanics [47–49].

First of all, let's describe the technique behind the deformation of the potential shape. Looking at Figure 1, one may notice that the original and the paired Hamiltonians are different in spectra by just one level. And if this new additional level has the energy less than the ground state energy of the original Hamiltonian, it defines the vacuum state of the paired Hamiltonian with new potential (6). To keep the coincident part of the both Hamiltonians spectra, the shape of the new potential shall be changed. The level of deformation depends on the interplay between the unfixed parameters that naturally arise in this scheme upon the definition of new, non-normalized, wave function $\varphi_\epsilon(x)$, corresponding to the new ground state with the factorization energy ϵ. For instance, the Harmonic Oscillator potential describes the system with one potential well; its deformation may potentially form another well. So that, by controlled adding an additional level, we are able to get the (almost) isospectral quantum mechanical system with two-well potential. However, the clear impact of Quantum Mechanics in this case will consists in possible *tunneling effects* between the wells of the paired to the Harmonic Oscillator potential. Further, by adding a new level, lower than the ground level of the Hamiltonian H_1, one can form another, paired to H_1, Hamiltonian H_2 with another potential, the shape of which will be different from the potential V_1. Here, the interplay between parameters of the solutions may result as in a two-well as well as in a three-well potential of different (symmetric or asymmetric) shapes. In the latter case, one is able to study more complex tunneling effects that provides a lot of possibilities to control quantum-mechanical processes.

Let us to be more specific and to consider the appearance of the controlling parameters from logic of the construction of supersymmetric Hamiltonians.

Consider to this end the factorization of a static 1D Hamiltonian $H_+ = -\partial_x^2 + V_+(x)$ by two operators (*supercharges*) $Q^\dagger$, Q (analogs of operators A and $A^\dagger$ in Section 2):

$$H_+ = Q^\dagger Q, \qquad Q^\dagger = -\partial_x + \frac{1}{2}\partial_x W(x), \quad Q = \partial_x + \frac{1}{2}\partial_x W(x). \tag{21}$$

The *superpotential* $W(x)$ [18] (analog of the function $\beta(x)$ of Section 2) is determined from the Riccati equation

$$\left(\frac{1}{2}\partial_x W(x)\right)^2 \mp \frac{1}{2}\partial_x^2 W(x) = V_\pm(x), \tag{22}$$

where V_- is the potential of the paired to H_+ Hamiltonian $H_- = -\partial_x^2 + V_-(x) = QQ^\dagger$. The isospectrality of Hamiltonians $H_\pm$ is realized modulo the H_+ ground state (the spectrum of the H_- Hamiltonian begins with the first excited level of H_+)

$$\Psi_0(x) = N_0\, e^{-\frac{1}{2}W(x)}, \qquad E_0 = 0. \tag{23}$$

Note, that the zero energy value in the ground state of the initial Hamiltonian is the hallmark of supersymmetry: any of supersymmetric models have a non-negative energy. And if two paired by the supercharges Hamiltonians have the spectrums different just by the ground state, the supersymmetry is exact.

Now, let's figure out the appearance of a free additional parameter in the approach. Suppose to this end, there exists the factorization of H_- by other supercharges

$$H_- = \tilde{Q}\tilde{Q}^\dagger, \qquad \tilde{Q} = \partial_x + f(x), \quad \tilde{Q}^\dagger = -\partial_x + f(x). \tag{24}$$

From $H_- = -\partial_x^2 + V_-(x)$ it comes

$$f^2(x) + \partial_x f(x) = \left(\frac{1}{2}\partial_x W(x)\right)^2 + \frac{1}{2}\partial_x^2 W(x).$$

And if $W(x)$ is known, $f(x)$ is determined by [34, 35]

$$f(x) = \frac{1}{2}\partial_x W(x) - \frac{e^{-W(x)}}{\lambda + \int_x^\infty dz\, e^{-W(z)}} \equiv \frac{1}{2}\partial_x W(x) - \phi(x), \tag{25}$$

with $\phi(x)$ to be a general solution, with an integration constant λ, to the equation

$$\partial_x \phi(x) - \phi^2(x) + \phi(x)\partial_x W(x) = 0. \tag{26}$$

What will happen when we will construct the Hamiltonian $\tilde{H}_+ = \tilde{Q}^\dagger \tilde{Q}$? Explicitly,

$$\tilde{H}_+ = \tilde{Q}^\dagger \tilde{Q} = -\partial_x^2 + V_+ + 2\partial_x \phi(x), \quad \phi(x) = \frac{e^{-W(x)}}{\lambda + \int_x^\infty dz\, e^{-W(z)}}, \tag{27}$$

and we have constructed the new potential

$$\tilde{V}_+ = V_+ + 2\partial_x \phi(x). \tag{28}$$

Apparently, $\tilde{H}_+ \neq H_+$ since the potential $\tilde{V}_+$ in no way equal to the potential V_+. However, the spectra of $\tilde{H}_+$ and H_+ are the same *modulo the ground state*.

Indeed, by construction, the Hamiltonians H_+ and $\tilde{H}_+$ becomes (almost) isospectral, via their parent Hamiltonian H_-. Definitely, one can write

$$\tilde{H}_+ \tilde{Q}^\dagger = \left(\tilde{Q}^\dagger \tilde{Q}\right)\tilde{Q}^\dagger = \tilde{Q}^\dagger \left(\tilde{Q}\tilde{Q}^\dagger\right) = \tilde{Q}^\dagger H_-, \tag{29}$$

and this relation is similar to the one of intertwining relations (7). According to (29), the eigenstates of $\tilde{H}_+$ are determined by $|\tilde{\psi}_i^{(+)}\rangle = \tilde{Q}^\dagger |\psi_i^{(-)}\rangle$, where $|\psi_i^{(-)}\rangle$ are the eigenstates of H_-. So that, the energies (eigenvalues of $\tilde{H}_+$) will be given by E_i, $i = 1, \ldots, N$ (in the case of finite dimensional and discrete spectrum). However, the ground state $\tilde{Q}|\tilde{\psi}_0^{(+)}\rangle = 0$ is absent in the spectrum of $\tilde{H}_+$ and has to be added by hands [34]. In the coordinate representation, the corresponding wave function $\tilde{\Psi}_0$ is

$$\tilde{\Psi}_0 = \tilde{N}_0\, e^{-\frac{1}{2}W(x)} e^{\int_0^x dz\, \phi(z)}. \tag{30}$$

One may straightforwardly check that $\tilde{H}_+ \tilde{\Psi}_0 = 0$. So that the spectra (eigenvalues) of $\tilde{H}_+$ and H_+ become identical after adding the ground state $\tilde{\Psi}_0$.

The appearance of the integration constant λ in the potential $\tilde{V}_+$ and in the ground state wave function $\tilde{\Psi}_0$ becomes important for engineering the potential shape. Indeed, by developing the above-mentioned method in the framework of N=4 SQM, we can use both the ground state wave function and the whole spectrum of states in the construction of isospectral Hamiltonians. Moreover, we can use for this purpose even non-normalized wave functions of the starting Hamiltonian, which will correspond to addition of new levels with energies smaller than the ground state energy in the starting Hamiltonian spectrum. (See [50–52] for details.) This leads to a change of $\phi(x)$, and hence of the integration constant λ in (27). Different values of λ define different shapes of the potential: one-well or multi-well, symmetric or asymmetric with respect to the reflection operation. All these properties provide ample opportunities to study quantum mechanical processes and even to control them [50–52].

As an example of such controlling let us present results of modelling a wave package behavior in a symmetric and a non-symmetric two-well potentials for isospectal Hamiltonians, Figure 3 and Figure 4. Due to the difference in probabilities of the ground and first and second excitation levels in different wells of symmetric and asymmetric potentials, the probability flow of wave packages prepared with the corresponding energies essentially varies. It models the behavior of a *quantum diode*.

When the number of wells in the isospectral Hamiltonian potential becomes equal to three, the situation becomes more complicated. Here, with tunneling process, one can model properties of a quantum transistor, with different values of "current" flow in different wells, see Figure 5.

One can generalized the description with adding the temporal dependence. For instance, it could be an external periodic driving force that, in real devices, is reproduced by a laser EM field. The interplay of parameters in the extended by the external field frequency set allows one to reach the phenomenon of the so-called Coherent Tunneling Destruction (CTD) [53], when without changing the quantum character of the system it becomes possible to localize the initial wave packet in one of the wells. As an illustration of the CTD, in Figure 6 we present the data of numerical simulations borrowed from Ref. [52].

Hence, the formalism of Supersymmetric Quantum Mechanics turns out to be helpful in modelling different processes such as tunneling, particles flow, diffusion and so on, in the controllable manner. The latter is achieved by the exactly-solvable character of the models in hands, when the Green's functions are constructed out the explicitly known analytic expressions for the wave functions. Thus, evolution in such systems becomes, if not deterministic, then very predictable.

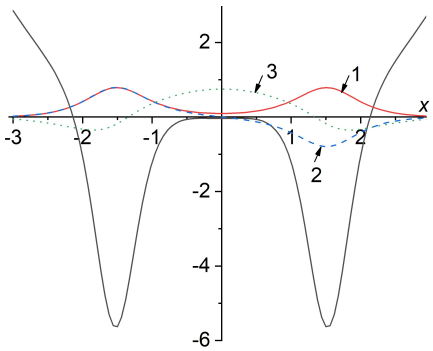

Fgure 3. The wave functions of the first three levels in different wells of a symmetric two-well potential; numeration starts with the ground level. See Ref. [52] for details.

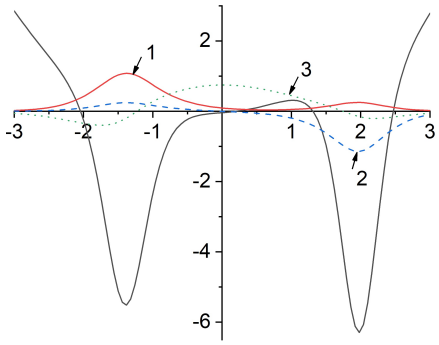

Fgure 4. The wave functions of the first three levels in different wells of an asymmetric two-well potential. See Ref. [52] for details.

5. CPT/PT-INVARIANT HAMILTONIANS CORRESPONDENCE

As we have noted in Section 2, the spectra of paired Hamiltonians are connected by the intertwining relations (7). Their role becomes even more important for non-stationary Supersymmetric Quantum Mechanics, as well as in the case of quantum description of open systems. The following section is devoted to the supersymmetric Lindbladian dynamics. Here we focus on a non-trivial correspondence between CPT and PT invariant models.

First, let's recall the generalization of the intertwining relations (29) to the non-stationary SQM:

$$\left(i\partial_t - H_-\right)\tilde{Q} = \tilde{Q}\left(i\partial_t - \tilde{H}_+\right). \tag{31}$$

H_- is the paired to H_+ and $\tilde{H}_+$ Hamiltonian (cf. Section 4). For the non-stationary case, H_+ becomes the part of the complete Schrödinger operator acting on a time-dependent wave function

$$\left(H_+ - i\partial_t\right)\psi^{(+)}(x,t) = 0, \qquad H_+ = -\partial_x^2 + V_+(x,t). \tag{32}$$

In the general case, the potential V_+ also depends on the time parameter. The way of H_+ factorization is implemented as in eq. (21), $H_+ = Q^\dagger Q$, but supercharges Q and $Q^\dagger$ now include a time-dependent superpotential $W(x,t)$. The Hamiltonian H_- is realized as $H_- = QQ^\dagger$.

Just as before (cf. equation (24)), we will require another factorization of H_- in terms of $\tilde{Q}$ and $\tilde{Q}^\dagger$ supercharges, which, as now required, must be [54–58]

$$\tilde{Q} = l(t)\left(\partial_x + f(x,t)\right), \qquad f(x,t) = \frac{1}{2}\partial_x W(x,t) - \phi(x,t). \tag{33}$$

The functions $l(t)$ and $\phi(x,t)$ are generally complex-valued functions, and this fact will be important in what follows. And the use of the intertwining relation (31) makes it possible to derive the relation [54, 55] between the new and the old potentials,

$$\tilde{V}_+(x,t) = V_+(x,t) + 2\partial_x\phi(x,t) - i\partial_t \ln l(t). \tag{34}$$

The function $\phi(x,t)$ is restricted to satisfy

$$\partial_x\left[f^2(x,t) - \partial_x f(x,t) - \tilde{V}_+(x,t)\right] - i\partial_t f(x,t) = 0, \tag{35}$$

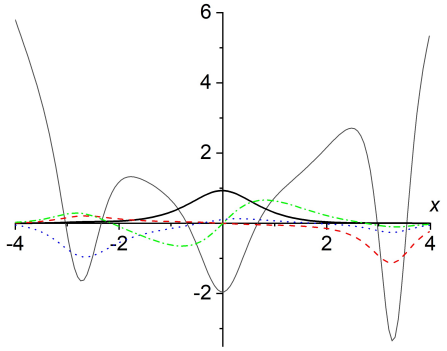

Fgure 5. The wave functions of the first three levels in different wells of an asymmetric three-well potential. See Ref. [52] for details.

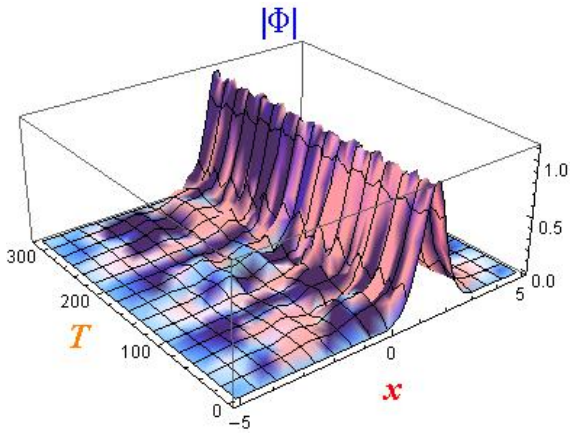

Fgure 6. Numerical simulation of evolution of the Gaussian wave packet $\Phi(x,T)$ in the external periodic driving force. We refer the reader to [52] for details.

and, if we will require the real-valued spectrum of $\tilde{H}_+$, the following constraints should hold:

$$\partial_t \ln|l(t)|^2 = -4\partial_x\left[\Im\mathrm{m}\,\phi(x,t)\right] \qquad \rightsquigarrow \qquad \partial_x^2\left[\Im\mathrm{m}\,\phi(x,t)\right] = 0. \tag{36}$$

From the relations (36) it becomes clear that for a non-trivial $l(t)$ it is required a complex-valued function $\phi(x,t)$.

Now let us associate the stationary Hamiltonian (27) with its time-dependent cousin. Recall, we have an arbitrary integration constant λ in the construction of $\tilde{H}_+$ (cf. eqs. (27)). However, *changing the λ does not affect the spectrum*, affecting the potential and wave functions instead. Therefore, we can instantly change the λ in its value, within its range, determined by relation

$$\lambda + \int_x^\infty dz\, e^{-W(x)} \neq 0, \tag{37}$$

and still have the steady spectrum. Hence, we can relate any instant λ changing to some unique value of the time parameter. Smooth changes will form a function of time $\lambda(t)$ after that [59].

The so introduced time-dependence of λ induces the time-dependence of $\phi(x)$ function of (25) (see [59]):

$$\phi(x,t) = \frac{e^{-W(x)}}{\lambda(t) + \int_x^\infty dz\, e^{-W(z)}}. \tag{38}$$

Then, the time dependence of the $\tilde{H}_+$ ground state wave function,

$$\tilde{\Psi}_0(x,t) = \tilde{N}_0 e^{-\frac{1}{2}W(x)} e^{\int_0^x dz\,\phi(z,t)}, \tag{39}$$

can be treated as a time-dependent geometric phase, i.e.,

$$\tilde{\Psi}_0(x,t) = \tilde{N}_0 e^{-\frac{1}{2}W(x)} e^{i\Phi(x,t)}, \quad i\Phi(x,t) = \int_0^x dz\,\phi(z,t). \tag{40}$$

Wave functions with time-dependent geometric phase naturally appear in quantum systems with time-dependent boundary conditions. (See, e.g., Ref. [60].) And interesting consequence of introducing time-dependent boundary conditions is introducing the field-compensator in time direction (a vector field with one non-trivial component, to make the formalism close to the standard theory of gauge fields).

To find the Hamiltonian $\tilde{H}_+$ paired to a *stationary* Hamiltonian H_+,

$$\left(H_+ - i\partial_t\right)\psi(x,t) = 0, \qquad H_+ = -\partial_x^2 + V_+(x), \tag{41}$$

with the *stationary* wave functions $\psi(x,t) = e^{-i\varepsilon t}\psi_\varepsilon(x)$ and independent on time potential $V_+(x)$ in the situation with time-dependent integration function $\lambda(t)$, one needs to form an analog of the covariant derivative in time direction: $D_t = \partial_t + A_t$. Then, the *non-stationary* Hamiltonian $\tilde{H}_+$ obeys the complete Schrödinger equation [59]

$$\left(\tilde{H}_+ - iD_t\right)\Psi(x,t) = 0, \qquad \tilde{H}_+ = -\partial_x^2 + \tilde{V}_+(x,t), \tag{42}$$

and two (almost)isospectral potentials $V_+(x)$ and $\tilde{V}_+(x,t)$ are related to each other as

$$\tilde{V}_+(x,t) = V_+(x) + 2\partial_x\phi(x,t) + \frac{i\partial_t\lambda}{\lambda(t) + \int_x^\infty dz\,|\Psi_0(z)|^2}\,. \tag{43}$$

The compensator field is given by

$$A_t(t) = \frac{\partial_t\lambda(t)}{\lambda(t) + \int_x^\infty dz\,|\Psi_0(z)|^2}, \tag{44}$$

so that the paired non-stationary Hamiltonian $\tilde{H}_+$ becomes complex-valued! In general, the Hermitian condition is not preserved, the energy is not conserved, so that such a Hamiltonian may be used for the description of either an open system or a system with dissipation. (See [59] for a brief discussion on possible applications of complex-valued non-stationary Hamiltonians, and Appendix therein.)

It is important to note that dealing with a real-valued potential to get real-valued eigenvalues of the Hamiltonian is an excess requirement [61–63]. Instead, one may consider complex-valued Hamiltonians with real spectrum, which after [62, 63] are called as PT-invariant Hamiltonians. The requirement to have a real-valued potential $\tilde{V}_+(x,t)$ leads to the following relation between the function $\phi(x,t)$ and the "compensator" field:

$$\mathfrak{Re}A_t(x,t) = 2\partial_x\left(\mathfrak{Im}\,\phi(x,t)\right). \tag{45}$$

Hence, in the case of PT-invariant Hamiltonians, $\phi(x,t)$ should be complex-valued to supply the non-triviality of the compensator $A_t(x,t)$. This requirement essentially narrows the class of physical systems to describe. More on the application of complex-valued potentials with complex-valued spectra can be found in Ref. [64].

6. SUPERSYMMETRIC QUANTUM MECHANICS FOR OPEN SYSTEMS

As we have noted in previous sections, the spectra of paired Hamiltonians and their potentials are connected by the intertwining relations (7), (29), (31). They become main relations for the developed in [54–58] non-stationary SQM, as well as in the polynomial (nonlinear, higher derivative) formulation of Supersymmetric Quantum Mechanics [65–68]. The latter approach has been used in extending the SQM to the description of open systems with exchanging the energy with the environment. We have noted that complex-valued Hamiltonians can be potentially used to this end. The gold standard in the description of open quantum systems is the application of the Franke-Gorini-Kossakowski-Lindblad-Sudarshan [69–72] (FGKLS) equation. The supersymmetrization of the FGKLS equation was considered in Ref. [73], and here we closely follow this approach.

The quantum states of an open system are mixed. Thus, one needs to use the density matrix formalism, in which the density matrix operator of a sub-system evolves according to

$$\frac{\partial\rho}{\partial t} = -i\left(H_{\text{eff}}\,\rho - \rho\,H_{\text{eff}}^\dagger\right) + L[\rho]. \tag{46}$$

Here H_{eff} is the effective Hamiltonian (which is not Hermitian in the case), and $L[\rho]$ is the so-called Lindbladian

$$L[\rho] = \sum_j\left(A_j\rho A_j^\dagger - \frac{1}{2}\left[\rho, A_j^\dagger A_j\right]\right). \tag{47}$$

The A_j operators are unspecified, and they may be used to model the influence of the measurement devices on a quantum system. The Lindbladian operator is introduced to evolve pure states into mixed states. So that A_j operators are naturally restricted to provide increasing the entropy

$$S = \text{Tr}\left(-\rho\log\rho\right) \tag{48}$$

upon the evolution of the system.

To construct the supersymmetric version of the FGKLS equation (46), let's introduce the supermultiplet of two paired Hamiltonians

$$\mathcal{H} = \begin{pmatrix} H_+ & 0 \\ 0 & H_- \end{pmatrix} = \begin{pmatrix} -\partial_x^2 + V_+(x) & 0 \\ 0 & -\partial_x^2 + V_-(x) \end{pmatrix}. \tag{49}$$

Following [73] we suppose the super-Hamiltonian to be independent on time.

Isospectrality of H_+ and H_- follows from the intertwining relations (7) (replacing (H_0, H_1) with (H_+, H_-), respectively)

$$AH_+ = H_-A, \qquad H_+A^\dagger = A^\dagger H_-. \tag{50}$$

The supercharges Q and $Q^\dagger$ are constructed out the A, $A^\dagger$ operators:

$$Q = \begin{pmatrix} 0 & A^\dagger \\ 0 & 0 \end{pmatrix}, \qquad Q^\dagger = \begin{pmatrix} 0 & 0 \\ A & 0 \end{pmatrix}. \tag{51}$$

Then, the intertwining relations (50) reflect the conservation of supercharges during the evolution of the system:

$$[\mathcal{H}, Q] = [\mathcal{H}, Q^\dagger] = 0. \tag{52}$$

The full superalgebra is closed by adding the following anti-commutator of supercharges,

$$\{Q, Q^\dagger\} = \mathcal{P}(\mathcal{H}), \tag{53}$$

where, in dependence on the realization of A and $A^\dagger$ by first or higher order derivative operators, $\mathcal{P}(\mathcal{H})$ is a linear or polynomial function of the super-Hamiltonian, respectively. (See [73] and Refs. therein for details.)

Similarly to the super-Hamiltonian $\mathcal{H}$ we can introduce the super-density matrix

$$\mathfrak{P} = \begin{pmatrix} \rho_+ & 0 \\ 0 & \rho_- \end{pmatrix}. \tag{54}$$

Then, the Schrödinger-Liouville equation (for $L[\mathfrak{P}] = 0$) is

$$\frac{\partial}{\partial t}\mathfrak{P} = -i[\mathcal{H}, \mathfrak{P}], \tag{55}$$

and we have to find the analog of intertwining relations (50) for super-partners ρ_+ and ρ_-. We can use the standard definition of the mean value to this end. For the super-Hamiltonian it becomes

$$\langle \mathcal{P}(\mathcal{H}) \rangle = \mathrm{Tr}\,(\mathcal{P}(\mathcal{H})\,\mathfrak{P}) = \mathrm{Tr}\left(\sqrt{\mathcal{P}(\mathcal{H})}\,\mathfrak{P}\,\sqrt{\mathcal{P}(\mathcal{H})}\right) = \mathrm{Tr}(Q\,\mathfrak{P}\,Q^\dagger + Q^\dagger\,\mathfrak{P}\,Q), \tag{56}$$

and the proposed by the authors of Ref. [73] intertwining relations are

$$Q^\dagger\,\mathfrak{P}\,\sqrt{\mathcal{P}(\mathcal{H})} = \sqrt{\mathcal{P}(\mathcal{H})}\,\mathfrak{P}\,Q^\dagger, \qquad Q\,\mathfrak{P}^\dagger\,\sqrt{\mathcal{P}(\mathcal{H})} = \sqrt{\mathcal{P}(\mathcal{H})}\,\mathfrak{P}^\dagger\,Q. \tag{57}$$

Analogous relations can be used for the Lindbladian operator with generally non-Hermitian A_j. For the super-density matrix the Hermiticity condition still holds: $\mathfrak{P} = \mathfrak{P}^\dagger$.

The generalization of (47) to the SQM is apparent: we have to introduce

$$\mathfrak{A}_j = \begin{pmatrix} A_{j+} & 0 \\ 0 & A_{j-} \end{pmatrix} \tag{58}$$

and to form, by use of (54) and (58), the super-Lindbladian operator. The intertwining relations for linear and quadratic in $\mathfrak{A}_j$ combinations (cf. (57)) are:

$$Q^\dagger\,\mathfrak{A}_j\,\sqrt{\mathcal{P}(\mathcal{H})} = \sqrt{\mathcal{P}(\mathcal{H})}\,\mathfrak{A}_j\,Q^\dagger, \qquad Q\,\mathfrak{A}^\dagger\,\sqrt{\mathcal{P}(\mathcal{H})} = \sqrt{\mathcal{P}(\mathcal{H})}\,\mathfrak{A}^\dagger\,Q, \tag{59}$$

$$Q^\dagger \sum_j \mathfrak{A}_j^\dagger\mathfrak{A}_j\,\sqrt{\mathcal{P}(\mathcal{H})} = \sqrt{\mathcal{P}(\mathcal{H})} \sum_j \mathfrak{A}_j^\dagger\mathfrak{A}_j\,Q^\dagger, \qquad Q \sum_j \mathfrak{A}_j^\dagger\mathfrak{A}\,\sqrt{\mathcal{P}(\mathcal{H})} = \sqrt{\mathcal{P}(\mathcal{H})} \sum_j \mathfrak{A}_j^\dagger\mathfrak{A}\,Q. \tag{60}$$

Examples of the application of the formalism can be found in Ref. [73].

7. CONCLUSIONS

In conclusion, let us recall the main advantages of Supersymmetry that make this approach preferable to others.

First, as it has been pointed out in one of the underlying work on Supersymmetry [15], supersymmetric models are super-renormalizable ones: the UV divergency problem, actual for standard field theories including the Standard Model, is completely absent for them. Unfortunately, our Universe is not supersymmetric; but this fact is about the energy scale on which SUSY is broken.

Second, application of Supersymmetry as a tool to investigate various physical models in different regimes and on different energy scales has shown its self-consistency and efficiency. We can just cite a few quotes from the modern literature in favor of this claim. For instance, the authors of Ref. [42] write: " ... optical and condensed matter systems at the SUSY points can be used for quantum information technology and can open an avenue for quantum simulation of the SUSY field theories." In Ref. [74] one can read off: " ... the atomic nucleus ^{195}Pt represents an excellent example of the dynamical U(6/12) supersymmetry. ... certainly the best documented example of the manifestation of dynamical supersymmetry in atomic nuclei." As it comes from reading Ref. [75], the potential of supersymmetry has not yet been definitively revealed, since the author "... brings the attention to the role of supersymmetry in quantum computation and quantum information more broadly, a subject much underexplored." Furthermore, in our studies [50–52] we have noticed the advantages of using the SQM approach, such as full knowledge of the spectrum and explicit analytical expressions for the wave functions, which makes studies of the evolution of quantum systems simple and straightforward, via the exact Green's function. The Coherent Tunneling Destruction and other tunneling effects in multi-well potentials require within the SQM approach a finite number of states (of the order of ten), while the same numerical simulation for potentials constructed by stitching a harmonic oscillator potential requires consideration of hundreds of states.

And finally, here we have shown the perspectives of applying the SQM formalism in studying quantum sytems. Especially in cases closer to the real world [73]. Recently, we have extended the approach to include the temporal dependence into the game [59], that made it possible to relate CPT-invariant stationary Hamiltonians to their PT-invariant non-stationary partners. It opens new avenues in investigations of quantum-mechanical models with complex-valued potentials, having more reach structure of physical phenomena, and being applicable to an essentially wide class of physical systems, including open systems. We expect new non-trivial results along the way and will strive to contribute to exciting intertwining Supersymmetry with quantum realm.

Acknowledgments

We express our sincere gratitude to Dmitry Vasilievich Volkov, who introduced us to the magical world of supersymmetry. We are also grateful to M.I. Konchatnij for the pleasant collaboration, which resulted in many important new results. The work of A.J.N. is partly carried out as a part of the COST initiative CA22113 – Fundamental challenges in theoretical physics (THEORY-CHALLENGES).

Conflicts of interest

The authors declare no conflict of interest.

ORCID


A.J. Nurmagambetov, https://orcid.org/0000-0001-5175-5997

REFERENCES

[1] S.I. Volkova, and A.J. Nurmagambetov, editors, *Dmitry Vasilievich Volkov. Articles, essays, memoirs*, (Tymchenko A.N. Publishing House, Kharkov, 2007) (in Russian).

[2] H.S. Green, Phys. Rev. **90**, 270 (1953). https://doi.org/10.1103/PhysRev.90.270

[3] D.V. Volkov, Sov. JETP, **9**, 1107 (1959); **11**, 375 (1960).

[4] O.W. Greenberg, Phys. Rev. Lett. **13**, 598 (1964). https://doi.org/10.1103/PhysRevLett.13.598

[5] O.W. Greenberg, and A.M.L. Messiah, Phys. Rev. **136**, B248 (1964). https://doi.org/10.1103/PhysRev.136.B248

[6] V.N. Gribov, and D.V. Volkov, Sov. Phys. JETP, **17**, 720 (1963).

[7] D.V. Volkov, "Quarks as a consequence of Duality," (A Reviewed Lecture), Preprint JINR, P2-8765, 1-50, (1975). (in Russian).

[8] D.V. Volkov, Fiz. Elem. Chast. Atom. Yadra, **4**, 3 (1973).

[9] Y.A. Golfand, and E.P. Likhtman, JETP Lett. **13**, 323 (1971). http://dx.doi.org/10.1142/9789814542340_0001

[10] D.V. Volkov, and V.P. Akulov, JETP Lett. **16**, 438 (1972). http://dx.doi.org/10.1007/BFb0105270

[11] D.V. Volkov, and V.P. Akulov, Phys. Lett. B, **46**, 109 (1973). http://dx.doi.org/10.1016/0370-2693(73)90490-5

[12] J. Wess, and B. Zumino, Phys. Lett. B, **49**, 52 (1974). http://dx.doi.org/10.1016/0370-2693(74)90578-4

[13] J. Wess, and B. Zumino, Nucl. Phys. B, **70**, 39 (1974). http://dx.doi.org/10.1016/0550-3213(74)90355-1

[14] D.V. Volkov, and V.A. Soroka, JETP Lett. **18**, 312 (1973).

[15] S. Deser, and B. Zumino, Phys. Lett. B, **62**, 335 (1976). http://dx.doi.org/10.1016/0370-2693(76)90089-7

[16] D.Z. Freedman, P. van Nieuwenhuizen, and S. Ferrara, Phys. Rev. D, **13**, 3214 (1976). http://dx.doi.org/10.1103/PhysRevD.13.3214

[17] H. Nicolai, J. Phys. A, **9**, 1497 (1976). http://dx.doi.org/10.1088/0305-4470/9/9/010

[18] E. Witten, Nucl. Phys. B, **188**, 513 (1981). https://doi.org/10.1016/0550-3213(81)90006-7

[19] E. Witten, J. Diff. Geom. **17**, 661 (1982). https://doi.org/10.4310/jdg/1214437492

[20] D.V. Volkov, V.P. Akulov, and A.I. Pashnev, Ukr. Fiz. Zh. (Russ.Ed.), **30**, 1263 (1985).

[21] D.V. Volkov, A.I. Pashnev, V.A. Soroka, and V.I. Tkach, JETP Lett. **44**, 70-72 (1986).

[22] D.V. Volkov, and V.I. Tkach, JETP Lett. **32**, 668 (1980).

[23] D.V. Volkov, and A.A. Zheltukhin, Lett. Math. Phys. **17**, 141 (1989). https://doi.org/10.1007/BF00402328

[24] D.P. Sorokin, V.I. Tkach, and D.V. Volkov, Mod. Phys. Lett. A, **4**, 901 (1989). https://doi.org/10.1142/S0217732389001064

[25] D.P. Sorokin, V.I. Tkach, D.V. Volkov, and A.A. Zheltukhin, Phys. Lett. B, **216**, 302 (1989). https://doi.org/10.1016/0370-2693(89)91119-2

[26] D.V. Volkov, and A.A. Zheltukhin, Nucl. Phys. B, **335**, 723 (1990). https://doi.org/10.1016/0550-3213(90)90527-K

[27] I.A. Bandos, D.P. Sorokin, M. Tonin, P. Pasti, and D.V. Volkov, Nucl. Phys. B, **446**, 79 (1995). https://doi.org/10.1016/0550-3213(95)00267-V

[28] I.A. Bandos, D.P. Sorokin, and D. Volkov, Phys. Lett. B, **352**, 269 (1995). https://doi.org/10.1016/0370-2693(95)00506-G

[29] W.D. McGlinn, Phys. Rev. Lett. **12**, 467 (1964). https://doi.org/10.1103/PhysRevLett.12.467

[30] S. R. Coleman and J. Mandula, Phys. Rev. **159**, 1251 (1967). https://doi.org/10.1103/PhysRev.159.1251

[31] G.L. Kane, and M. Shifman, *The Supersymmetric World:The Beginnings of the Theory*, (World Scientific Publishing, 2000).

[32] String Theory, https://en.wikipedia.org/wiki/String_theory

[33] L. Infeld and T. E. Hull, Rev. Mod. Phys. **23**, 21 (1951). https://doi.org/10.1103/RevModPhys.23.21

[34] B. Mielnik, J. Math. Phys. **25**, 3387 (1984). https://doi.org/10.1063/1.526108

[35] N.G. van Kampen, J. Stat. Phys. **17**, 71 (1977). https://doi.org/10.1007/BF01268919

[36] L.E. Gendenshtein, and I.V. Krive, Sov. Phys. Usp. **28**, 645 (1985). https://doi.org/10.1070/PU1985v028n08ABEH003882

[37] T. Regge, and J.A. Wheeler, Phys. Rev. **108**, 1063 (1957). https://doi.org/10.1103/PhysRev.108.1063

[38] F.J. Zerilli, Phys. Rev. Lett. **24**, 737-738 (1970). https://doi.org/10.1103/PhysRevLett.24.737

[39] A.M. Arslanaliev, and A.J. Nurmagambetov, MDPI Physics, **3**, 17 (2021). https://doi.org/10.3390/physics3010004

[40] K. Glampedakis, A.D. Johnson, and D. Kennefick, Phys. Rev. D, **96**, 024036 (2017). https://doi.org/10.1103/PhysRevD.96.024036

[41] D. Li, A. Hussain, P. Wagle, Y. Chen, N. Yunes, and A. Zimmerman, Phys. Rev. D, **109**, 104026 (2024). https://doi.org/10.1103/PhysRevD.109.104026

[42] M. Tomka, M. Pletyukhov, and V. Gritsev, Sci Rep. **5**, 13097 (2015). https://doi.org/10.1038/srep13097

[43] A.V. Galaktionov, Phys. Rev. B, **101**, 134501 (2020). https://doi.org/10.1103/PhysRevB.101.134501

[44] E. D'Hoker, and L. Vinet, Phys. Lett. B, **137**, 72 (1984), https://doi.org/10.1016/0370-2693(84)91108-0

[45] F. Iachello, Phys. Rev. Lett. **44**, 772 (1980). https://doi.org/10.1103/PhysRevLett.44.772

[46] A.F. Andreev, and M.Yu. Kagan, JETP, **66**, 504 (1987).

[47] A.I. Pashnev, Theor. Math. Phys. **69**, 1172 (1986). https://doi.org/10.1007/BF01037879

[48] V.P. Berezovoi, and A.I. Pashnev, Theor. Math. Phys. **74**, 264-268 (1988). https://doi.org/10.1007/BF01016619

[49] V.P. Berezovoj, and A.I. Pashnev, Z. Phys. C, **51**, 525 (1991). https://doi.org/10.1007/BF01548580

[50] V.P. Berezovoj, and M.I. Konchatnij, J. Phys. A, **45**, 225302 (2012). https://doi.org/10.1088/1751-8113/45/22/225302

[51] V.P. Berezovoj, M.I. Konchatnij, and A.J. Nurmagambetov, J. Phys. A, **46**, 065302 (2013). https://doi.org/10.1088/1751-8113/46/6/065302

[52] V.P. Berezovoj, M.I. Konchatnij, and A.J. Nurmagambetov, Nucl. Phys. B, **969**, 115483 (2021). https://doi.org/10.1016/j.nuclphysb.2021.115483

[53] F. Grossmann, T. Dittrich, P. Jung, and P. Hanggi, Phys. Rev. Lett. **67**, 516 (1991). https://doi.org/10.1103/PhysRevLett.67.516

[54] V.G. Bagrov, A.V. Shapovalov, and I.V. Shirokov, Phys. Lett. A, **147**, 348 (1990). https://doi.org/10.1016/0375-9601(90)90551-X

[55] V.G. Bagrov, A.V. Shapovalov, and I.V. Shirokov, Theor. Math. Phys. **87**, 635 (1991). https://doi.org/10.1007/bf01017951

[56] V.G. Bagrov, B.F. Samsonov, and L.A Shekoyan, Russian Phys. Jour. **38**, 706 (1995). https://doi.org/10.1007/BF00560273

[57] V.G. Bagrov, and B.F. Samsonov, J. Phys. A, **29**, 1011 (1996). https://doi.org/10.1088/0305-4470/29/5/015

[58] V.G. Bagrov, B.F. Samsonov, Phys. Lett. A, **210**, 60 (1996). https://doi.org/10.1016/0375-9601(95)00832-2

[59] V.P. Berezovoj, and A.J. Nurmagambetov, PTEP, **2024**, 063A02 (2024). https://doi.org/10.1093/ptep/ptae074

[60] P. Pereshogin, and P. Pronin, Phys. Lett. A, **156**, 12 (1991). https://doi.org/10.1016/0375-9601(91)90117-Q

[61] D. Baye, G. Lévai, and J.M. Sparenberg, Nucl. Phys. A, **599**, 435 (1996). https://doi.org/10.1016/0375-9474(95)00487-4

[62] C.M. Bender, and S. Boettcher, Phys. Rev. Lett. **80**, 5243 (1998). https://doi.org/10.1103/PhysRevLett.80.5243

[63] C.M. Bender, S. Boettcher, and P. Meisinger, J. Math. Phys. **40**, 2201 (1999). https://doi.org/10.1063/1.532860

[64] N. Moiseyev, *Non-Hermitian Quantum Mechanics*, (Cambridge University Press, 2011).

[65] A.A. Andrianov, M.V. Ioffe, and V.P. Spiridonov, Phys. Lett. A, **174**, 273 (1993). https://doi.org/10.1016/0375-9601(93)90137-O

[66] A.A. Andrianov, F. Cannata, J.P. Dedonder, and M.V. Ioffe, Int. J. Mod. Phys. A, **10**, 2683 (1995). https://doi.org/10.1142/S0217751X95001261

[67] A.A. Andrianov, M.V. Ioffe, and D.N. Nishnianidze, Phys. Lett. A, **201**, 103 (1995). https://doi.org/10.1016/0375-9601(95)00248-2

[68] A.A. Andrianov, and M.V. Ioffe, J. Phys. A, **45**, 503001 (2012). https://doi.org/10.1088/1751-8113/45/50/503001

[69] V.A. Franke, Theor. Math. Phys. **27**, 172 (1976). https://doi.org/10.1007/BF01051230

[70] V. Gorini, A. Kossakowski, and E.C.G. Sudarshan, J. Math. Phys. **17**, 821 (1976). https://doi.org/10.1063/1.522979

[71] G. Lindblad, Commun. Math. Phys. **48**, 119 (1976). https://doi.org/10.1007/BF01608499

[72] G. Lindblad, Rept. Math. Phys. **10**, 393 (1976). https://doi.org/10.1016/0034-4877(76)90029-X

[73] A. A. Andrianov, M. V. Ioffe and O. O. Novikov, J. Phys. A **52**, 425301 (2019) https://doi.org/10.1088/1751-8121/ab4338

[74] J. Jolie, AIP Conf. Proc. **2150**, 020012 (2019). https://doi.org/10.1063/1.5124584

[75] P.M. Crichigno, Preprint arXiv:2011.01239 [quant-ph], https://doi.org/10.48550/arXiv.2011.01239

ПРИКЛАДНА СУПЕРСИМЕТРІЯ

В.П. Березовий[a], **О.Ю. Нурмагамбетов**[a,b,c]

[a] *Інститут теоретичної фізики імені О.І. Ахієзера ННЦ ХФТІ, вул. Академічна, 1, Харків, 61108, Україна*
[b] *Харківський національний університет ім. В.Н. Каразіна, майдан Свободи, 4, Харків, 61022, Україна*
[c] *Інститут радіофізики та електроніки імені О.Я. Усикова, вул. Ак. Проскури, 12, Харків, 61085, Україна*

Суперсиметрія є одним із найважливіших і невід'ємних інгредієнтів сучасної теоретичної фізики. Однак відсутність, принаймні на момент написання цього огляду, експериментального підтвердження суперсиметрії у фізиці елементарних частинок і високих енергій ставить під сумнів життєздатність цього концепту на рівні енергій, досяжних на LHC. Тим більш несподіваним є або вже експериментально верифіковані, або запропоновані до верифікації прояви суперсиметрії в галузі низьких (фізика конденсованих середовищ, квантова оптика) і середніх (ядерна фізика) енергій, де працює стандартна квантова механіка. На прикладі різних систем з абсолютно різних галузей фізики ми обговорюємо ізоспектральність квантових гамільтоніанів, приховану і явну суперсиметрію, переваги підходу суперсиметричної квантової механіки та її роль у квантовому інжинірингу.
Ключові слова: *суперсиметрична квантова механіка; ізоспектральність; точно-розв'язувані моделі*

East European Journal of Physics. 2. 17-26 (2025)
DOI:10.26565/2312-4334-2025-2-02 ISSN 2312-4334

A PERSPECTIVE ON SMALL MODULAR REACTORS: A CASE STUDY FOR GREECE

Alexander Chroneos[a,b], Aspassia Daskalopulu[a], Ioannis Goulatis[a], Ruslan V. Vovk[c], Lefteri H. Tsoukalas[d]

[a]*Department of Electrical and Computer Engineering, University of Thessaly, 38333 Volos, Greece*
[b]*Department of Materials, Imperial College London, London SW7 2BP, United Kingdom*
[c]*V.N. Karazin Kharkiv National University, Kharkiv, Svobody sq., 61022, Ukraine*
[d]*School of Nuclear Engineering, Purdue University, West Lafayette, In, USA*
Corresponding Author e-mail: rvvovk2017@gmail.com
Received February 2, 2025; revised March 31, 2025; accepted April 3, 2025

Global efforts towards decarbonization are intensifying, but the transition to a green economy comes at a high cost, which some estimate to amount to approximately $3.5 trillion dollars annual investment, most of which is upfront. This puts a strain on developing economies that possess fossil natural resources, because in giving them up they become increasingly dependent on imported energy, which comes at a high cost, in addition to costs incurred by their efforts to shift to renewable energy sources. Nuclear technology produces dispatchable and uninterrupted hydrogen, heat and electricity that can cover the requirements for base load, and interest in its adoption is rising. Small modular reactors (SMR) offer a number of advantages, particularly for countries with limited nuclear expertise. Here we briefly assess the present state of SMR systems and consider their advantages and disadvantages with focus on their potential adoption in Greece. The review discusses the history, present state and the possible future of including SMRs in the emerging Greek energy mix.
Keywords: *Small Modular Reactor; Nuclear Energy; Thorium*
PACS: 28.41.Bm, 28.50.Dr, 29.25.Dz,

1. INTRODUCTION

Following the devastating consequences of its first use in Hiroshima and Nagasaki, and its associated potential for military uses, the first Atomic Era, in which nuclear power was to be deployed for civil purposes, such as the generation of cheap and ample energy, was marked by the 1946 Atomic Energy Act and reinforced in the context of the Atoms for Peace program in 1954. Since 1951, when the Experimental Breeder Reactor 1 (EBR-1) was used to generate electricity, and until August 2023, the International Atomic Energy Agency (IAEA) reports 410 nuclear power reactors in operation in 31 countries and 57 under construction [1]. We are now witnessing the beginnings of a second atomic era, hallmarked by small modular reactors (SMRs), where nuclear power is more closely associated with critical and emerging technologies and the fourth industrial revolution, and, moreover, the energy demanding fifth industrial revolution [2].

According to the World Nuclear Association [3] about 30 countries, ranging from developing nations to sophisticated economies, are considering, planning, or starting nuclear power programs. It is expected that industrialization and urbanization will grow substantially, especially in developing countries, forcing them to compete in order to gain access to cheap, abundant and 'green' energy afforded by nuclear technology, while having limited or no nuclear expertise of their own. The capacity of the grid, the population of the skilled workforce to operate such technology, and the standard of infrastructure to support the nuclear supply chain are all contributing factors that will determine which of the developing countries that are interested in nuclear power are more likely to receive design licensing and expertise from nuclear developed nations, in order to realize their aspirations. Given the nonproliferation and safety concerns that nuclear technology raises, an additional factor is the political and social stability of a country and its adherence with international rules and policy.

Greece is classified as a High-Income Country (HIC), the second largest in the Balkans and 53rd in the world, based on gross national income, according to World Bank 2022 data. It has Uranium and Thorium deposits, and construction and manufacturing industries that, with appropriate adjustment, could evolve into nuclear reactor component manufacturing. Also, it has a well-established education system that produces professionals in various fields relevant to nuclear energy, including engineering (across the full spectrum of electrical, mechanical, civil, chemical, but as yet not nuclear engineering per se), computer science, materials, environmental science and so on. The Greek grid has been undergoing substantial expansion in order to accommodate increasing numbers of renewable energy sources, and using this experience, it is well positioned to undergo further expansion, in order to be able to accommodate nuclear energy sources. Moreover, though in a dire state at the time, Greece strived to participate in the first atomic era, and at some point, developed expertise and possessed human capital that could be used to drive its participation to the second atomic era marked by SMRs.

We argue that the adoption of nuclear energy through SMRs in Greece could transform its industrial (and hence economic) development, open opportunities for its participation in the global nuclear supply chain, and enable its contribution to the global decarbonization effort. As Greece is representative of a class of similar countries (in terms of

Cite as: A. Chroneos, A. Daskalopulu, I. Goulatis, R.V. Vovk, L.H. Tsoukalas, East Eur. J. Phys. 2, 17 (2025), https://doi.org/10.26565/2312-4334-2025-2-02

economic growth, grid condition, and supply chain capabilities) we hope that this case study will contribute to stimulate further consideration of the adoption of nuclear energy by them, too, and perhaps inspire fruitful collaborations towards this goal.

The rest of the paper is organized as follows: Section 2 expands on Small Modular Reactors and their position in the evolution of nuclear technology. Section 3 focuses on the advantages and disadvantages of SMRs. Section 4 presents the historical context within which Greece developed scientific infrastructure and human capital for nuclear technology. Section 5 addresses the main concerns that have been raised for nuclear energy in Greece and outlines some of the positive prospects. Finally in Section 6 we present our conclusions in summary.

2. TECHNICAL ASPECTS AND THE EVOLUTION OF SMALL MODULAR REACTORS

The understanding of the physical properties of materials is essential to improve energy related materials for superconductor, fusion, fission, battery and fuel cell applications [4-18]. In most systems atomistic modelling techniques can offer complementary perspectives to experimental work, thus accelerating progress [19-23]. In the present environment where there is the requirement for a sustainable transition to net-zero CO_2 emissions by 2050 there is renewed support to new technologies including nuclear fusion and fission. Nuclear fusion considered as the future energy source is theoretically an infinite source of power with practically no CO_2 emissions, it is considered safe to operate, and a resilient energy system. There are still significant technical issues that need to be tamed for nuclear fusion technology to be in the energy mix by 2050. At the heart of the technology is magnetic confinement, which employs magnetic and electric fields to heat and confine the hydrogen plasma. High temperature superconductor materials including cuprate superconductors are essential in fusion technology as they are able to accommodate very high current densities in high magnetic fields. This improved power density in turn is a prerequisite to optimize the limited space in a tokamak [12].

DEMO is the fusion reactor that is anticipated to produce energy at a reasonable rate and the optimistic forecasts is that there will be required at least 25-30 years to reach this goal. The present state is a transition to renewables like solar and wind with fossil fuels being gradually excluded from the energy mix. This leaves a difficult task for the stabilization of the power grid and the required production of the base load. With batteries having a number of disadvantages (cost, environmental impact for the extraction of lithium etc.) and limited water resources and infrastructure (dams) to pump water in a higher potential energy state the only viable and low CO_2 emissions solution to produce the base load is nuclear power.

Uranium dioxide is the most common nuclear fuel. Xenon and helium in uranium dioxide have been studied for decades as they can have an impact on the thermal conductivity and physical properties of the fuel and spent fuel. In uranium-based nuclear fuels radioactive decay (i.e. alpha-decay) will lead to the production of helium. In prolonged time periods helium is accumulated and the consequence of its presence in nuclear fuel has to be assessed. In particular, at the end of use and in the disposal (or storage) stage of uranium dioxide-based fuels they will probably contain helium that was formed during the radioactive decay of actinides produced in the irradiation process.

The size of nuclear power plants and the associated costs for their construction, maintenance and operation, led to the development of SMRs, which are smaller in size, easier to site and license and can be constructed in a modular fashion in one location and then shipped for installation and operation in another location. Although they can operate at various power scales ranging from 50 MWe to several hundred MWe, typical SMR capacity is at 300 MWe per reactor, and their modularity allows for streamlined design and adaptability, as components can be added incrementally to meet changing energy demands. So far three SMRs are operational in Russia, China and India, three more are under construction, 65 are in the design stage and 39 are in the conceptual design stage [24]. As SMRs are considered promising for effective, widespread, and safer use of nuclear power for energy generation, with associated benefits for decarbonization and economic development in poorer parts of the world, the IAEA has launched a special purpose portal to promote technical cooperation, standardization and coordination of research projects [25]. Many regard SMRs as the hallmark of a new atomic era, for example as part of the plan to reactivate France's nuclear program, as announced by President Macron in February 2022, who plans €1 billion of investment to be allocated to the development of innovative small-scale reactors.

Nuclear reactors, irrespective of size, are generally categorized in generations, depending on their design as seen in Figure 1 [26].

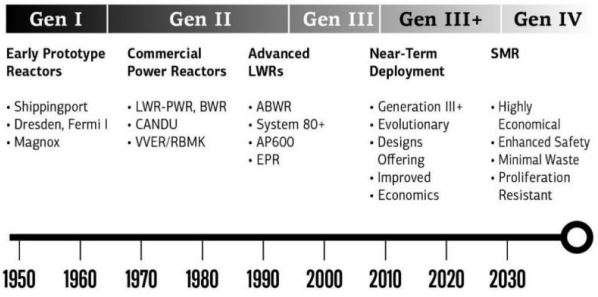

Figure 1. Evolution of nuclear reactors from the early prototype reactors to SMR [26]

The majority of current nuclear reactors in operation are generation II (or Gen II) reactors. This is a design characterization and refers to commercial reactors built until the end of the 1990s, which include pressurized water

reactors (PWR), boiling water reactors (BWR), advanced gas-cooled reactors (AGR), water-water energetic reactors (VVER), and so on. The Chornobyl and Fukushima reactors belong to this design classification, although Chornobyl was an idiosyncratic dual-purpose reactor, called RBMK, which was intended for both military and civilian purposes, and does not fully merit Gen II characterization.

Gen II reactors were succeeded by Generation III (or Gen III) reactors cooled and moderated by water, also called light water reactors (LWR), followed standardized designs that afford improvements, such as better fuel technology, higher thermal efficiency, and passive nuclear safety. The improvements are said to render Gen III reactors "evolutionary designs" with a longer operational life of 60 years, possibly extendible to 100 years, as opposed to Gen II reactors that were intended for 40 years of operation, possibly extendible to 60 years. The first Gen III reactors have been operating in Japan since 1996. Gen III reactors have solved the safety problem, especially addressing lessons learned from the Chornobyl and Fukushima accidents and consolidating the "defense in depth" safety architecture of reactor protection systems.

The Gen IV International Forum for the development of Gen IV reactors, which are hailed as "revolutionary designs", was established in 2000, but there is still no concrete deployment of such a reactor. Six designs have been selected, namely the gas-cooled fast reactor (GFR), the lead-cooled fast reactor (LFR), the molten salt reactor (MSR), the sodium-cooled fast reactor (SFR), the supercritical-water-cooled reactor (SCWR) and the very high-temperature reactor (VHTR) [27], of which the SFR is the most developed. Gen IV reactors are intended to solve the problem of economics, that is, in addition to the safety achievements of Gen III, they focus on reducing the levelized costs of Gen IV reactors to render them competitive with other power generation approaches, especially natural gas units. Additionally, some Gen IV designs aim at high temperatures to facilitate the efficient production of hydrogen.

The requirement to reduce greenhouse gas emissions (Net Zero by 2050) has led to the use of renewable energy sources (mainly solar and wind power) in synergy with nuclear units. Here nuclear can be deployed for baseload and grid security purposes because it is fully dispatchable and in addition, nuclear reactors provide emissions-free power for several years, generating not only electricity, but also, water, heat and hydrogen while ensuring grid stability and resilience, thus contributing positively to both decarbonization and energy security goals.

In the past few years there is growing research and industrial interest in SMRs. This is driven by the innovative nature of these reactors, their potential to be used in countries without civil nuclear power and their expected significant role in the decarbonization of energy production providing countries an efficient route towards net zero. Because of their smaller cost, in comparison to large nuclear power plants, and their versatility for integration they can become an essential component in the energy mix providing grid stability, security, grid resilience and energy diversification.

3. ADVANTAGES AND DISADVANTAGES OF SMR

The emergence of renewed investment in nuclear power as an essential pathway to a "carbon free future", led to a growing interest in small and medium size modular reactors [28]. This interest in compact power units, as an alternative to conventional plants, simpler in design, easier to site and license, and faster to build as well as to connect to the operating electricity grid, aims at achieving for nth-of-a-type reactors levelized costs competitive with gas. The term 'levelized costs' refers to the average cost of the energy produced over the lifetime of a generating unit. Nuclear units are very capital intensive, requiring that nearly 80% of the total cost incurred (from inception to decommissioning) to be spent upfront, that is before any power is generated. SMRs are expected to have significantly smaller licensing, siting and construction costs (all incurred before energy is produced) and therefore lower investment risks. Importantly, SMRs development involves innovative smart systems where, with the help of digitization and artificial intelligence (AI), the financial burdens for operations and maintenance as well as security of nuclear materials are reduced [29].

In mid-level countries with respect to industrial and demographical considerations (such as Greece) that are committed to the energy (or green) transition, decisions about the future energy mix (i.e., coal, oil, natural gas / liquefied natural gas (LNG), renewables, hydro, nuclear, etc.) require multicriteria analysis. SMRs can be considered as an efficient, cheaper and feasible alternative source of electricity (and fuel) generation technology (note: historically Greece has strived to participate in the atomic age initiated by the Atoms for Peace Initiative in 1950s, refer to Section 4 below).

With simplified licensing, siting, construction, and digitization, SMRs are expected to have significantly lower total investment costs compared to the conventional large nuclear stations and require reduced investment in the transmission grid if built to replace retiring fossil fuel units. In the US, through the Inflation Reduction Act (IRA) of 2023 there are strong incentives to convert retiring carbon producing coal plants with emissions-free SMRs to take advantage of existing transmission lines.

SMRs are particularly attractive for new generation nuclear power technology for countries with land and natural risks, which limit the potential for renewable energy (for example Japan). SMRs can have similar operating conditions and fuel arrangements with most types of large nuclear power plants but reduced refueling needs (some types can operate for up to 30 years without replenishment of uranium). The small, modular, and factory-based construction and standardization of components and systems, means reduced construction costs together with faster licensing and shorter installation times.

A further advantage of SMRs is the flexible cooling requirements and the flexibility to serve as a backup power supply [30] as they can also be employed for applications such as water desalination, which can be particularly important in islands or remote areas as well as highly interconnected smart grids operating through price-directed demand-side management and in need of reliable local power sources ensuring proper and fast islanding to prevent cascading failures [31].

Thorium dioxide and mixed fuels containing thorium can be adopted in SMRs. This is important as there is increasing interest in alternative thorium-based nuclear fuels so as to benefit from the relatively abundant thorium resources and the potential of a safer proliferation resistant fuel [32-35]. There is a regeneration of interest in thorium-based fuels and this is also reflected in the research of their physical properties [36-39]. Thorium-based fuels have advantages but require knowhow of the Th fuel cycle and hence an already developed nuclear industry. So this can be a drawback for nuclear-emerging countries such as Greece.

The difficulty to store electricity efficiently has led to the consideration of alternative routes such as hydrogen production. Hydrogen can be used in solid oxide fuel cells (SOFC) to produce electricity and power vehicles or industrial facilities. The problem with hydrogen production is that it requires energy and high temperatures. An SMR can be used in synergy with a hydrogen production facility (effectively a solid oxide electrolysis cell (SOEC)) to take advantage of the heat and the excess off-peak electricity produced by the reactor. The process in the SOEC is effectively the reverse of the SOFC and leads to the production of hydrogen. As the latter is also hard to store efficiently, chemical engineering routes can be used to convert hydrogen to syn-gas or even liquid fuel that can then be used straight on in mobile and industrial applications using existing infrastructure. Notably, the use of hydrogen apart from the difficulty to store poses safety risks as it has a wide detonation range, it is difficult to detect, and can even cause embrittlement to steel containers.

There are still some technical issues (for example, on the ceramic electrolyte membranes) that need to be overcome, but the production of syn-gas or liquid fuels taking advantage of nuclear resources is appealing, particularly if it is combined with carbon capture. That is, if the carbon required in the process is captured then there will be very little net CO_2 being produced, while the existing infrastructure will be maintained.

Workforce preparation is needed through credential-granting academic programs based on best international practices properly implemented and accredited. A properly credentialed workforce is *sine qua non* for nuclear industry and regulators, as this is an area firmly within national frames of responsibilities, and multilateral agreements for frameworks of international collaboration, fully respecting nonproliferation and safety objectives. In addition, the implementation of new licensing and siting criteria will require new expertise in nuclear safety regulatory bodies.

Last, but not least, we are aware that a "fleet" of smaller and distributed nuclear reactors is likely to present substantial problems with public acceptance. This increased risk can be important in countries with seismic areas and vulnerable to tsunamis. In addition to improvements in science education (STEM), to address the issue of public acceptance, there has to be great openness and a public dialogue that fully respects the public's right to know and choose through democratic processes.

4. NUCLEAR IN GREECE

Having briefly presented the advantages and challenges posed by SMR technology, we now turn to consider how realistic it is for Greece to adopt SMRs, and argue that, given its historical participation in the first atomic era, it is well-positioned to participate actively in the current, new atomic era.

4.1. GRR-1: The First Research Reactor

The atomic era in Greece, as in many other developed and developing countries globally, began after Eisenhower's "Atoms for Peace Initiative", announced at the United Nations in December 1953 [40, 41]. According to this Initiative, first-generation nuclear facilities would be created as a result of cooperation between the United States Atomic Energy Commission (USAEC) and other national authorities on atomic energy research and power projects, on a common legal basis worldwide in the period 1950s – 1970s. In 1954, the US Congress provided the legal basis for "Atoms for Peace" by enacting the Atomic Energy Act of 1954 [42].

In the geopolitical and geoeconomic backdrop of the first decades following WWII Greece was a major part of the long-term development program "The Marshall Plan, authorizing the European Recovery Program" [43]; all energy matters in Greece, including atomic energy research, education, safety, and cutting-edge applications were part of the crucial international cooperation framework between the USA and Western Europe that led to an historically unprecedented period of peace and prosperity in the whole continent. However, Greece's integrated energy development programme was idiosyncratic due, primarily, to the nine years that elapsed from the start of WWII in 1940 till the end of the subsequent civil war and the establishment of the Greek Public Power Corporation (PPC/DEI) in 1950 [44].

During the 1950s and early 1960s, coal was the main natural source for electricity generation; indicatively, 64% of electricity generation in 1958 was fuel by domestically available lignite [45] and this situation in the Greek energy system persisted with similar quality characteristics during the following decades, mainly due to the political / economical targeting to minimize the dependence of the energy system on oil imports (after the late 2000s, on both: oil and natural gas) and the use of indigenous sources instead. Consequently, the share of lignite (coal) in electricity generation increased from about 30% in 1973 (first oil crisis) and 47% in 1979 (second oil crisis), to 62% in 1983, 74% in 1989, 70% in 1998 and to about than 60% - 70% in 2000s (depending on the methodology). Indicatively in 2008-09 (global economic crisis), the above indicator was 53% & 56% correspondingly.

It is in general accepted that this, had a negative impact to the efficiency of the country's energy sector and economy and specifically, during the first period we investigate in this study (until the 1980s), Greece was highly dependent on imported fuels for the overall energy mix, while generating electricity from domestically available lignites [45, 46]. Nevertheless, this was also a period of atomic and nuclear research and the quest for uranium resources for a possible

nuclear power plant in Greece [47]. In accordance with the principles and the financial and technical assistance possibilities set by the international cooperation legal framework as a result of the “Atoms for Peace" US policy (1953-54), and the aspirations, the persistent focus and vision of distinguished scientists and statesmen for the modernization of the Greek economy through energy self-sufficiency and technology development [48] crucial steps were taken regarding the participation of the Greek State in the United Nations International Atomic Energy Agency (UN-IAEA). Indicatively, Greece is one of the founding members of CERN that was established in 1954 [49]. In 1954 also, the Greek Atomic Energy Commission (GAEC/EEAE) was established and given authority over nuclear safety and regulation matters [50].

The GAEC with the assistance of the US Atomic Energy Commission (US-AEC), the predecessor of the current US Department of Energy (DOE), and the Nuclear Regulatory Commission (NRC), founded the “Demokritos Nuclear Centre” in 1959, featuring a research reactor (GRR-1) and a number of supplementary laboratories [51]. Six fundamentally important years passed between the Research Agreement of GAEC with US-AEC in 1955 [52], followed by the contract signed with the American firm “AMF Atomics” for the design and construction of the first 1 MW pool Greek Research Reactor and its inauguration in 1961. GRR-1 achieved criticality for the first time on July 31st, 1961, its operation at full power began in April 1964 and in July 1971 the reactor was operated at increased power of 5 MW.

The establishment of an atomic research center in Greece contributed to the growth of scientific research in the region [53] and for decades thereafter the GRR-1 has been the main nuclear facility in Greece. It remained functional until the eve of the Athens Olympic Games in 2004. In July 2004, it was put in a state of extended shut-down. All used High Enrichment Uranium (HEU) fuel elements were returned to the USA in 2005, following the terms of fuel purchase agreement between the U.S. Department of Energy and the Greek Government. During the period 2005-2010, the reactor was shut-down for maintenance and preparation of the core conversion to Low Enrichment Uranium (LEU) [54]. Since February 2019, all LEU fuel elements have been repatriated to North America. The current license granted to GRR-1 for extended shutdown is due for renewal in October 2024 [55].

4.2. Greece’s Potential Nuclear Energy Programme

Importantly, Greece is a party to the 1968 Treaty on the Non-Proliferation of nuclear weapons (NPT), which it ratified on 11 March 1970 [56] and the Additional Protocol which supplements the NPT. Civil nuclear energy was considered back in the 1960’s and 1970s as one of the country's long term development program priorities [45, 48]. Several factors, such as public lectures by distinguished researchers and university professors [48], the subsequent PPC’s plans and discussions to build nuclear power plants as an alternative source for electricity generation in 1963 [45], the progress in nuclear technology, the political stability after the “Junta” period and the restoration of democracy [45, 48], and the investment interest raised by the system for licensing on nuclear installations (legal framework regarding: *conditions and procedures for licensing on nuclear installation of the Public Electricity Corporation)* in 1978 [57], mobilized the scientific pool and policy makers in Greece and worldwide in investigating opportunities for designing and building a nuclear power plant (NPP) in Greece. Despite the first and second oil crises in 1973 and 1979 respectively with a strong energy impact in Greek economy [46, 58] and in spite of the government investment programme in oil & natural gas fields & PPC's lignite mines after the 1979 oil crisis, some reports and pre-feasibility and site evaluation studies were commissioned by the PPC, among them, the Ebasco’s study, in order to identify potential appropriate locations for the installation of a Nuclear Plant (Table 1, Figure 2, Ref. 45 and references therein).

Table 1. Timeline of the atomic research and energy era in modern Greece.

YEAR	Milestones
1950	Establishment of the Greek Public Power Corporation (PPC/DEI), (07.08.1950)
1954	Establishment of Greek Atomic Energy Commission GAEC / EEAE (26.02.1954) CERN (Convention entered in force, 29.09.1954. Greece is one of the founder members)
1955	04.08.1955 Research Agreement between USAEC and Greece to construct a research Reactor
1961	The GRR-1 achieved criticality for the first time 31.07.1961. "Opening" of the Democritus Nuclear Centre / The inauguration of the reactor
1978	New Legislations about the establishment and operation of nuclear facilities. Conditions and procedures for licensing on nuclear installation of the Public Electricity Corporation (PPC)
1985	Administrative and operational separation of GAEC from the National Center of Scientific Research "Demokritos"
1986	Chornobyl NPP accident (26.04.86)
2004	Since July 2004, the Research Reactor is in state of extended shut-down
2011	Fukushima NPP accident (11.03.2011) New European Nuclear Safety Regulators Group [39] criteria, methodology and the timeframe for carrying out the" stress tests"
2019	GRR-1. All used LEU fuel elements have been repatriated to USA since February 2019

Figure 2. Nuclear power plants' possible locations proposed in early 1980's ([45] and references therein) in relation to the main regions with operating thermal power plants (TPP) and the Prinos oil field (P). (1) near the city of Larissa, (2) Near the village Mandudi, (3) Near the town Karystos, (4) Ilia Prefecture, (5) southwest of the city of Tripolis, (6) west of cape Maleas, (7) Near the village Archagelos. GRR-1, is the Greek Research Reactor, situated in "Demokritos' ' Nuclear Centre, Athens, WMLC - West Macedonia Lignite Centre, MLC – Megalopolis Lignite Centre.

4.3. The Consequences of Nuclear Accidents

The 26 April 1986 accident at the Chornobyl nuclear power plant in Ukraine (then USSR) had a decisive influence on the development of international nuclear law over the following two decades. In Greece, preliminary NPP construction plans froze. The then prime minister Andreas Papandreou moved on to cancel them. The abandonment of these plans boosted exploitation of Greek lignite ores (from 54% as source for electricity generation in 1980-85, lignite ores rose to 69% in 1986-91 ([45] and references therein). After the Fukushima NPP accident (11.03.2011), new criteria, methodology and the timeframe for carrying out the "stress tests" were introduced by the European Nuclear Safety Regulators Group [59].

4.4. Uranium Deposits in Greece

The research / investigations (geological surveys) for Uranium ore deposits in Greece, began in the early 1950s by American, English and French scientific teams and experts that collaborated with Greek researchers [45, 47, 48].

In the late 1970s, the Institute of Geological and Mining Research (IGME) carried out new surveys regarding categories of uranium minerals and possible mining locations in Greece. The main Uranium raw material (ore) deposits were being identified in North Greece's regions ([45, 47, 48] and references therein). The geographical sites and the quantities (of uranium mineral resources in N. Greece) are documented in [47], in "Red Books" [60], i.e., national reports, published between 1973 and 2005, and in scientific investigations [61] and references therein). The estimated Greece Uranium resources in earlier studies ([45, 47, 48, 60, 61) and in most recent estimations [62, 63] are summarized and presented in Table 2.

Table 2. Estimated Uranium Resources in Greece in Tonnes U.

Identified Recoverable Resources / (Uranium, 2009, Uranium, 2022)	**7000**
Reasonably Assured Resources (RAR)	*6000*
Inferred Resources (IR)	*1000*
Undiscovered resources (prognosticated, cost range < USD 260/KgU) [62, 63]	*6000*
Unconventional resources (phosphate rocks, reported in Red Books 1965-1993) [62]	*500*
Indicated reserves of uranium (U3O8) [61]	*1800*
Identified in situ resources (RAR + IR, cost range < USD 260/KgU) [63]	*9300*

As shown in Table 2 the current estimations in both identified recoverable resources and undiscovered resources in cost range < 260/KgU in Greece are more than 13 thousand tonnes U.

5. CONCERNS AND PROSPECTS

A main argument against the development of civil nuclear facilities in Greece has been seismic activity. It should be stressed, however, that about 20% of nuclear power stations in the world are in seismically active areas and these include facilities in the USA and Japan. Interestingly, neighboring countries with seismic activity such as Bulgaria [64] and Turkey (Akkuju NPP) operate nuclear power stations. Greece has had strict building codes for many years and was

one of the first countries worldwide to enforce laws and codes for earthquake resistant buildings. The current building code, established in 2000 and informed by international and local experience, is considered one of the strictest globally and the reported damage in public buildings by earthquakes is very low. At any rate it is anticipated that there are areas in Greece with limited seismicity, where nuclear power station(s) with appropriate earthquake engineering can be built. From another viewpoint the rigorous and principled design of a nuclear structure will require substantial effort that could also have a positive impact on the future design code, thus enhancing the safety of buildings and other structures.

Another argument against the development of civil nuclear facilities in Greece has been the prospect of exploiting renewable energy sources, such as wind and solar power, which are considered safer than nuclear power, and relatively abundant in the Greek region. However, there are several points that counter this argument. One of them concerns power density [65] i.e., the average electrical power produced in one horizontal square meter of infrastructure: renewables take up a lot of space, as wind turbines must be spaced out in large areas, and likewise solar panels are meaningless if they are used only in small spaces. The power density for nuclear power is about 1000 W/m^2 compared with 2-3 W/m^2 for wind and 100 W/m^2 for solar. Another point concerns dispatchable generation capacity and reliability: nuclear reactors can generate power at a constant rate as opposed to wind farms and solar panels that rely on such volatile sources. This impacts on the stability and, consequently, safety of the power grid. Various studies have examined the potential for competitive large-scale renewable deployment and concluded that it is more difficult to accomplish than as many anticipate [66, 67]. However, the experience that has been acquired through efforts to increase the integration of renewables is valuable, should one view them as proxies for SMR integration in the grid.

The adoption of SMR in Greece will have numerous positive consequences. In conjunction with the production of electricity, SMRs may be used synergistically with electrolyzes to produce low-carbon hydrogen and hydrogen containing fuel such as methanol or ammonia. In particular, the heat and power from the SMR can be employed for the production of low-carbon hydrogen. Given SMRs flexible modular design they can be located near energy intensive industrial processes including, but not limited to, cement factories, steel mills, oil refineries, shipbuilding facilities, cable, aluminum and critical materials refineries, where emissions-free sources of hydrogen may be used to achieve carbon reduction targets in industry as well as abet the production of peak electricity with fuel cells. Presently, only very limited amounts of green hydrogen are produced and these cannot deliver the large quantities of clean hydrogen required to make a difference in transport and industrial applications. Nuclear hydrogen production taking advantage of the SMR technologies is a key component to produce low-cost hydrogen, which is critical to decarbonize and propel the economic machinery of a country. For transport applications hydrogen has advantages but it is also problematic to store (metal embrittlement, low temperatures) and handle (has a high detonation range, odorless). These problems can be overcome, however, if the net aim is not to produce hydrogen as an end product, but rather use the hydrogen produced as an intermediate step for the production of methanol, syngas and liquid fuels. This will be very beneficial environmentally, if the carbon required for these processes is via carbon capture, but also because there will be no need to change all the gas stations to hydrogen ones that will require substantial infrastructure and extensive training of the staff.

As an illustrative example, four 300 MWe SMRS can produce 10 GWh of electric energy annually, which is approximately 20% of electricity consumption in Greece. By mid-century this number can quadruple, resulting in the production of 40 GWh capable of fueling electric vehicles and, thus, replacing the current 25% of the total energy mix which is used by internal combustion engines for transportation. Additional electricity from wind, solar, biomass and hydro can result in an energy mix fully compliant with net zero targets. This can be considered a *low growth scenario*, where the economy is in steady state, that is with less than 1% average annual growth.

A more aggressive *high growth scenario* has the economy growing annually by an average of at least 3%. In this scenario, significant investment will be needed in nuclear power and the transmission/distribution system of electric power. Tripling the overall electric energy output by mid-century, that is going from approximately 50 GWh per year to 150 GWh per year, can be abetted by having at least 50% of the electric power provided by nuclear sources. In such a scenario the levelized cost of electricity is expected to be reduced to nearly 1/3 of current values extending benefits far beyond energy generation.

Another important possibility afforded by SMRs concerns the production of marine fuel. This is key for the Greek economy as one of the main pillars (arguably the strongest) of the shipping industry, which under new regulations will need to become greener. Renewable energy solutions do not have the energy density to power the fleet, whereas changing to alternative “greener” fuels will require changing the engines etc. A viable pathway may be hybrid engines burning ammonia fabricated with nuclear-produced emissions-free hydrogen.

The construction of SMRs will create numerous job opportunities, contributing to overall employment and high growth. Over 1,100,000 job-years of highly paid jobs will be added in the Greek economy under the low growth scenario. On the other hand, under the high growth scenario, which is the more likely of the two, the adoption of SMRs to fuel up to 5 GWe capacity may create in excess of 5,000,000 job-years. Nuclear power creates a substantial economic ecosystem with numerous engineering, manufacturing, logistics and service jobs [68]. As an indication of such growth prospects, consider that as early as in the 1970s Dr Karakalos conducted important radiographic work at NSCR Demokritos, which led to the uncovering of the Antikythera Mechanism gear system [69, 70, 71], opening new opportunities for archaeometry and material science. The reactor was used to perform neutron radiography, a technique that involves the use of neutrons to produce images of the internal structure of objects, through the layers of corrosion and other materials, without

damaging the artifact. Neutron detector technology for materials' defect inspection (e.g. weld analysis, concrete inspection, radiation hardening) was estimated to be US$1.2 billion in 2023 and projected to US$3.8 billion in 2033.

6. CONCLUSIONS

In the present review the state of SMRs and their potential use in countries such as Greece was assessed. More than six decades after the construction of the experimental nuclear facility in Demokritos there has been no civil nuclear power station. Greece has relied heavily on domestic lignites and oil and gas imports; however, this is no longer sustainable or economically viable under decarbonization with voluntary or binding targets in almost all economic activities including, but not limited to, power generation, transportation, shipping, industry, agriculture and services.

In the present crossroads, SMRs for Greece make technical and economic sense. To keep the nuclear option open Greece will have to rapidly invest in the development of the workforce and supply chain infrastructure. It is estimated that nearly one million new nuclear technical and engineering positions will be needed globally by mid-century. Hence there is an urgent need to invest in the academic sector for engineers and technicians with nuclear credentials, as have other countries with more steady involvement in nuclear energy (for example the UK). Investments in three (3) SMR units of 1 GWe total installed capacity are expected to create approximately 200,000 man-years of employment in high-paying engineering and technical jobs. In addition, it is anticipated that the adoption of SMRs and participation in engineering workforce and supply chain development will have a very positive impact on several high-value-added sectors including domestic refining and transport, batteries, semiconductors and critical materials mining and processing. Of particular importance will be the use of low temperature heat and off-peak electricity to produce hydrogen and liquid fuels.

Nuclear power adoption will be critical in decreasing oil/gas imports and increasing energy independence for Greece. The cost of imported energy currently represents up to 10% of the GDP, and its reduction can tip the economy from recession to growth. In recent years, in the context of increasing energy independence (while at the same time contributing to the global effort for decarbonization) Greece has been investing heavily on renewables, which are volatile and harmful for grid stability. However substantial expertise has been gained from the incorporation of renewables and the consequent grid expansion required, as one might view them as proxies for SMRs.

Last, but not least, nuclear power adoption will necessitate further development of the education system, in order to prepare highly qualified human capital, and perhaps contribute to repatriate human capital, as today most of the Greek nuclear experts work abroad.

Author Contributions: The manuscript was written and edited by all authors.
Funding: This research received no external funding.
Institutional Review Board Statement: Not applicable.
Informed Consent Statement: Not applicable.
Ethics Approval: Not applicable.
Availability of Data and Materials: No data was used for the research described in the article.
Acknowledgments: Not applicable.
Conflicts of Interest: The authors declare no conflict of interest.

ORCID

Alexander Chroneos, https://orcid.org/0000-0002-2558-495X; **Aspassia Daskalopulu,** https://orcid.org/0000-0003-1051-6302
Ruslan V. Vovk, https://orcid.org/0000-0002-9008-6252; **Lefteri H. Tsoukalas,** https://orcid.org/0000-0002-6718-1163

REFERENCES

[1] The Database of Nuclear Power Reactors, https://pris.iaea.org/pris/, last accessed 24/08/2023
[2] OSTP 2022. Critical and Emerging Technologies, A Report by the Fast Track Action Subcomittee on critical and emerging Technologies of the National Science and Technology Council, Office of the President of the USA, February 2022. https://www.whitehouse.gov/wp-content/uploads/2022/02/02-2022-Critical-and-Emerging-Technologies-List-Update.pdf
[3] WNA 2023. Emerging Nuclear Energy Countries. World Nuclear Association. https://world-nuclear.org/information-library/country-profiles/others/emerging-nuclear-energy-countries.aspx
[4] R.C. Baetzold, "Atomistic study of defects in $YBa_2Cu_3O_7$," Phys. Rev. B, **42**, 56 (1990). https://doi.org/10.1103/PhysRevB.42.56
[5] K. Lang, V. Madhavan, J.E. Hoffman, E.W. Hudson, H. Eisaki, S. Uchida, and J.C. Davis, "Imaging the granular structure of high-Tc superconductivity in underdoped $Bi_2Sr_2CaCu_2O_{8+\delta}$," Nature (London), **415**, 412-416 (2002). https://doi.org/10.1038/415412a
[6] M.A. Obolenskii, R.V. Vovk, A.V. Bondarenko, and N.N. Chebotaev, "Localization effects and pseudogap state in single crystals with different oxygen content," Low Temp. Phys. **32**, 571-575 (2006). https://doi.org/10.1063/1.2215373
[7] R.V. Vovk, M.A. Obolenskii, A.A. Zavgorodniy, A.V. Bondarenko, I.L. Goulatis, A.V. Samoilov, and A. Chroneos, "Effect of high pressure on the fluctuation conductivity and the charge transfer of $YBa_2Cu_3O_{7-\delta}$ single crystals," J. Alloys Compds. **453**, 69-74 (2008). https://doi.org/10.1016/j.jallcom.2006.11.169
[8] R.V. Vovk, Z.F. Nazyrov, M.A. Obolenskii, I.L. Goulatis, A. Chroneos, and V.M. Pinto Simoes, "Phase separation in oxygen deficient $HoBa_2Cu_3O_{7-\delta}$ single crystals: effect of high pressure and twin boundaries," Phil. Mag. **91**, 2291-2302 (2011). https://doi.org/10.1080/14786435.2011.552893
[9] R.V. Vovk, M.A. Obolenskii, Z.F. Nazyrov, I.L. Goulatis, A. Chroneos, and V.M.P. Simoes, "Electro-transport and structure of 1-2-3 HTSC single crystals with different plane defects topologies," J. Mater. Sci.: Mater. Electron. **23**, 1255-1259 (2012). https://doi.org/10.1007/s10854-011-0582-8

[10] A.L. Solovjov, E.V. Petrenko, L.V. Omelchenko, R.V. Vovk, I.L. Goulatis, and A. Chroneos, "Effect of annealing on a pseudogap state in untwinned $YBa_2Cu_3O_{7-\delta}$ single crystals," Sci. Rep. **9**, 9274 (2019). https://doi.org/10.1038/s41598-019-45286-w
[11] F. Chiabrera, I. Garbayo, L. Lopez-Conesa, G. Martin, A. Ruiz-Caridad, M. Walls, L. Ruiz-Gonzalez, *et al*., "Engineering Transport in Manganites by Tuning Local Nonstoichiometry in Grain Boundaries," Adv. Mater. **31**, 1805360 (2019). https://doi.org/10.1002/adma.201805360
[12] A. Holland, "Government Policy for the Fusion Energy Economy- Lessons from the Fusion Industry Association's First Two Years," J. Fusion Energy, **42**, 14 (2023). https://doi.org/10.1007/s10894-023-00356-w
[13] R. Devanathan, W.J. Weber, and G.D. Gale, "Radiation tolerance of ceramics—insights from atomistic simulation of damage accumulation in pyrochlores," Energy Environ. Sci. **3**, 1551-1559 (2010). https://doi.org/10.1039/C0EE00066C
[14] A. Chroneos, M.J.D. Rushton, C. Jiang, and L.H. Tsoukalas, "Nuclear wasteform materials: Atomistic simulation case studies," J. Nucl. Mater. **441**, 29-39 (2013). https://doi.org/10.1016/j.jnucmat.2013.05.012
[15] S.C. Lumley, R.W. Grimes, S.T. Murphy, P.A. Burr, A. Chroneos, P.R. Chard-Tuckey, and M.R. Wenman, "The thermodynamics of hydride precipitation: The importance of entropy, enthalpy and disorder," Acta Materialia, **79**, 351-362 (2014). https://doi.org/10.1016/j.actamat.2014.07.019
[16] M.W.D. Cooper, R.W. Grimes, M.E. Fitzpatrick, and A. Chroneos, "Modeling oxygen self-diffusion in UO2 under pressure," Solid State Ionics **282**, 26-30 (2015). https://doi.org/10.1016/j.ssi.2015.09.006
[17] E. Zapata-Solvas, S.R.G. Christopoulos, N. Ni, D.C. Parfitt, D. Horlait, M.E. Fitzpatrick, A. Chroneos, and W.E. Lee, "Experimental synthesis and density functional theory investigation of radiation tolerance of $Zr_3(Al_{1-x}Si_x)C_2$ MAX phases," J. Am. Ceram. Soc. **100**, 1377-1387 (2017). https://doi.org/10.1111/jace.14742
[18] A.L. Solovjov, L.V. Omelchenko, E.V. Petronko, R.V. Vovk, V.V. Khokevych, and A. Chroneos, "Peculiarities of pseudogap in $Y_{0.95}Pr_{0.05}Ba_2Cu_3O_{7-\delta}$ single crystals under pressure up to 1.7 GPa," Sci. Rep. **9**, 20424 (2019). https://doi.org/10.1038/s41598-019-55959-1
[19] S.T. Murphy, "A point defect model for $YBa_2Cu_3O_7$ from density functional theory," J. Phys. Commun. **4**, 115003 (2020). https://doi.org/10.1088/2399-6528/abc9a7
[20] F. Baiutti, F. Chiabrera, M. Acosta, D. Diercks, D. Parfitt, J. Santiso, X. Wang, A. Chroneos, *et al*., "A high-entropy manganite in an ordered nanocomposite for long-term application in solid oxide cells,"Nat. Commun. **12**, 2660 (2021). https://doi.org/10.1038/s41467-021-22916-4
[21] M. Dahlqvist, and J. Rosen, "The rise of MAX phase alloys – large-scale theoretical screening for the prediction of chemical order and disorder," Nanoscale, **14** 10958-10971 (2022). https://doi.org/10.1039/D2NR02414D
[22] M.M. Jin, J.L. Miao, B.H. Chen, M, Khafizov, Y.F. Zhang, and D.H. Hurley, "Extended defects-enhanced oxygen diffusion in ThO_2," Comp. Mater. Sci. **235**, 112842 (2024). https://doi.org/10.1016/j.commatsci.2024.112842
[23] L. Johnson, W. Malone, J. Risk, R.A. Chen, T. Gibson, M.W.D. Cooper, and G.T. Craven, "Machine learning method to determine concentrations of structural defects in irradiated materials," Comp. Mater. Sci. **242**, 113079 (2024). https://doi.org/10.1016/j.commatsci.2024.113079
[24] Number of global SMR projects 2022, Statista Research Department, https://www.statista.com/statistics/1334632/number-of-small-modular-reactor-projects-worldwide/, last accessed 24/08/2023.
[25] The platform of Small Modular Reactors and their Applications, https://nucleus.iaea.org/sites/smr/SitePages/HomeSmrPlatform.aspx, last accessed 24/8/2023.
[26] S.M. Goldberg, and R. Rosner, *Nuclear Reactors: Generation to Generation. American Academy of Arts and Sciences*, 2011, https://www.amacad.org/sites/default/files/academy/pdfs/nuclearReactors.pdf
[27] G. Locatelli, M. Mancini, and N. Todeschini, "Generation IV nuclear reactors: Current status and future prospects," Energy Policy, **61**, 1503-1520 (2013). https://doi.org/10.1016/j.enpol.2013.06.101
[28] B. Steigerwald, J. Weibezahn, M. Slowik, and C. von Hirschhausen, "Uncertainties in estimating production costs of future nuclear technologies: A model-based analysis of small modular reactors," Energy, **281**, 128204 (2023). https://doi.org/10.1016/j.energy.2023.128204
[29] L.H. Tsoukalas, *Fuzzy Logic: Applications in Artificial Intelligence, Big Data, and Machine Learning*, (McGraw Hill, New York, 2024).
[30] S. Froese, N.C. Kunz, and M.V. Ramana, "Too small to be viable? The potential market for small modular reactors in mining and remote communities in Canada," Energy Policy, **144**, 111587 (2020). https://doi.org/10.1016/j.enpol.2020.111587
[31] L.H. Tsoukalas, and R. Gao, "Inventing Energy Internet: The role of Anticipation in Human-centered Energy Distribution and Utilization," in: *2008 SICE Annual Conference*, (Chofu, Japan, 2008), pp. 399-403, https://doi.org/10.1109/SICE.2008.4654687
[32] M. Kazimi, "Thorium fuel for nuclear energy: an unconventional tactic might one day ease concerns that spent fuel could be used to make a bomb," Am. Sci. **91**, 408–415 (2003). https://www.americanscientist.org/sites/americanscientist.org/files/200582141548_306.pdf
[33] S.F. Ashley, G.T. Parks, W.J. Nuttall, C. Boxall, and R.W. Grimes, "Thorium fuel has risks," Nature, **492**, 31–33 (2012). https://doi.org/10.1038/492031a
[34] World Thorium Occurrences, 2019. Deposits and Resources. IAEA TECDOC-1877, Vienna.
[35] A. Chroneos, I. Goulatis, A. Daskalopulu, and L.H. Tsoukalas, "Thorium fuel revisited," Progress Nucl. Energy, **164**, 104839 (2023). https://doi.org/10.1016/j.pnucene.2023.104839
[36] A. Chroneos, and R.V. Vovk, "Modeling self-diffusion in UO_2 and ThO_2 by connecting point defect parameters with bulk properties," Solid State Ionics, **274**, 1–3 (2015). https://doi.org/10.1016/j.ssi.2015.02.010
[37] N. Kuganathan, P.S. Ghosh, C.O.T. Galvin, A.K. Arya, B.K. Dutta, G.K. Dey, and R.W. Grimes, "Fission gas in thoria," J. Nucl. Mater. **485**, 47–55 (2017). https://doi.org/10.1016/j.jnucmat.2016.12.011
[38] A.V. Colton, and B.P. Bromley, "Simulations of pressure-tube-heavy-water reactor cores fueled with thorium-based mixed-oxide fuels," Nucl. Technol. **203**, 146–172 (2018). https://doi.org/10.1080/00295450.2018.1444898
[39] S. Moxon, J. Skelton, J.S. Tse, J. Flitcroft, A. Togo, D.J. Cooke, E.L. da Silva, *et al*., "Structural dynamics of Schottky and Frenkel defects in ThO_2: a density-functional theory study," J. Mater. Chem. **10**, 1861–1875 (2022). https://doi.org/10.1039/D1TA10072F
[40] J. Krige, and K.H. Barth, "Introduction," Osiris, **21**(1), 1–21 (2006). https://doi.org/10.1086/507133
[41] J.F. Pilat, editor, *Atoms for Peace: An Analysis After Thirty Years*, 1st ed. (Routledge, 1985). https://doi.org/10.4324/9780429038327

[42] The Atomic Energy Act of 1954. Pub. L. No 703, 83th Cong, 2d Sess. (1954), 68 Stat. 919
[43] The Economic Cooperation Act of 1948. Pub. L. No 472, 80th Cong.; 2d Sess. (1948), 62 Stat. 137
[44] Greece: Law 1468 of 1950, Official Gazette vol. A.169/1950. https://www.et.gr/api/DownloadFeksApi/?fek_pdf=19500100169 (in Greek)
[45] S. Arapostathis, A. Kandaraki, Y. Garyfallos, and A. Tympas, "Tobacco for Atoms': Nuclear Politics, Ambivalences and Resistances about a Reactor that was Never Built," History of Technology, **33**, 205-227 (2017).
[46] A. Angelis-Dimakis, G. Arampatzis and D. Assimacopoulos, "Monitoring the sustainability of the Greek energy system," Energy Sustain. Dev. **16**(1), 51-56 (2012). https://doi.org/10.1016/j.esd.2011.10.003
[47] E.K. Judd, and H.E. DeSanctis, "Possibilities for uranium in Greece, report," (University of North Texas Libraries, UNT Digital Library, 1953). https://digital.library.unt.edu/ark:/67531/metadc1393254/
[48] A. Hekimoglou, *Atomic era. Nuclear energy, Reactors and Uranium in Greece in the 20th c*. (Papadopoulos Publications, Athens, 2023). (in Greek).
[49] CERN (1971). Convention for the establishment of a European organization for nuclear research: Paris, 1st July, 1953: as amended. Geneva: CERN. https://legal-service.web.cern.ch/system/files/downloads/CONVENTION.pdf
[50] Greece: Law 2750 of 1954, Official Gazette vol. A.32/1954. https://www.et.gr/api/DownloadFeksApi/?fek_pdf=19540100032 (in Greek)
[51] IAEA, *Report on Greece. Establishment of an Atomic Centre*, (IAEA Bulletin, **1**(2), 9-10 (1959).
[52] L.L. Strauss, Twenty-second Semiannual Report of the Commission to the Congress, July 1957. United States, 1957. https://doi.org/10.2172/1364038
[53] P. Dimotakis, "The Demokritos Nuclear Research Centre, Greece," Nature, **220**, 861–862 (1968). https://doi.org/10.1038/220861a0
[54] GAEC (2014). Greece Report as required under Article 9.1 of Council Directive 2009/71/EURATOM. https://energy.ec.europa.eu/system/files/2021-02/el_implementation_reports_2014_en_0.pdf
[55] GAEC (2020). Report of Greece of July 2020 on the implementation of Council Directive 2009/71/Euratom as amended by the Council Directive 2014/87/Euratom. https://energy.ec.europa.eu/system/files/2021-03/12._el_2nd_2020_report_a-nsd_0.pdf
[56] NEA (2020). Nuclear Legislation in OECD and NEACountries: Greece (2016 update), OECD Publishing, Paris.
[57] Greece: Presidential Decree 610 of 1978, Official Gazette, vol. A.130/1978. https://www.et.gr/api/DownloadFeksApi/?fek_pdf=19780100130 (in Greek).
[58] G. Donatos, and G. Mergos, "Energy demand in Greece: The impact of the two energy crises," Energy Economics, **11**(2), 147-152 (1989). https://doi.org/10.1016/0140-9883(89)90008-X
[59] ENSREG, 2011. Declaration of ENSREG - EU "Stress Tests" specifications. https://www.ensreg.eu/news/declaration-ensreg-eu-stress-tests-specifications
[60] Uranium, 2005. Resources, Production and Demand, OECD NEA/IAEA, 2006
[61] A. Tsirambides, and Filippidis, "Energy Mineral Resources of Greece," Journal of Environmental Science and Engineering B, **1**, 709-719 (2012).
[62] Uranium, 2009. Resources, Production and Demand, OECD NEA/IAEA, 2010.
[63] Uranium, 2022. Resources, Production and Demand, OECD NEA/IAEA, 2023.
[64] A. Tympas, S. Arapostathis, K. Vlantoni, and I. Garyfallos, "Border Crossing Electrons: Critical Energy Flows in the Balkans from WWII to the Post-Cold War Era," in: *The Making of Europe's Critical Infrastructures: Common connections and shared vulnerabilities*, P. Högselius, A. Hommels, A. Kaijser, and E. Van der Vleuten, editors, (Macmillan Publishers Limited, 2013), pp. 157-183.
[65] V. Smil, *Power Density: A Key to Understanding Energy Sources and Uses*, (MIT Press, Cambridge, 2015).
[66] L. Hirth, "The market value of variable renewables: The effect of solar wind power variability on their relative price," Energy Economics, **38**, 218-236 (2013). https://doi.org/10.1016/j.eneco.2013.02.004
[67] P.J. Heptonstall, and R.J.K. Gross, "A systematic review of the costs and impacts of integrating variable renewables into power grids," Nature Energy, **6**(1), 72-83 (2021). https://doi.org/10.1038/s41560-020-00695-4
[68] NEA (2018), Measuring Employment Generated by the Nuclear Power Sector, OECD Publishing, Paris.
[69] D. de Solla Price, "Gears from the Greeks. The Antikythera Mechanism: A Calendar Computer from ca. 80 B.C." Transactions of the American Philosophical Society, **64**(7), 1–70 (1974). https://doi.org/10.2307/1006146
[70] J.H. Seiradakis, and M.G. Edmunds, "Our current knowledge of the Antikythera Mechanism," Nature Astronomy, **2**(1), 35-42 (2018). https://doi.org/10.1038/s41550-017-0347-2
[71] T. Freeth, "Decoding an Ancient Computer," Scientific American, **301**(6), 76–83 (2009). http://www.jstor.org/stable/26001660

ПЕРСПЕКТИВА МАЛИХ МОДУЛЬНИХ РЕАКТОРІВ: ЦІЛЬОВЕ ДОСЛІДЖЕННЯ ДЛЯ ГРЕЦІЇ

Олександр Хронеос[a,b], Аспасія Даскалопулу[a], Іоанніс Гулатіс[a], Руслан В. Вовк[c], Лефтері Х. Цукалас[d]
[a]Кафедра електротехніки та комп'ютерної інженерії, Університет Фессалії, 38333 Волос, Греція
[b]Відділення матеріалів, Імперський коледж Лондона, Великобританія
[c]Харківський національний університет імені В. Н. Каразіна, Україна
[d]Факультет ядерної інженерії, Університет Пердью, США

Глобальні зусилля до декарбонізації посилюються, але перехід до зеленої економіки має високу ціну, яка, за деякими оцінками складати приблизно 3,5 трильйона доларів щорічних інвестицій, більшість з яких є початковими. Це створює навантаження на економіки, що розвиваються, які володіють викопними природними ресурсами, тому що, відмовляючись від них, вони стають все більш залежними від імпортованої енергії, що пов'язане з високою ціною, на додаток до витрат, понесених їхніми зусиллями з переходу на відновлювані джерела енергії. Ядерна технологія виробляє диспетчеризований і безперебійний водень, тепло та електроенергію, які можуть покрити вимоги до базового навантаження, і інтерес до її впровадження зростає. Малі модульні реактори (ММР, англ. SMR) пропонують ряд переваг, особливо для країн з обмеженим ядерним досвідом. Тут ми коротко оцінюємо поточний стан систем SMR і розглядаємо їхні переваги та недоліки з акцентом на їхнє потенційне впровадження в Греції. В огляді обговорюється історія, поточний стан і можливе майбутнє включення SMR в новий енергетичний комплекс Греції.

Ключові слова: *малий модульний реактор; атомна енергетика; торій*

East European Journal of Physics. 2. 27–37 (2025)
DOI: 10.26565/2312-4334-2025-2-03 ISSN 2312-4334

BARROW HOLOGRAPHIC DARK ENERGY WITHIN SAEZ-BALLESTER SCALAR FIELD AND LYRA GEOMETRY

Vilas Raut[a], **Dhiraj Rautkar**[b]
[a]*Department of Mathematics, M. M. Mahavidyalaya, Darwah, Dist. Yavatmal-India*
[b]*Department of Mathematics, PRMIT&R, Badnera-Amaravati, India*
[*]*Corresponding Author e-mail: dvrautkar@gmail.com*
Received January 28, 2025; revised March 25, 2025; accepted March 30, 2025

This paper investigates the dynamical behavior of hypersurface homogeneous spacetime cosmological models within the framework of the scalar-tensor theory of gravitation formulated by Saez and Ballester (Phys. Lett. A, 113, 467 1986) in Lyra geometry. We present two cosmological models derived from this theory by solving the field equations using: (i) Special law of variation for Hubble's parameter and (ii) the proportional relationship between the shear scalar σ^2 and scalar expansion θ as described by Collins et al. (Gen. Rel. Grav. 12, 805 1980). For each model, we evaluate key dynamical parameters, including the equation of state (EoS) parameter, the deceleration parameter, the statefinder parameter, and the total energy density parameter of dark energy. Additionally, we determine the scalar field in both models. Our findings indicate that these models describe an accelerated expansion of the universe, with theoretical results showing reasonable agreement with observational data.

Keywords: *Hypersurface Homogeneous space-time; Holographic dark energy; Scalar-Tensor Theory of Gravitation*

PACS: 04.20.Jb, 04.50.Kd, 98.80.Cq, 98.80.Jk

1. INTRODUCTION

The recent observational studies have given evidence for the accelerated expansion of the universe [1, 2] and fluctuation of Cosmic Microwave Background Radiation (CMBR) [3], Sloan Digital Sky Survey (SDSS) [4], Wilkinson Microwave Anisotropy Probe (WMAP) [5], Large Scale Structure (LSS) [6], Baryonic Acoustic Oscillations [7], Gravitational Lensing [8] etc. It has also been suggested that the main reason for this is an exotic negative pressure named as 'dark energy'. It is surmised that the universe embedded of 68.3% dark energy as well as 26.8% dark matter. There have been numerous other dark energy models proposed, including quintessence [9], phantom [10], quintom [11], tachyon [12], ghost [13], K-essence [14], phantom [15], Chaplygin gas [16], polytropic gas [17] and holographic dark energy (HDE) [18] and many more to explain the accelerated expansion of the universe. To explain this accelerated expansion of the universe two different approaches have been advocated: to construct different dark energy candidates and to modify Einstein's theory of gravitation.

Very recently, a holographic dark energy model has been conjectured to explain the dark energy (Thomas [19], Horaya and Minic [20]). Li [18] has constructed a viable holographic dark energy model based on the holographic principle of the quantum gravity theory. Brans-Dicke (BD) [21] and Saez-Ballester (SB) [22] scalar tensor theories of gravitations. Therefore, there have been several investigations of DE cosmological model in the above alternative theories of gravitation to explain DE models by studying their dynamical aspects. In most of the above cases, the researchers concentrated on the anisotropic Bianchi type DE models. Recently, Naidu et al., [24] discussed Kaluza Klein FRW dark energy models in Saez-Ballester theory of gravitation. Oliveros et al., [25] investigated Barrow holographic dark energy [26, 27] with Granda-Oliveros cutoff [30]. In this study, we focus on the scalar-tensor theory of gravity proposed by Saez- Ballester. In the Saez-Ballester theory, a scalar field ϕ is introduced alongside the metric tensor field, modifying gravitational interactions. This modification can lead to attractive or repulsive forces, depending on the form of the scalar field and its coupling.. This inclusion aims to more fully incorporate Mach's principle. Saez and Ballester later developed a new scalar-tensor theory where the metric of spacetime is simply coupled with a dimensionless scalar field. However, this theory includes an antigravity regime. The gravitational action was first introduced by Saez [23] and is given by:

$$I = \int_{\Sigma} (L + GL_m)\sqrt{-g}d^4x \tag{1}$$

where L_m is the matter Lagrangian. Varying this gravitational action, δI, leads to the field equations of the Saez-Ballester scalar-tensor theory and Lyra geometry:

$$G_{ij} + \frac{3}{2}\psi_i\psi_j - \frac{3}{4}g_{ij}\psi_k\psi^k = -\left(T_{ij} + \bar{T}_{ij}\right) + \omega\phi^n\left(\phi_{.i}\phi_{.j} - \frac{1}{2}g_{ij}\phi_{.k}\phi^{.\hat{k}}\right) \tag{2}$$

The scalar field ϕ satisfies the following equation:

Cite as: V. Raut, D. Rautkar, East Eur. J. Phys. 2, 27 (2025), https://doi.org/10.26565/2312-4334-2025-2-03

$$2\phi^n \phi^{,i}_{,i} + n\phi^{n-1}\phi_{,k}\phi^{,k} = 0 \tag{3}$$

Here, $G_{ij} = R_{ij} - \frac{1}{2}Rg_{ij}, R_{ij}$ is the Ricci tensor, R is the Ricci scalar, ψ^i is displacement vector field of Lyra's geometry w is a dimensionless constant, and T_{ij} and $\bar{T}_{ij}$ are the energy-momentum tensor of matter and Barrow holographic dark energy, respectively. Relativistic units $8\pi G = c = 1$ are used in these equations.

2. BARROW HOLOGRAPHIC DARK ENERGY

A new proposal that has recently caught the attention of the community is the so-called Barrow holographic dark energy (BHDE) [26], which has its roots in the idea introduced by Barrow [27], inspired by illustrations of the COVID-19 virus. Barrow proposed that quantum gravitational effects modify the black hole Bekenstein-Hawking entropy [28, 29] by introducing a fractal structure for the geometry of the horizon. In this section, we delve into the theoretical framework and cosmological implications of an interacting Barrow holographic dark energy (BHDE) model. The concept of BHDE was introduced by Barrow, building upon the modification of black hole horizon entropy represented by:

$$S_B = \left(\frac{A}{A_0}\right)^{1+\frac{\Delta}{2}}, 0 \leq \Delta \leq 1 \tag{4}$$

where A denotes the standard horizon area and A_0 is the Planck area. The parameter Δ quantifies the effect of quantum deformation on the structure of the horizon. In particular, $\Delta = 1$ represents maximal deformation, whereas $\Delta = 0$ corresponds to the simplest horizon structure, recovering the conventional Bekenstein-Hawking entropy. In the area of cosmology, this modified entropy leads to a holographic dark-energy (HDE) model described by:

$$\rho_B = CL^{\Delta-2}, \tag{5}$$

where C is an unknown parameter with dimensions $[L]^{-2-\Delta}$. This formulation extends beyond the standard HDE scenario ($\Delta = 0$), where $\rho_D \propto L^{-2}$. The BHDE model is thus a more comprehensive framework, particularly focusing on cases where $\Delta > 0$ and quantum deformation effects are significant. The energy density of BHDE, employing the Hubble horizon $\left(H^{-1}\right)$ as the IR cutoff (L), is given by:

$$\rho_B = CH^{2-\Delta} \tag{6}$$

The choice of the Hubble horizon as the IR cut-off is noteworthy because of its inherent relevance in cosmology. Various models of HDE have explored different IR cut-off, each influencing cosmological dynamics differently. For instance, Li demonstrated that selecting the future event horizon as the IR cut-off yields an accelerating universe in the absence of interaction between dark matter (DM) and dark energy (DE), whereas the particle horizon leads to a decelerating universe. Recent attention has been drawn to the BHDE model within the context of the Granda-Oliveros (G-O) cutoff [30], which incorporates both the square of the Hubble parameter and its time derivative:

$$L_{\mathbb{R}} = \left(\alpha H^2 + \gamma \dot{H}\right)^{-1/2} \tag{7}$$

where α and γ are arbitrary dimensionless parameters. Recent studies have further explored BHDE with the G-O length as the IR cutoff, considering BHDE as a dynamical vacuum and accounting for interactions between matter and dark energy sectors. We are implementing the BHDE density with the G-O IR cutoff, where the holographic DE density ρ_B is given by:

$$\rho_B = 3M_p^2 \left(\alpha H^2 + \gamma \dot{H}\right)^{1-\frac{\Delta}{2}} \tag{8}$$

Here, α and β are parameters with dimensions $[L]^{\frac{2\Delta}{\Delta-2}}$, ensuring the correct dimensionality of ρ_B.

Unlike the original HDE model where $\Delta = 0$, the parameter C in equation (6) is replaced by $3M_p^2$. The barotropic equation of state $p_B = \omega_B \rho_B$, the equation of state HDE parameter is obtained as

$$\omega_B = -1 - \frac{2\alpha H\dot{H} + \gamma\ddot{H}}{3H\left(\alpha H^2 + \gamma \dot{H}\right)} \tag{9}$$

The above discussion and investigations, we consider in this paper the minimally interacting holographic dark energy model in hypersurface homogeneous spacetime within the framework of the SB scalar-tensor theory of gravitation. This work is organized as follows: In Sect. 2, we derive the SB field equations with the help of a hypersurface homogeneous spacetime metric in the presence of two minimally interacting fields: dark matter and holographic dark energy. Sect. 3 is devoted to the solution of SB field equations with the help of a special law of variation for Hubble's parameter proposed by Berman [31] and using physically relevant conditions. In Sect. 4, physical and kinematical parameters of the model are also computed and discussed. The last section contains some concluding remarks.

3. METRIC AND FIELD EQUATIONS

We consider the hypersurface homogeneous space time as follows

$$ds^2 = -dt^2 + A^2dx^2 + B^2\left[dy^2 + \Sigma^2(y,k)dz^2\right] \tag{10}$$

where A and B are functions of time (t) and $\Sigma^2(\mathrm{y,k}) = \sin y, y, \sinh y$ for $k = 1, 0, -1$, respectively. T_{ij} and $\bar{T}_{ij}$ are energy momentum tensors for matter and holographic dark energy, respectively. which are defined as

$$\begin{aligned} T_{ij} &= \rho_m u_i u_j \\ \bar{T}_{ij} &= (\rho_B + p_B)\, u_i u_j + g_{ij} p_B \end{aligned} \tag{11}$$

Here ρ_m and ρ_h are the energy densities of matter and barrow holographic dark energy and p_B is the pressure of holographic dark energy.

In a co-moving coordinate system, the field equation (2) for the metric (10), using equation (11) can be written as

$$\frac{2\ddot{B}}{B} + \frac{\dot{B}^2}{B^2} + \frac{k}{B^2} + \frac{3}{4}\beta^2 + \frac{\omega}{2}\phi^n\dot{\phi}^2 = -p_B \tag{12}$$

$$\frac{\ddot{A}}{A} + \frac{\ddot{B}}{B} + \frac{\dot{A}}{A}\frac{\dot{B}}{B} + \frac{3}{4}\beta^2 + \frac{\omega}{2}\phi^n\dot{\phi}^2 = -p_B \tag{13}$$

$$2\frac{\dot{A}\dot{B}}{AB} + \frac{\dot{B}^2}{B^2} + \frac{k}{B^2} - \frac{3}{4}\beta^2 - \frac{\omega}{2}\phi^n\dot{\phi}^2 = (\rho_m + \rho_B) \tag{14}$$

$$\ddot{\phi} + \dot{\phi}\left(\frac{\dot{A}}{A} + 2\frac{\dot{B}}{B}\right) + \frac{n}{2}\frac{\dot{\phi}^2}{\phi^n} = 0 \tag{15}$$

where an overhead dot denotes differentiation with respect to t. Now the average scale factor and the volume of the universe are defined as

$$V = AB^2 \tag{16}$$

Subtracting (12) from (13), we get

$$\frac{\ddot{A}}{A} - \frac{\ddot{B}}{B} + \frac{\dot{A}\dot{B}}{AB} - \frac{\dot{B}^2}{B^2} - \frac{k}{B^2} = 0 \tag{17}$$

We obtain

$$\frac{\dot{A}}{A} - \frac{\dot{B}}{B} = \frac{c_1}{V} + \frac{1}{V}\int\left[\frac{k}{B^2}\right]Vdt \tag{18}$$

where λ represents a constant of integration.

Taking $k = 0$, the equation (18) leads to

$$\frac{\dot{A}}{A} - \frac{\dot{B}}{B} = \frac{c_1}{V} \tag{19}$$

From equation (19), we obtain

$$A^3 = \frac{V}{c}\exp\left(\int\frac{c_1}{V}dt\right) \tag{20}$$

The directional Hubble parameter in the direction of x, y, and z axes respectively are as follows

$$H_x = \frac{\dot{A}}{A}, H_y = H_z = \frac{\dot{B}}{B} \tag{21}$$

The average Hubble parameter is

$$H = \frac{1}{3}\left(\frac{\dot{A}}{A} + 2\frac{\dot{B}}{B}\right) \tag{22}$$

The expressions for the scalar expansion θ and the shear scalar σ^2 are

$$\theta = 3H \tag{23}$$

$$\sigma^2 = \frac{1}{2}\left(\sum_{i=1}^{3}H_i^2 - 3H^2\right) \tag{24}$$

The average anisotropy parameter is

$$A_B = \frac{1}{3}\sum_{i=1}^{3}\left(\frac{\Delta H_i}{H}\right)^2 \tag{25}$$

where $\Delta H_i = H_i - H, i = 1, 2, 3$ obtained as

$$\dot{\rho}_m + \dot{\rho}_B + 3H\left(\rho_m + \rho_B + p_B\right) = 0 \tag{26}$$

The continuity equation of the matter is

$$\dot{\rho}_m + 3H\rho_m = 0 \tag{27}$$

The continuity equation of the HDE is

$$\dot{\rho}_B + 3H\left(\rho_B + p_B\right) = 0 \tag{28}$$

4. SOLUTIONS AND THE MODEL

We have three equations (12)-(14) in four unknowns A, B, p_B, ρ_B. To solve the system completely, we need one extra condition. We solve the field equations for following physical conditions.

1. Special law of variation for Hubble's parameter;
2. Shear scalar proportional to expansion scalar.

4.1. Model Special law of variation for Hubble's parameter

We consider the relation between H and a, which was proposed by Berman (1983)

$$H = na^{\frac{-1}{n}} \tag{29}$$

where $n \geq 0$ are constants.

From equations (28) and (30) we obtain

$$q = -1 + \frac{1}{n} \tag{30}$$

Now, using Eq. (30) and Eq. (31), the solution of Eq. (28) gives the law of variation of the average scale factor of the form

$$a(t) = (t+b)^n, n \neq 0. \tag{31}$$

Using equation (31), we get

$$V = a^3(t) = (t+b)^{3n} \tag{32}$$

Now from equations (17), (21) and (32) we obtain

$$\begin{aligned} A(t) &= c_2^{\frac{2}{3}}(t+b)^n \exp\left(\frac{2c_1}{3(1-3n)}(t+b)^{1-3n}\right), \\ B(t) &= c_2^{\frac{-1}{3}}(t+b)^n \exp\left(-\frac{c_1}{3(1-3n)}(t+b)^{1-3n}\right) \end{aligned} \tag{33}$$

Now from equation (33) in equation (15) we obtain the scalar field as

$$\phi^{\frac{n+2}{2}} = \left(\frac{n+2}{2}\right)\left[\frac{\phi_0}{3(1-3n)}(t+b)^{1-3n}\right] \tag{34}$$

where ϕ_0 are constants of integration.

The directional and average Hubble parameter is

$$\begin{aligned} H_x &= \frac{n}{(t+b)} + \frac{2c_1}{3}(t+b)^{-3n} \\ H_y = H_z &= \frac{n}{(t+b)} - \frac{c_1}{3}(t+b)^{-3n} \end{aligned} \tag{35}$$

And

$$H = \frac{n}{(t+b)} \tag{36}$$

The values of the directional parameters are infinite at $t = 0$ and tend to zero as $t \to \infty$. The mean Hubble parameter $H \to 0$ as $t \to \infty$ i.e. the rate of expansion of the universe is decreasing.

The scalar expansion θ is

$$\theta = 3\frac{n}{(t+b)} \tag{37}$$

The average anisotropy parameter is

$$A_B = \frac{1}{3}\sum_{i=1}^{3}\left(\frac{H_i - H}{H}\right)^2 = \frac{2c_1^2}{9}(t+b)^{2-6n} \tag{38}$$

The shear scalar σ^2 is

$$\sigma^2 = \frac{c_1^2}{2}(t+b)^{-6n} \tag{39}$$

It is found that $\frac{\sigma^2}{\theta^2} \neq 0$ and the anisotropy parameter do not vanish except at n = 1.

Applying the conservation condition for the left-hand side of equation (2), we get

$$\beta\left(\dot{\beta} + \beta\left[\frac{\dot{A}}{A} + 2\frac{\dot{B}}{B}\right]\right) = 0.$$

From Eq. (43) by integrating, we have

$$\beta = \beta_0(t+b)^{-3n}$$

Using equation (32) in equation (28) we get the energy density of dark matter as

$$\rho_m = \rho_0(t+b)^{-3n} \tag{40}$$

where $\rho_0 > 0$ is a real constant of integration.

Using equation (36) in equation (28) the BHDE density is written as,

$$\rho_B = 3M_p^2\left(\frac{n^2(\alpha - n\gamma)}{(t+b)^2}\right)^{1-\frac{\Delta}{2}} \tag{41}$$

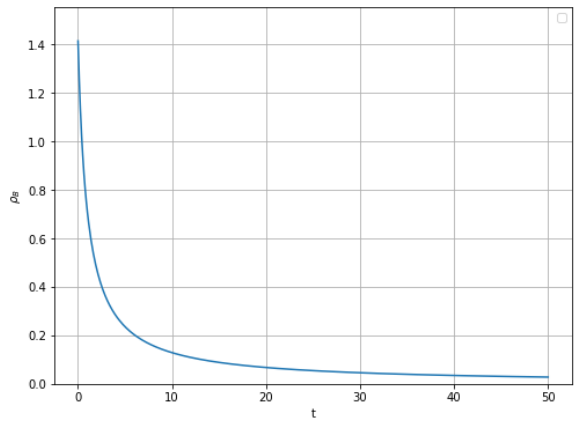

Figure 1. Plot of Density of Barrow HDE vs time, the energy density of Hypersurface homogeneous Barrow HDE model in Granda-Oliveros cut-off decreases.

Using equations (32), (33) in equation (13) we get, the pressure of Barrow HDE as

$$p_B = \frac{n^2}{(t+b)^2} + \left(\frac{2nc_1}{3} + \frac{3}{4}\beta_0\right)(t+b)^{-3n} + \left(\frac{\omega\phi_0^2}{2} + \frac{c_1^2}{9}\right)(t+b)^{-6n} \tag{42}$$

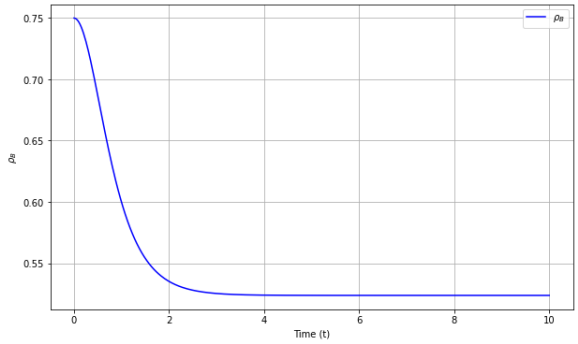

Figure 2. Plot of pressure of BHDE vs time, the pressure p_B of BHDE decreases with time and approaches zero as time goes to infinity.

Using equations (41), (42) and the barotropic equation of state $p_B = \omega_B \rho_B$, the equation of state BHDE parameter is obtained as

$$\omega_B = -1 - \frac{(2-\Delta)(2\alpha H\dot{H} + \beta\ddot{H})}{6H\left(\alpha H^2 + \beta\dot{H}\right)} \tag{43}$$

EoS parameter is obtained as,

$$\omega_B = -1 + \frac{(2-\Delta)}{3n}. \tag{44}$$

From equation (44) shows (i) For small Δ and n : The dark energy behaves less like a cosmological constant and more like matter or radiation, with ω_B greater than -1. (ii) For large Δ and n : The system behaves like a cosmological constant with ω_B approaching -1. (iii) For intermediate values of Δ and n : ω_B transitions smoothly between matter-like and dark energy-like behavior, offering a flexible model for the evolution of the universe.

This form of ω_B in the Barrow holographic dark energy model provides a way to model the evolution of dark energy and its impact on the universe's expansion, with flexibility to explain both early-time and late-time acceleration.

Matter density parameter Ω_m and the holographic dark energy parameter Ω_B are given by

$$\Omega_m = \frac{\rho_m}{3H^2} \text{ and } \Omega_B = \frac{\rho_B}{3H^2} \tag{45}$$

Using equations (36), (40), (41) and (45) we get the overall density parameter as

$$\begin{aligned}\Omega &= \Omega_m + \Omega_B \\ &= \frac{3n^2}{(t+b)^2} + \frac{1}{3n^2}\left(\frac{\omega\phi_0^2}{2} + \frac{5c_1^2}{9} + \frac{3}{4}\beta_0\right)(t+b)^{2-6n} + \frac{kc_2^{\frac{2}{3}}}{3n^2}(t+b)^{2(1-n)}\exp\left(\frac{2c_1}{3(1-3n)}(t+b)^{1-3n}\right)\end{aligned} \tag{46}$$

From equation (46), the total energy density parameter of Hypersurface homogeneous Barrow HDE model in Granda-Oliveros cut-off decreases below 1, indicating an open universe.

4.2. Model for Shear scalar proportional to expansion scalar

The shear scalar σ^2 is proportional to scalar expansion so that we can take (Collins et al., [32])

$$A = B^n \tag{47}$$

where $n \neq 1$ is a positive constant and preserves the isotropic character of the spacetime.

Using the equation (47) in the equation (17), we get

$$\frac{\ddot{B}}{B} + (n+1)\frac{\dot{B}^2}{B^2} = \frac{k}{(n-1)B^2} \tag{48}$$

We get

$$2\ddot{B} + 2(n+1)\frac{\dot{B}^2}{B} = \frac{2k}{(n-1)B} \tag{49}$$

equation (49) further reduces to

$$\dot{B}^2 = \frac{k}{n^2-1} + CB^{-2n-2} \tag{50}$$

where C is a constant of integration and for $n = -2$ we get

$$\begin{aligned} B &= \cosh\left(\ell_1 t + \ell_2\right)^{1/3} \\ A &= \cosh\left(\ell_1 t + \ell_2\right)^{n/3} \end{aligned} \tag{51}$$

The spatial volume is given by

$$V = \left[\cosh\left(\ell_1 t + \ell_2\right)\right]^{\frac{n+2}{3}} \tag{52}$$

The average Hubble parameter is

$$H = \frac{1}{3}\left(\frac{\dot{A}}{A} + 2\frac{\dot{B}}{B}\right) = \frac{(n+2)}{9} \cdot \tanh\left(\ell_1 t + \ell_2\right) \tag{53}$$

The values of the directional parameters are infinite at $t = 0$ and tend to zero as $t \to \infty$. The mean Hubble parameter $H \to 0$ as $t \to \infty$ i.e. the rate of expansion of the universe is decreasing.

Now using equations (51) in equation (15) we obtain the scalar field as

$$\phi^{\frac{n+2}{2}} = \left(\frac{n+2}{2}\right) \operatorname{sech}^{\frac{2(n+2)}{3}}\left(\ell_1 t + \ell_2\right) + \phi_0 \tag{54}$$

where ϕ_0 are constants of integration. Taking $\phi_0 = 0$, we have

$$\phi^{\frac{n+2}{2}} = \left(\frac{n+2}{2}\right) \operatorname{sech}^{\frac{2(n+2)}{3}}\left(\ell_1 t + \ell_2\right) \tag{55}$$

The scalar expansion θ is

$$\theta = 3H = (n+2)\tanh\left(\ell_1 t + \ell_2\right) \tag{56}$$

The shear scalar σ^2 is

$$\sigma^2 = \frac{3}{2}\Delta H^2 = \left[\frac{(n-1)}{3} \cdot \tanh\left(\ell_1 t + \ell_2\right)\right]^2 \tag{57}$$

The average anisotropy parameter is

$$A_B = \frac{2(n-1)^2}{(n+2)^2} \tag{58}$$

It is found that $\frac{\sigma^2}{\theta^2} \neq 0$ and the anisotropy parameter do not vanish except at n = 1. We observe that at $t = 0$ the mean anisotropy parameter is not zero i.e. in the early stage the universe found to be anisotropic. The shear scalar $\sigma = 0$ as $t \to \infty$ i.e. at late time matter has no shear.

Using equation (52) in equation (27) we get the energy density of dark matter as

$$\rho_m = \rho_0 \left[\operatorname{sech}\left(\ell_1 t + \ell_2\right)\right]^{\frac{n+2}{3}} \tag{59}$$

where $\rho_0 > 0$ is a real constant of integration.

Using equation (54) in equation (8) we get, the density of Barrow HDE as

$$\rho_B = 3M_p^2\left[\frac{(n+2)}{9}\left(\frac{\alpha(n+2)}{81} - \frac{\gamma\ell_1}{9}\right)\tanh^2\left(\ell_1 t - \ell_2\right) + \frac{\gamma(n+2)\ell_1}{9}\right]^{1-\frac{\Delta}{2}} \tag{60}$$

Using equations (51) and (52) in equation (13) we get

$$\begin{aligned} p_B = -M_p^2 \frac{k_1 \tanh^2\left(\ell_1 t + \ell_2\right) + k_2\right]^{1-\frac{\Delta}{2}} \cdot \left(1 - \frac{\Delta}{2}\right) \cdot 2k_1 \tanh\left(\ell_1 t + \ell_2\right) k_3}{\frac{n+2}{3}\tanh\left(\ell_1 t + \ell_2\right)} \\ - \left[3k_1 \tanh^2\left(\ell_1 t + \ell_2\right) + 3k_2\right]^{1-\frac{\Delta}{2}} \end{aligned} \tag{61}$$

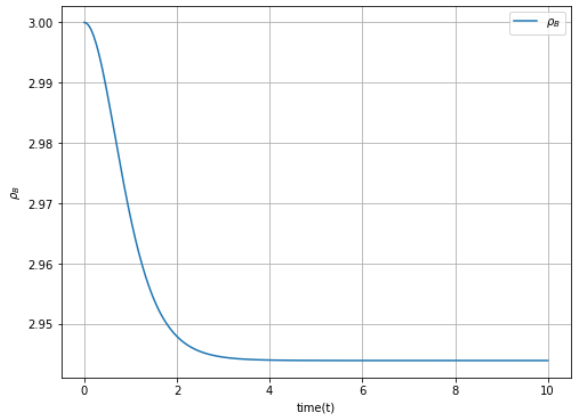

Figure 3. Plot of Density of Barrow HDE vs time, the energy density of Hypersurface homogeneous Barrow HDE model in Granda-Oliveros cut-off decreases.

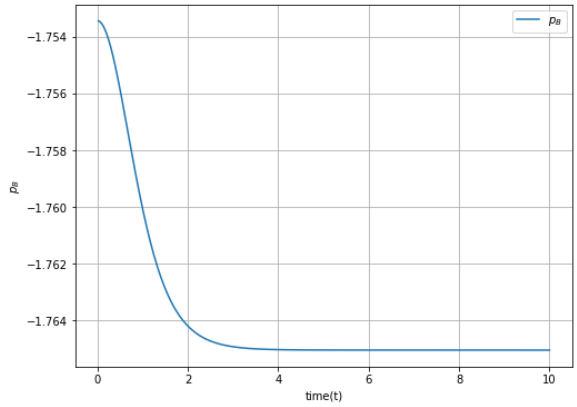

Figure 4. Plot of pressure of BHDE vs time, the pressure p_B of BHDE decreases with time and approaches zero as time goes to infinity.

where

$$k_1 = \frac{n+2}{9}\left(\frac{\alpha(n+2)}{81} - \frac{\gamma\ell_1}{9}\right), k_2 = \frac{\gamma(n+2)\ell_1}{9}, k_3 = \left|\left(1 - \tanh^2(\ell_1 t + \ell_2)\right)\cdot \ell_1\right|$$

Using equation (53) in equation (43) the equation of state BHDE parameter is obtained as

$$\omega_B = -1 - \frac{(2-\Delta)\ell_1\left(2\alpha\frac{n+2}{9} - 2\gamma\right)\operatorname{sech}^2(\ell_1 t + \ell_2)}{6\left[\alpha\left(\frac{(n+2)^2}{81}\right)\tanh^2(\ell_1 t + \ell_2) + \gamma\left(\frac{n+2}{9}\right)\operatorname{sech}^2(\ell_1 t + \ell_2)\right]} \tag{62}$$

Matter density parameter Ω_m and the holographic dark energy parameter Ω_h are given by

$$\Omega_m = \frac{\rho_m}{3H^2} \text{ and } \Omega_B = \frac{\rho_B}{3H^2} \tag{63}$$

Using equations (53), (59), (60) and (63) we get the overall density parameter as

$$\begin{aligned}\Omega &= \Omega_m + \Omega_B \\ &= \frac{27M_p^2\rho_0\left[\operatorname{sech}(\ell_1 t + \ell_2)\right]^{\frac{n+2}{3}}\left[\frac{(n+2)}{9}\left(\frac{\alpha(n+2)}{81} - \frac{\gamma\ell_1}{9}\right)\tanh^2(\ell_1 t - \ell_2) + \frac{\gamma(n+2)\ell_1}{9}\right]^{1-\frac{\Delta}{2}}}{(n+2)^2\tanh^2(\ell_1 t + \ell_2)}\end{aligned} \tag{64}$$

From equation (64) show how the density parameter evolves as a function of time. Here are the key features we expect: 1. Early Evolution: When t is small, Ω may be larger than 1 , indicating a matter-dominated or radiation-dominated

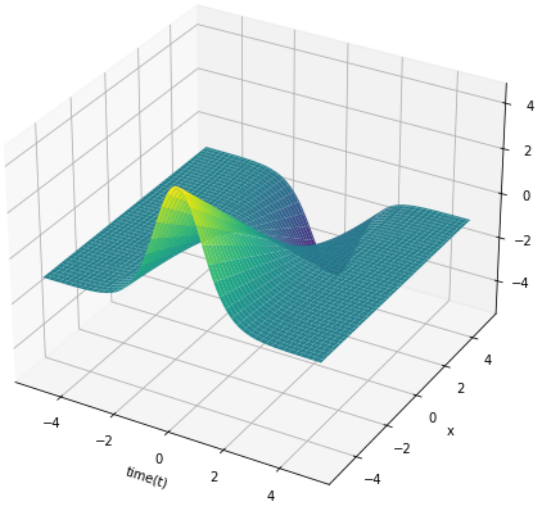

Figure 5. Plot of EoS parameter versus cosmic time t

universe. 2. Transition Period: As time progresses, the function will likely show a smooth transition where the contribution from dark energy becomes dominant. 3. Late Evolution: For large values of t, Ω might approach 1 , signifying that the universe has reached a state dominated by dark energy or a cosmological constant, and the expansion is accelerating. From figure (5) observed that the regime of the EOS parameter ω_B changes with Δ, transitioning from a phantom energy regime $\omega_B < -1$) for $\Delta < 2$ to a vacuum energy regime ($\omega_B = -1$) for $\Delta = 2$ and then to a quintessence regime ($\omega_B > -1$) for $\Delta > 2$. The specific plots of ω_B against t for different Δ values will illustrate these transitions and provide a visual understanding of the behavior of the parameter in different cosmological regimes.

From equation (57), it is clear that the expansion scalar is decreasing function of time which approaches constant at large time. The universe is expanding with constant rate at the present. Scalar expansion versus time. The scalar expansion (θ) and the shear scalar (σ^2) diverge with $t \to 0$. The parameters σ^2 and θ are a decreasing function of time t and vanish as $t \to \infty$. The deceleration parameter tends to be negative at $t \to \infty$, i.e. the universe is accelerating at present, which is in accordance with the observational result. One can see that the mean anisotropic parameter is not zero i.e. the model is anisotropic. In this regime, we also note that the anisotropy of the fluid does not act so as to increase the anisotropy of the expansion. The density and the EoS parameter are dynamical quantities $\rho_B \to 0, \omega \to$ -1 as $t \to \infty$. i.e. the model represents a vacuum universe and is mathematically equivalent to cosmological constant.

5. CONCLUSIONS

In this paper we have investigated a hypersurface homogeneous space-time filled with two minimally interacting fluids, dark matter and Barrow holographic dark energy in the Saez-Ballester scalar-tensor theory of gravitation in Lyra gemetry. To obtain exact solutions of the Saez-Ballester field equations we use (i) models of the constant deceleration parameter of the universe and (ii) the relation between the scalar field ϕ and the average scale factor. We have also computed some of the physical and kinematical parameters of the model, and their cosmological significance is described. It is found that $\frac{\sigma^2}{\sigma^2} \neq 0$ and the anisotropy parameter do not vanish except at $n = 1$. The coincidence parameter is a decreasing function of time. The spatial volume (V) of the universe increases with cosmic time so that there is a spatial expansion of the universe with time t. The parameters H, θ, σ^2 all diverge at the initial epoch, i.e.at $t = 0$ and they all tend to zero for infinite time. Also, the physical parameters $\rho_m, \rho_h, p_B, \phi$ diverge for $t = 0$ while they all vanish for infinite time. Therefore, the model has a big bang singularity at $t = 0$. We can observe that $A_B \neq 0$ and this indicates that this present model is anisotropic throughout the evaluation of the universe. The average anisotropy parameter and shear scalar vanish for $n = 1$. This shows that the universe will become shear free and isotropic in finite time. It may be observed that the EoS parameter turns out to be vacuum universe and mathematically equivalent to cosmological constant for $\Delta = 2$. Also, the average density decreases with time.

Acknowledgments

The authors would like to acknowledge the deep sense of gratitude to the anonymous referees for valuable suggestion for improvement and up gradation of the manuscript.

ORCID

Vilas Raut, https://orcid.org/0009-0003-3639-9578; **Dhiraj Rautkar**, https://orcid.org/0009-0007-9934-9147

REFERENCES

[1] A. G. Riess, A. V. Filippenko, P. Challis, *et al.*, "Observational evidence from supernovae for an accelerating universe and a cosmological constant," The Astronomical Journal, **116**(3), 1009 (1998). https://doi.org/10.1086/300499

[2] S. Perlmutter, G. Aldering, M.D. Valle, *et al.*, "Discovery of a supernova explosion at half the age of the universe," Nature, **391**(6662), 51–54 (1998). https://doi.org/10.1038/34124

[3] D.N. Spergel, L. Verde, H.V. Peiris, *et al.*, "First-year Wilkinson Microwave Anisotropy Probe (WMAP) observations: Determination of cosmological parameters," The Astrophysical Journal Supplement Series, **148**(1), 175 (2003). https://doi.org/10.1086/377226

[4] U. Seljak, A. Makarov, P. McDonald, *et al.*, "Cosmological parameter analysis including SDSS Lyman α forest and galaxy bias: Constraints on the primordial spectrum of fluctuations, neutrino mass, and dark energy," Physical Review D—Particles Fields, Gravitation, and Cosmology, **71**(10), 103 515 (2005). https://doi.org/10.1103/PhysRevD.71.103515

[5] C.L. Bennett, R.S. Hill, G. Hinshaw, M.R. Nolta, N. Odegard, L. Page, D.N. Spergel, *et al.*, "First-year Wilkinson Microwave Anisotropy Probe (WMAP) observations: Foreground emission," The Astrophysical Journal Supplement Series, **148**(1), 97 (2003). https://doi.org/10.1086/377252

[6] M. Tegmark, M.R. Blanton, M.A. Strauss, et al., The three-dimensional power spectrum of galaxies from the Sloan Digital Sky Survey," The Astrophysical Journal, **606**(2), 702 (2004). https://doi.org/10.1086/382250

[7] D.J. Eisenstein, I. Zehavi, D.W. Hogg, *et al.*, "Detection of the baryon acoustic peak in the large-scale correlation function of SDSS luminous red galaxies," The Astrophysical Journal, **633**(2), 560 (2005). https://doi.org/10.1086/468499

[8] C.R. Contaldi, H. Hoekstra, and A. Lewis, "Joint cosmic microwave background and weak lensing analysis: Constraints on cosmological parameters," Physical Review Letters, **90**(22), 221303 (2003). https://doi.org/10.1103/PhysRevLett.90.221303

[9] R.R. Caldwell, R. Dave, and P.J. Steinhardt, "Cosmological imprint of an energy component with general equation of state," Physical Review Letters, **80**(8), 1582 (1998). https://doi.org/10.1103/PhysRevLett.80.1582

[10] R.R. Caldwell, "A phantom menace? Cosmological consequences of a dark energy component with super-negative equation of state," Physics Letters B, **545**(1-2), 23–29 (2002). https://doi.org/10.1016/S0370-2693(02)02589-3

[11] B. Feng, X. Wang, and X. Zhang, "Dark energy constraints from the cosmic age and supernova," Physics Letters B, **607**(1-2), 35–41 (2005). https://doi.org/10.1016/j.physletb.2004.12.045

[12] M. Setare, "The holographic dark energy in non-flat Brans–Dicke cosmology," Physics Letters B, **644**(2-3), 99–103 (2007). https://doi.org/10.1016/j.physletb.2006.11.070

[13] M. Malekjani, T. Naderi, and F. Pace, "Effects of ghost dark energy perturbations on the evolution of spherical overdensities," Monthly Notices of the Royal Astronomical Society, **453**(4), 4148–4158 (2015). https://doi.org/10.1093/mnras/stv1900

[14] T. Chiba, "Tracking k-essence," Physical Review D, **66**(6), 063514 (2002). https://doi.org/10.1103/PhysRevD.66.063514

[15] S. Nojiri, and S.D. Odintsov, "Quantum de Sitter cosmology and phantom matter," Physics Letters B, **562**(3-4), 147–152 (2003). https://doi.org/10.1016/S0370-2693(03)00439-6

[16] A. Kamenshchik, U. Moschella, and V. Pasquier, "An alternative to quintessence," Physics Letters B, **511**(2-4), 265–268 (2001). https://doi.org/10.1016/S0370-2693(01)00571-8

[17] K. Kleidis, and N.K. Spyrou, "Polytropic dark matter flows illuminate dark energy and accelerated expansion," Astronomy & Astrophysics, **576**, A23 (2015). https://doi.org/10.1051/0004-6361/201423759

[18] M. Li, "A model of holographic dark energy," Physics Letters B, **603**(1-2), 1–5 (2004). https://doi.org/10.1016/j.physletb.2004.10.014

[19] S. Thomas, "Holography stabilizes the vacuum energy," Physical Review Letters, **89**, 081301 (2002). https://doi.org/10.1103/PhysRevLett.89.081301

[20] P. Horava, and D. Minic, "Probable values of the cosmological constant in a holographic theory," Physical Review Letters, **85**(8), 1610 (2000). https://doi.org/10.1103/PhysRevLett.85.1610

[21] C. Brans, and R.H. Dicke, "Mach's principle and a relativistic theory of gravitation," Physical Review, **124**(3), 925 (1961). https://doi.org/10.1103/PhysRev.124.925

[22] D. Saez, and V. Ballester, "A simple coupling with cosmological implications," Physics Letters A, **113**(9), 467–470 (1986). https://doi.org/10.1016/0375-9601(86)90035-5

[23] D. Saez, "Variational formulation of two scalar-tetradic theories of gravitation," Physical Review D, **27**, 2839-2847 (1983). https://link.aps.org/doi/10.1103/PhysRevD.27.2839

[24] R. Naidu, Y. Aditya, K.D. Raju, T. Vinutha, and D. Reddy, "Kaluza-Klein FRW dark energy models in Saez-Ballester theory of gravitation," New Astronomy, **85**, 101564 (2021). https://doi.org/10.1016/j.newast.2021.101564

[25] A. Oliveros, M. Sabogal, and M.A. Acero, "Barrow holographic dark energy with Granda–Oliveros cutoff," The European Physical Journal Plus, **137**(7), 1–11 (2022). https://doi.org/10.1140/epjp/s13360-022-01612-5

[26] E.N. Saridakis, "Barrow holographic dark energy," Physical Review D, **102**(12), 123525 (2020). https://doi.org/10.1103/PhysRevD.102.123525

[27] J.D. Barrow, "The area of a rough black hole," Physics Letters B, **808**, 643 (2020). https://doi.org/10.1016/j.physletb.2020.135643

[28] J.D. Bekenstein, "Black holes and entropy," Physical Review D, **7**(8), 2333 (1973). https://doi.org/10.1103/PhysRevD.7.2333

[29] S.W. Hawking, "Particle creation by black holes," Communications in Mathematical Physics, **43**(3), 199–220 (1975). https://doi.org/10.1007/BF02345020

[30] L. Granda, and A. Oliveros, "Infrared cut-off proposal for the holographic density," Physics Letters B, **669**(5), 275–277 (2008). https://doi.org/10.1016/j.physletb.2008.09.065

[31] M. Berman, "A special law of variation for Hubble's parameter," Nuovo Cimento B Serie, **74**, 182–186 (1983).

[32] C.B. Collins, E.N. Glass, and D.A. Wilkinson, "Exact spatially homogeneous cosmologies," General Relativity and Gravitation, **12**(10), 805–823 (1980). https://doi.org/10.1007/BF00763318

ГОЛОГРАФІЧНА ТЕМНА ЕНЕРГІЯ БАРРОУ В СКАЛЯРНОМУ ПОЛІ САЄЗА-БАЛЛЕСТЕРА ТА ГЕОМЕТРІЇ ЛІРИ

Вілас Раут[a], **Дхірадж Рауткар**[b]

[a] *Департамент математики, М.М. Махавідьялая, Дарва, округ Яватмал, Індія*

[b] *Департамент математики, Інститут технологій і досліджень професора Рама Меге Баднера-Амараваті, Індія*

У цій статті досліджується динамічна поведінка гіперповерхневих однорідних просторово-часових космологічних моделей у рамках скалярно-тензорної теорії гравітації, сформульованої Саезом і Баллестером (Phys. Lett. A, 113, 467 1986) у геометрії Ліри. Ми представляємо дві космологічні моделі, отримані з цієї теорії шляхом вирішення рівнянь поля з використанням: (i) спеціального закону зміни для параметра Хаббла та (ii) пропорційного співвідношення між скалярним зсувом σ^2 і скалярним розширенням θ, як описано Коллінзом та ін. (Gen. Rel. Grav. 12, 805 1980). Для кожної моделі ми оцінюємо ключові динамічні параметри, включаючи параметр рівняння стану (EoS), параметр уповільнення, параметр вимірювача стану та параметр загальної густини енергії темної енергії. Додатково визначаємо скалярне поле в обох моделях. Наші висновки вказують на те, що ці моделі описують прискорене розширення Всесвіту, причому теоретичні результати демонструють розумну згоду з даними спостережень.

Ключові слова: *гіперповерхневий однорідний простір-час; голографічна темна енергія; Скалярно-тензорна теорія тяжіння*

EAST EUROPEAN JOURNAL OF PHYSICS. **2.** 38-42 (2025)
DOI:10.26565/2312-4334-2025-2-04 ISSN 2312-4334

PHOTOMETRIC FLICKERING OF THE CH Cyg IN 2018

Kh. M. Mikailov[a], R.T. Mammadov[b,c]*
[a]*Baku State University, Baku, AZ-1148, Azerbaijan*
[b]*Batabat Astrophysics Observatory, Ministry of Science and Education of the Republic of Azerbaijan, Nakhchivan, AZ-7000, Azerbaijan*
[c]*Nakhchivan State University, Nakhchivan, AZ-7012, Azerbaijan*
**Corresponding Author e-mail: ruslan_rtm@yahoo.com*
Received January 10, 2025; revised March 4, 2025; accepted March 17, 2025

Photometric observations of the CH Cyg symbiotic star were conducted using the Zeiss 600 telescope at the ShAO (Shamakhy Astrophysical Observatory) between 06.07.2018 and 16.09.2018 over the course of 17 nights with the V-filter. The light curve for this star was constructed based on our observations and data from the AAVSO (American Association of Variable Star Observers) database. To analyze the nature of the variability, we performed statistical spectral Fourier analysis utilizing the Scargle method. Our findings align perfectly with those of the AAVSO. The star's light has increased during the observation period up to 2 stars size – from 8.5^m to 6.5^m. Continuous observations have shown that short-term flickering of the star occurs during the night up to 0.2-0.45 magnitude. We suppose that the cause of these flickering is the increase in the flow rate of matter from the Red Giant star to the surface of the White Dwarf in the period close to the periastron.
Keywords: *Symbiotic star; CH Cyg; Photometric variable; Flickering; Power spectrum*, *Observation; CDD photometry*
PACS: 97.80.−d; 97.80 Fk; 97.80.Gm; 97.80.hn

1. INTRODUCTION

Symbiotic stars are interacting binary systems surrounded by cover. They consist of advanced Red Giant and hot component – White Dwarf. The material source of the cloud is Red Giant which loses its substance by star wind and pulsation, the energy source is the hot White Dwarf.

CH Cyg (HD 182917) is the brightest and closest one among the symbiotic stars. The distance to this symbiotic star is about 244 parsecs according to data of Hippacros [1]. Its visual star size increased up to $V=5.5^m$ on 1982-1983 and decreased down to minimum of $V=10.5^m$ in 1996. The brightness of the start in a still condition is mainly 7^m. Photometric observation of CH Cyg for more than 130 years is available, and it was studied comprehensively [2]. For long time CH Cyg was known as a single giant star pulsating in 100 days period in a little amplitude. Previous to 1963, CH Cyg showed no variable behavior and was actually used as a M6III spectral type calibrator. Since 1963 after activation strong emission lines of blue continuum and hydrogen were seen. Since that time CH Cyg was accepted as a symbiotic star – binary of M7 cold giant and accreting White Dwarf [3]. At that time, the spectrum of CH Cyg resembled a symbiotic star. This phenomenon was observed again in 1965. Since then, there have been several such outbursts of different durations: 1967−1970, 1977−1986, 1992−1995, 1998−1999, 2011-2012 and 2017-2018.

CH Cyg is one of the rare symbiotics flashing in minute time scale [4]. Flickering disappears, blue continuum gets stronger and radiation lines are getting larger when jets are observed. Flickering reflects large spectral stochastic changes of brightness in several minutes time scale up to 0.01^m to 1^m magnitude. Flickering activity has been observed only in 10 symbiotic stars: RS Oph, T GrB, MWC 560, V2116 Oph, CH Cyg, RT Cru, o Cet, V407 Cyg, V648 Car and EF Aql.

5-20 minutes of flickering has been observed in the spectrum of the symbiotic star of CH Cyg in the optical region profiles of emission lines and in the spectrophotometric parameters [5].

Here we present photometric observations of the flickering of CH Cyg in 2018.

2. OBSERVATIONS AND RESULTS

Observations of CH Cyg star have been carried out in ZEISS-600 telescope of Shamakhy Astrophysics Observatory during 72 days between 06.07.2018 – 16.09.2018 and 17 nights. The telescope was fitted with CCD photo receiver of 4096x4096 pixel (1 pix= 9mic) size and with 17 arcmin of efficient visual area of photometer [6].

The data reduction was done using MaxIm DL following standard procedures for aperture photometry. A few comparison stars from the list of Henden and Munari have been used, bearing in mind that V2365 Cyg (SAO 31628) is an eclipsing binary [7, 8].

TYC 3551-1725-1 was selected as the comparison star, and V2365 Cyg (SAO 31628) was used as the check star. To investigate the nature of the faster variations, continuous observations with high time resolution were carried out over several nights using a single filter (V).

Table 1 presents the observation list, including the observation date, the number of images taken, the exposure duration, the total observation period, as well as the average, maximum, and minimum brightness values, along with the maximum variations observed.

Cite as: Kh.M. Mikailov, R.T. Mammadov, East Eur. J. Phys. 2, 38 (2025), https://doi.org/10.26565/2312-4334-2025-2-04

Table 1. Journal of observations.

date-obs	exposures	obs. duration (minute)	Vave	V_{min}	V_{max}	ΔV
06.07.2018	5x10s	1.16	7.579	7.591	7.568	0.023
09.07.2018	15x5s	2.51	7.488	7.507	7.466	0.041
10.07.2018	59x3s	10	7.463	7.546	7.379	0.167
11.07.2018	79x3s	9+3*	7.301	7.388	7.269	0.119
14.07.2018	10x3s	2.36	7.187	7.211	7.17	0.041
18.07.2018	60x2s,15x3s	13	7.145	7.275	7.056	0.219
19.07.2018	700x3s,30x5s	148	7.012	7.143	6.846	0.297
06.08.2018	450x1s,15x2s, 11x3s	79	6.574	6.714	6.411	0.303
07.08.2018	120x2s	20.5	6.564	6.61	6.493	0.117
16.08.2018	174x1.5s, 150x2s	37+42*	6.623	6.796	6.424	0.372
22.08.2018	50x2s, 15x3s	10	6.669	6.727	6.589	0.138
30.08.2018	60x2s	8	6.777	6.808	6.74	0.068
03.09.2018	70x2s	17	6.471	6.626	6.358	0.268
06.09.2018	20x1.5s, 130x1s, 200x1s	43+27*	6.674	6.91	6.447	0.463
07.09.2018	160x1s	24	6.889	6.961	6.828	0.133
15.09.2018	100x1s	14	7.214	7.336	7.082	0.254
16.09.2018	950x2s, 500x2s	87+79*	7.199	7.336	7.087	0.249

*- observations have been conducted in the two sequential time intervals.

Observations have been conducted continuously within several nights. The most lasting observations have been conducted in 19-07-2018 – 148 minutes, 06-08-2018 – 79 minutes and 16-09-2018 – 87 and 79 minutes. Continuity of observations in the other nights have been: 10 minutes in 10/11-07-2018 and 22-08-2018, 13-14 minutes in 18-07-2018 and 15-09-2018, 20 minutes in 07-08-2018, 37 and 42 minutes in 16-08-2018.

Light curve in V filter has been given in the figure-1 based on our observations and AAVSO (American Association of Variable Star Observers) database. As it is reflected in the figure, our results accord with the AAVSO results. CH Cyg star was active during observation period and increased its brightness from 7.56^m to 6.47^m.

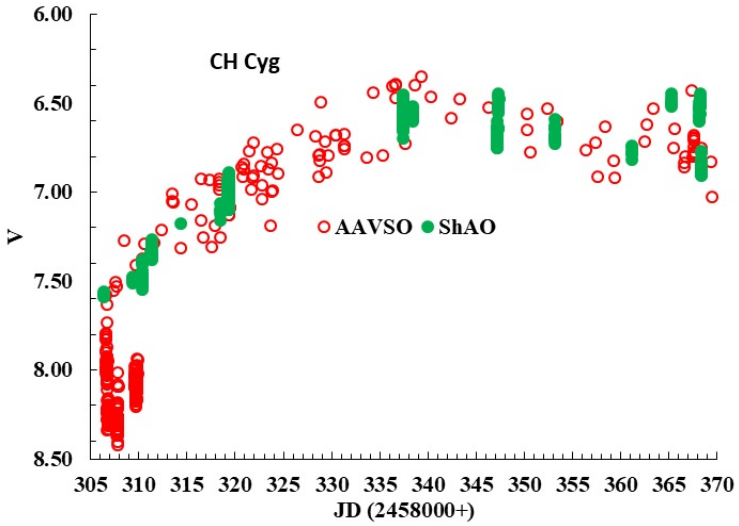

Figure.1. Comparison of the Light Curves of the CH Cyg Symbiotic Star for the period from 06-07-2018 ÷ 16-09-2018. ○-AAVSO, ●-ShAO.

3. FLICKERING

Photometric flickering of CH Cyg was identified by Wallerstein for the first time [9] and then have been comprehensively studied by various authors [10,11,12,13]. Flickering was not observed in 2010-2013, was observed again starting from 2014 [11].

Our observations also coincided to flickering time of the star. Nigh observations showed that several minutes lasting little amplitude of flickering occurs in the symbiotic star of CH Cyg. Light curves of several nights reflecting flickering in V filter of CH Cyg star are given in the figure 2. As it is reflected in the figure 2, character and amplitude of flickering was different from night to night.

Maximum change of brightness was 0.16^m for 7 minutes in 10-07-2018, 0.12^m for 5 minutes in 11-07-2018, 0.22^m for 10 minutes in 18-07-2018, 0.3^m for 35 minutes in 19-07-2018, 0.3^m for 39 minutes in 06-08-2018, 0.21^m for 17 minutes in 16-08-2018, in the first half of observation, 0.27^m for 39 minutes in the second half of observation, the amplitude of flickering during the night was 0.36^m. It was 0.14^m for 03 minutes in 22-08-2018, 0.14^m for 24 minutes in the first half of observation in 06-09-2018^m, 0.16^m for 26 minutes in the second half of the observation, amplitude of flickering was 0.45^m during the night. 0.22^m for 3 minutes in the first half of observation in 15-09-2018, 0.26^m for 8 minutes in the second half of observation, 0.14^m for 17 minutes in 16-09-2018 for the first half and maximum amplitude of flickering was 0.25^m.

Thus, changes in V brightness of CH Cyg symbiotic star with 0.1 m - 0.45 m amplitude in 1-30 minutes interval and 0.05 m - 0.06 m amplitude of changes happened in 10-30 seconds interval.

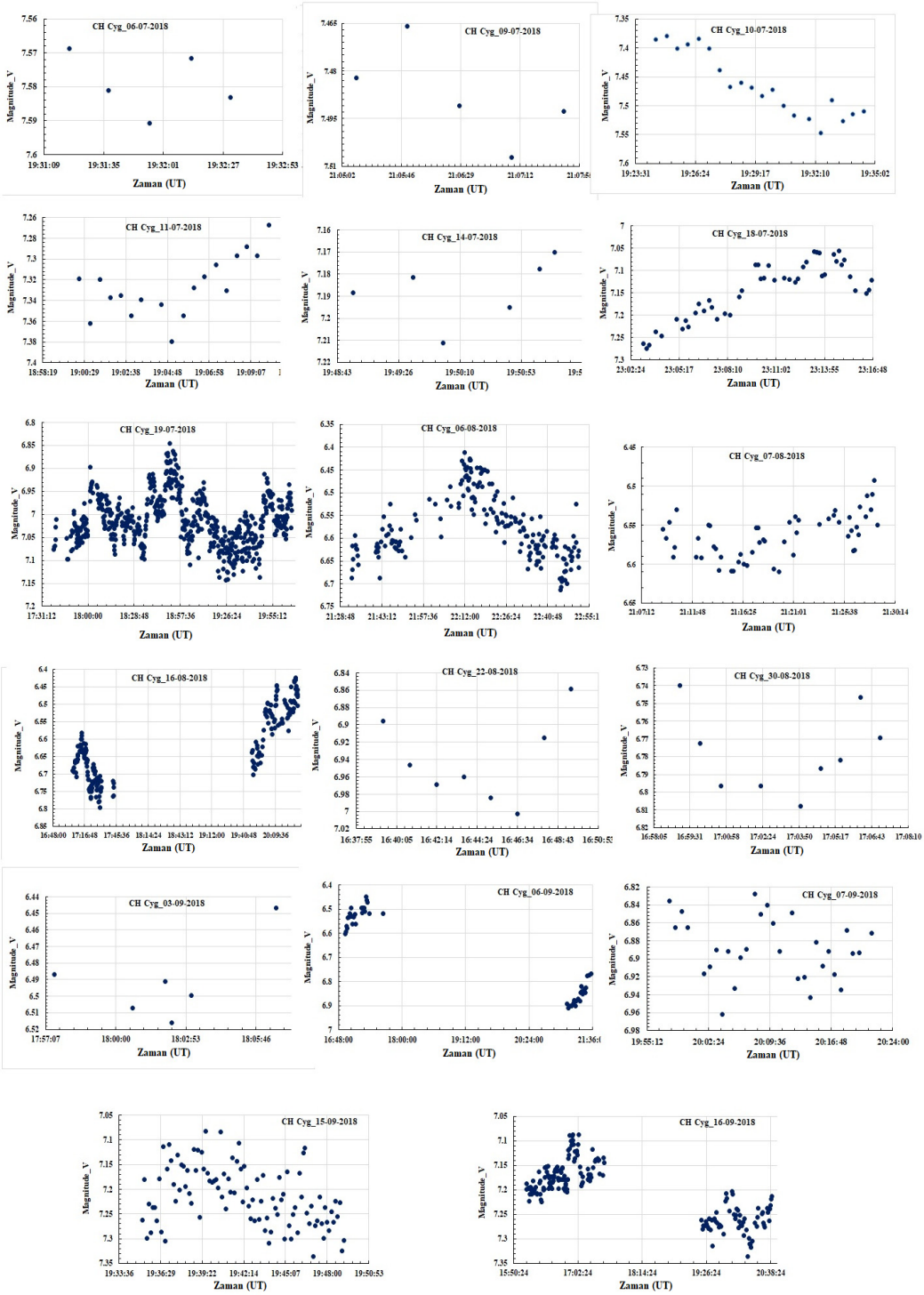

Figure 2. Flickering of CH Cyg in V bands.

4. PERIODICITY

Investigating the periodicity of flickering in the CH Cyg symbiotic star is challenging because our observations did not cover a sufficiently long time period, except for a few nights. However, as shown in Figure 2, some periodic variations were observed on certain nights. To explore the periodicity on a minute timescale, we applied spectral Fourier analysis using the Scargle method to the results of all our observations. As an example, the power spectra for the V-band on 06-08-2018, 16-08-2018, and 07-09-2018 are presented in figure 3.

In the figure 4 phase diagrams of brightness in V filter for the dates of 06-08-2018, 16-08-2018 and 07-09-2018 are given. Short time changes in brightness of CH Cyg star in V filter in dates of 06-08-2018 (79 minutes of observation) and 16-08-2018 (200 minutes) demonstrated close periodic values – 67 minutes and 65 minutes. Period of flickering was 12 minutes in 07-09-2018.

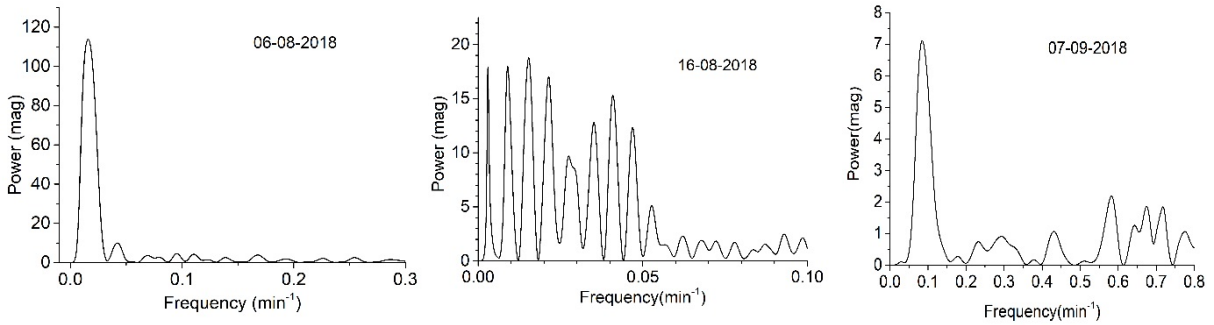

Figure 3. Power spectrum within 0-0.3, 0-0.1, 0-0.8 frequency intervals according to value of V data massive. The highest peak within the power spectrum accords with the value of frequency 0.0149, 0.0153, 0.0846 in the dates of 06-08-2018, 16-08-2018, 07-09-2018. Periods respectively are 67 minutes, 65 minutes and 12 minutes.

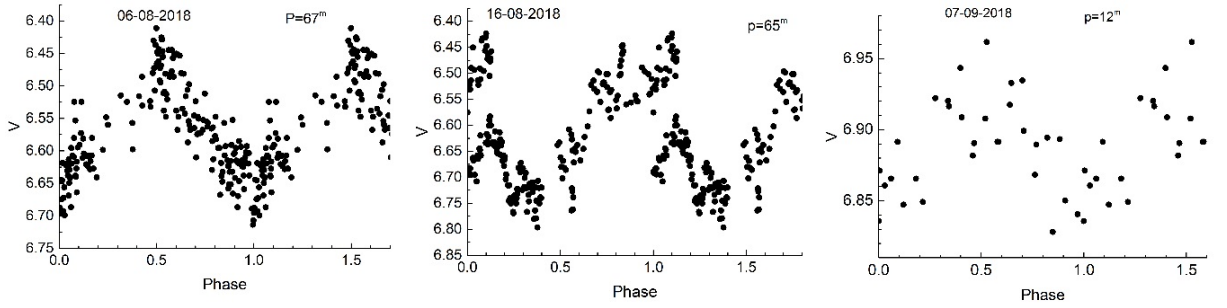

Figure 4. Phase diagrams for brightness of the start CH Cyg in V filter.

5. DISCUSSION

Red Giants are stars that have reached the necessary temperature for helium fusion in their cores. White Dwarfs, on the other hand, are stars nearing the end of their life cycle and are highly compressed. These stars are so dense that, despite having nearly the same mass as the Sun, their size is comparable to that of Earth. Due to their immense density, being 200000 times heavier than Earth, they exert a very strong gravitational pull. As a result, they can accumulate large amounts of matter from the companion cold giant, and in most symbiotic systems, an accretion disc forms around the White Dwarf.[16]. This happens due to rotation of binary system. As a result of the rotation of the binary system, the substance flowing from the Red Giant bends and falls on the White Dwarf due to its strong gravity. By causing matter to rotate, it forms a disk around the White Dwarf.

White Dwarfs have such a strong gravitational field that they can pull matter from the other star in a symbiotic system. This process is known as Roche Lobe Overflow. It occurs when a star expands to a point where its ability to retain its outer layers diminishes, causing its size to exceed the Roche limit. As a result, the excess material flows onto the binary system, forming a disc. Occasionally, this accretion leads to the formation of an ionized gas cloud around the hot component.

Source of flickering in optical region in symbiotic stars are known to be a disc [15]. Researchers consider that flickering disappears when accretion disc destroyed [11] or magnetic propeller gets activated [10]. Faster changes were observed during flickering of stars. Changes in fluxes in U filter were 10-30% within several minutes. CH Cyg is unique changing star and demonstrates complex alterations of different character in the light curve and large diapason of spectrum. Observed long lasting alterations (variating in 10 years) are caused by orbital movements or increasement of the dust cover. Several alterations of 95-100 days are related to pulsation of the giant [16]. Short term flickering activity relates to accretion disc. Increasement of activity of flickering since 2014 can be related to acceleration of processes in the disc as a result of increasement in amount of substance absorbed from the Red Giant while White Dwarf moves through periastron in CH Cyg symbiotic system.

6. CONCLUSION

The results of the analysis of observations in the V filter for the CH Cyg symbiotic star, made with the "Zeiss-600" telescope at the ShAO from 06.07.2018 to 16.09.2018 (over a period of 72 days and 17 nights), are as follows:

The star's brightness increased by about 2 magnitudes during the observation period, rising from 8.5^m to 6.5^m.

Continuous observations revealed that short-term flickerings in the star's brightness occur, ranging from 0.2 to 0.45 magnitudes. These flickering are likely caused by an increase in the rate of material flow from the Red Giant to the White Dwarf near periastron.

Periodic variations of 67, 65, and 12 minutes were observed for the fluctuations on different nights.

We sincerely thank the observers worldwide who contributed variable star observations to the **AAVSO** (American Association of Variable Star Observers) International Database, which were used in this research.

ORCID

Ruslan Mammadov, https://orcid.org/0000-0001-5879-1368

REFERENCES

[1] F. Van Leeuwen, "Hipparcos, the New Reduction of the Raw Data," Astrophysics and Space Science Library, **350**, 39-70 (2007). https://doi.org/10.1007/978-1-4020-6342-8_2

[2] M. Mikolajewski, J. Mikolajewska, and T.N. Khudyakova, "A long-period symbiotic binary CH Cygni. I. A hundred years' history of variability," Astronomy and Astrophysics, **235**, 219-233 (1990). https://articles.adsabs.harvard.edu/pdf/1990A%26A...235..219M

[3] Kh. M. Mikailov, A.J. Orujova, R.T. Mammadov, I.A. Alakbarov, and O.V. Khalilov, "Analysis of spectral and photometric observations of the CH Cyg symbiotic star in 2018," Astronomıcal Journal of Azerbaijan, **16**(1) 4-21 (2021). https://aaj.shao.az/vol16_n1/AAJ_2021_V16_N1.pdf

[4] D. Dobrzycka, S.J. Kenyon, and A.E. Milone, "Rapid Light Variations in Symbiotic Binary Stars," Astronomical Journal, **111**(1), 414-423 (1996). https://articles.adsabs.harvard.edu/pdf/1996AJ....111..414D

[5] Kh.M. Mikailov, R.T. Mammadov, B.N. Rustamov, and A.B. Rustamova, "Spectral Variability of the Symbiotic Star CH Cyg". Proceedings of the Pakistan Academy of Sciences: Part A: PS-671, **60**(1), 9-13 (2023). https://doi.org/10.53560/PPASA(60-1)671

[6] B.I Abdullayev, I.A. Alekberov, N.I. Gulmaliyev, Kh.M. Mikailov, *et al*., "A new photometer – polarımeter coupled wıth ccd," Azerbaijani Astronomical Journal, **8**(4), 39-49 (2012). https://aaj.shao.az/vol7_n4/AAJ_2012_V7_N4.pdf

[7] A. Henden, and U. Munari, "UBV(RI)C photometric sequences for symbiotic stars III," Astronomy and Astrophysics, **458**(1), 339-340 (2006). https://doi.org/10.1051/0004-6361:20065662

[8] J.L. Sokoloski, and R.P.S. Stone, "Discovery of Eclipsing Binary Nature of SAO 31628 = BD+49d2997, Common Comparison Star for CH Cygni," Information Bulletin on Variable Stars, **4983**, 1-3 (2000). https://adsabs.harvard.edu/full/2000IBVS.4983....1S

[9] G. Wallerstein, "Photoelectric observations of rapid variations of CH Cygni," Annals of Harvard College Observatory, **88**, 111-112 (1968). https://adsabs.harvard.edu/full/1968Obs....88..111W

[10] M. Mikolajewski, J. Mikolajewska, T. Tomov, *et al*., "Symbiotic binaries. III - Flickering variability of CH Cygni: Magnetic rotator model," Acta Astronomica, **40,** 129-157 (1990). https://adsabs.harvard.edu/full/1990AcA....40..129M

[11] J.L. Sokoloski, and S.J. Kenyon, "CH Cygni. II. Optical Flickering from an Unstable Disk," The Astrophysical Journal, **584**, 1027-1034 (2003). https://doi.org/10.1086/345902

[12] T.H. Dingus, "Flickering Analysis of CH Cygni Using Kepler Data," Flickering Analysis•Spring 2016, 38, (2016). https://dc.etsu.edu/cgi/viewcontent.cgi?article=1380&context=honors

[13] K.A. Stoyanov, J. Martí, R. Zamanov, *et al*., "Optical flickering of the symbiotic star CH Cyg," Bulgarian Astronomical Journal, **28**, 42-47 (2018). https://arxiv.org/pdf/1711.01749

[14] J.L. Sokoloski, "Symbiotic Stars as Laboratories for the Study of Accretion and Jets: A Call for Optical Monitoring," Journal of the American Association of Variable Star Observers (JAAVSO), **31**(2), 89-102 (2003). https://articles.adsabs.harvard.edu/pdf/2003JAVSO..31...89S

[15] J.L. Sokoloski, and S.J. Kenyon, "CH Cygni. I. Observational Evidence for a Disk-Jet Connection," The Astrophysical Journal, **584**(2), 1021-1026 (2003). https://doi.org/10.1086/345901

[16] Kh.M. Mikailov, and R.T. Mammadov, "95-day variability in the light curve of the symbiotic star CH Cyg," in: *Proceedings of the XXI International Multidisciplinary Conference "Prospects and Key Tendencies of Science in Contemporary World*," (Bubok Publishing S.L., Madrid, 2022), pp. 67-71. https://www.internauka.org/conf/spain/21/343943

ФОТОМЕТРИЧНЕ МЕРЕХТІННЯ CH CYG У 2018 РОЦІ

Х.М. Мікайлов[a], Р.Т. Мамедов[b,c]

[a]Бакинський Державний Університет, Баку, AZ-1148, Азербайджан

[b]Батабатська Астрофізична Обсерваторія Міністерства Науки і Освіти Азербайджанської Республіки, Нахічевань, AZ-7000, Азербайджан

[c]Нахічеванський Державний Університет, Нахічевань, AZ-7012, Азербайджан

Фотометричні спостереження симбіотичної зірки CH Cyg проводилися на телескопі Zeiss 600 в ШАО (Шамахинська Астрофізична Обсерваторія) в інтервалі 06.07.2018-16.09.2018 протягом 17 ночей з використанням V-фільтра. Криву блиску цієї зірки було встановлено на основі наших спостережень і баз даних AAVSO. Для вивчення характеру зміни ми застосували статистичний спектральний аналіз Фур'є за методом Скаргла. Наші результати повністю відповідають результатам AAVSO. Світло зірки збільшилося за період спостережень до розміру 2 зірки – з 8,5 до 6,5. Безперервні спостереження показали, що вночі відбуваються короткочасні мерехтіння зірки до 0,2-0,45 зоряної величини. Ми припускаємо, що причиною цих мерехтінь є збільшення швидкості потоку речовини від зірки червоного гіганта до поверхні білого карлика в період, близький до периастрона.

Ключові слова: *симбіотична зірка; CH Cyg; фотометрична змінна; мерехтіння; спектр потужності, спостереження; CDD фотометрія*

EAST EUROPEAN JOURNAL OF PHYSICS. **2.** 43-48 (2025)
DOI:10.26565/2312-4334-2025-2-05 ISSN 2312-4334

A NEW IBM-1 HAMILTONIAN PARAMETERIZATION BASED ON DYNAMICAL SYMMETRY FOR EVEN-EVEN Se^{74-78}, $Ru^{104-106}$ AND $Mo^{106-108}$

Berun N. Ghafoor
Department of Physics, College of Education, University of Sulaimani, Iraq
**Corresponding Author e-mail: berun.ghafoor@univsul.edu.iq*
Received February 26, 2024; revised March 18, 2025; accepted March 20, 2025

The present study investigates the dynamical symmetries of even-even Se^{74-78}, $Ru^{104-106}$ and $Mo^{106-108}$ isotopes within the framework of the Interacting Boson Model-1 (IBM-1). The analysis explores the three fundamental symmetry groups: SU(5) (vibrational), O(6) (gamma-soft), and SU(3) (rotational). Energy levels were calculated using newly optimized Hamiltonian parameterizations based on the U(6) unitary group structure in six dimensions, and the results were compared with experimental data, demonstrating excellent agreement. A key finding of this study is that for each nucleus, the predominant Hamiltonian parameter can be selectively adjusted to achieve an optimal theoretical-experimental match, particularly in relation to the $\frac{E4_1^+}{E2_1^+}$ energy ratio. This approach provides a systematic and efficient method for refining Hamiltonian parameterization, offering a standardized technique to enhance the accuracy of nuclear structure studies. The findings contribute to a deeper understanding of nuclear collective motion and may serve as a foundation for further advancements in theoretical nuclear physics.
Keywords: *IBM-1; Dynamical symmetry, Hamiltonian parameterization; Energy levels; Se-isotopes; Ru-isotopes; Mo-isotopes*
PACS: 21.60.Fw, 21.10.Re, 23.20.Lv, 27.60.+j, 27.50.+e

INTRODUCTION

The Interacting Boson Model (IBM-1), developed by Arima and Iachello, revolutionizes the study of nuclear structure by offering a simplified yet powerful framework rooted in group theory [1]. In the six-dimensional space governed by the unitary group U(6), the IBM-1 model explains dynamical symmetry through its fundamental subgroups: SU(5) for vibrational nuclei, SU(3) for rotational nuclei, and O(6) for gamma-soft nuclei [2].

Several studies have utilized the IBM-1 model to investigate the nuclear structure of various isotopes. S.A. Abdulsahib et al. employed IBM-1 for even-even Se^{76-82} isotopes, considering them as O(6) shapes. Their study focused on the impact of the O(6) dynamical symmetry group chain on the Hamiltonian parameterization, particularly on (a_0, a_1, and a_3) [3]. Similarly, Yaseen, Mustafa T., et al. analyzed the Se^{72-80} isotopes, primarily highlighting the dominance of U(5) characteristics. They also noted a minor influence of the a_2 parameter, beginning from Se^{74} to Se^{80}. Their energy ratios indicated that Se^{72} is the closest to a typical vibrational limit, while the Se^{74-80} isotopes exhibit a gradual transition toward the rotational region along the U(5)-SU(3) limit [4].

Beyond selenium isotopes, Sharrad, Fadhil I. et al. investigated $Ru^{96,98}$ isotopes, demonstrating their U(5) dynamical symmetry. They highlighted the significant influence of the ϵ parameter in the IBM-1 Hamiltonian. Furthermore, the even-even $Ru^{108-112}$ isotopes were classified as transitional nuclei, positioned between the U(5) spherical vibrator and SO(6) γ-unstable rotor symmetries [6]. More broadly, several studies focus on refining the IBM-1 Hamiltonian to enhance its applicability to these isotopes.

In addition, Berun et al. have carried out significant research on the nuclear structure of Mo isotopes, including $^{94}_{42}Mo$ [7], $^{96-98}_{42}Mo$ [8], and $^{100}_{42}Mo$ [9], using the IBM-1 model. Their studies emphasized the vibrational nature of these nuclei under SU(5) symmetry, highlighting the crucial role of four Hamiltonian parameters (ε, a_1, a_3, and a_4) in determining their energy spectra. More recently, Ghafoor and Shwan (2024) explored the nuclear structure of $^{102}_{42}Mo$ within the IBM-1 framework, analyzing the impact of the Hamiltonian parameters a_0, a_1, and a_3. Their findings established a strong correlation between these parameters and the O(6) dynamical symmetry group, which characterizes gamma-soft nuclei [10].

The objective of the current study is to systematically investigate the Hamiltonian parameters for constructing the energy levels of even-even Se^{74-78}, $Ru^{104-106}$, and $Mo^{106-108}$ isotopes. A particular focus is placed on the $\frac{E4_1^+}{E2_1^+}$ energy ratio, which serves as a key indicator of nuclear dynamical symmetry. Furthermore, this study examines the specific dynamical symmetries exhibited by these nuclei within the IBM-1 framework, refining the parameterization approach for future nuclear structure studies.

THEORETICAL BACKGROUND

The Hamiltonian, which establishes connections between the basis states, is formulated using the principles of second quantization. As a result, it exclusively consists of combinations of the operators s, $s^\dagger$, d, and $d^\dagger$. Such a Hamiltonian operator ($\hat{H}$) comprises both one-body and two-body operators [1].

Cite as: B.N. Ghafoor, East Eur. J. Phys. 2, 43 (2025), https://doi.org/10.26565/2312-4334-2025-2-05

$$\widehat{H} = \varepsilon_s\, s^{\dagger}\tilde{s} + \varepsilon_d \sum_m d^{\dagger}\tilde{d} + V. \quad (1)$$

The parameters ε_s and ε_d represent the single-boson energies for the s- and d −bosons, respectively, and m represents the magnetic quantum number of the dd-boson states, which range from $m = -2, -1, 0, 1, 2$ corresponding to the angular momentum quantum number L = 2. while V denotes the boson-boson interaction potential. The operators $s^{\dagger}(\tilde{s})$ function as creation and annihilation operators for the s-boson state, whereas $d^{\dagger}(\tilde{d})$ serve as creation and annihilation operators for the d-boson state. The most widely utilized formulation of the IBM-1 Hamiltonian [11], which also provides the clearest insight into how each term influences the resulting nuclear structure, is known as the multipole expansion. In this approach, different boson-boson interactions are categorized systematically, allowing the Hamiltonian to be expressed in a structured form.

$$\widehat{H} = \varepsilon\,(n_d) + a_0\,(\hat{P}.\,\hat{P}) + a_1(\hat{L}.\,\hat{L}) + a_2(\hat{Q}.\,\hat{Q}) + a_3\,(\hat{T}_3.\,\hat{T}_3) + a_4\,(\hat{T}_4.\,\hat{T}_4). \quad (2)$$

Here ε, a_0, a_1, a_2, a_3, and $a_4$represent the model parameters, while $\hat{P}.\,\hat{P}$, $\hat{L}.\,\hat{L}$, $\hat{Q}.\,\hat{Q}$, $\hat{T}_3.\,\hat{T}_3$, and $\hat{T}_4.\,\hat{T}_4$ correspond to the pairing, angular momentum, quadrupole, octupole, and hexadecapole operators, respectively. Additionally, n_d denotes the d-boson number operator.

RESULTS AND DISCUSSION

The first step in our calculations is to determine the total number of bosons. In the original IBM-1 model, there is no distinction between protons and neutrons [12], and the valence number is always counted relative to the nearest closed shells. To calculate the total boson count, we first determine the difference in proton or neutron numbers relative to the nearest closed shell, divide this value by two, and then sum the resulting proton and neutron bosons. Following this method, the total number of bosons for even-even isotopes is as follows: Se^{74-78} has 8, 7, and 6 bosons, respectively; $Mo^{106-108}$ has 11 and 12 bosons, respectively; and $Ru^{104-106}$ has 8 and 9 bosons, respectively. In the present study the $\frac{E4_1^+}{E2_1^+}$ ratio was used in order to determine the dynamical symmetry region for isotopes. Table 1 provides the IBM-1 Hamiltonian parameters essential for calculating the low-lying positive parity energy levels of presented nuclei. In the Interacting Boson Model-1 (IBM-1), the Hamiltonian plays a crucial role in describing nuclear structure by incorporating different interaction terms that govern the behavior of bosons. To ensure accurate results, the IBM-1 Hamiltonian is constructed and solved within the framework of dynamical symmetry regions. This approach allows for a systematic understanding of nuclear shape transitions, whether vibrational (U(5)), rotational (SU(3)), or gamma-soft (O(6)). The calculations are performed using the PHINT computer program [13], which efficiently handles the matrix diagonalization and provides the energy eigenvalues necessary for analyzing nuclear excitations.

Table 1. IBM-1 Hamiltonian parameterization for description of presented nuclei

Nucleus	Hamiltonian Parameters (MeV)						χ	$SO(6)$
	EPS	*PAIR*	*ELL*	*QQ*	*OCT*	*HEX*		
Se^{74}	0.2700	0.0070	0.0188	0.0000	0.0606	0.0850	0.0000	1.0000
Se^{76}	0.2670	0.0060	0.0188	0.0000	0.0506	0.0850	0.0000	1.0000
Se^{78}	0.1600	0.1160	0.0108	0.0000	0.3406	0.0550	0.0000	1.0000
Ru^{104}	0.5000	0.0500	0.0105	-0.0080	0.0000	0.0000	-1.3200	1.0000
Ru^{106}	0.4700	0.0500	0.0105	-0.0070	0.0000	0.0000	-1.3200	1.0000
Mo^{106}	0.4800	0.0500	0.0105	-0.0080	0.0000	0.0000	-1.3200	1.0000
Mo^{108}	0.4800	0.0400	0.0120	-0.0080	0.0000	0.0000	-1.3200	1.0000

Where the Parameters are related to its coefficients such $\varepsilon = EPS$, $a_0 = 2 * PAIR$, $a_1 = \frac{ELL}{2}$, $a_2 = \frac{QQ}{2}$, $a_3 = 5 * OCT$, $a_4 = 5 * HEX$ [14] The low-lying positive parity energy levels of Se isotopes have been investigated, and the theoretical results show strong agreement with experimental data [15-17], as illustrated in Figure 1.

The Hamiltonian parameters ε, a_1 and a_4 play a crucial role in accurately reproducing the energy levels for Se^{74} due to its SU(5) dynamical symmetry. However, in the case of Se^{76}, the sensitivity shifts towards a_0, where even a slight variation in a_0 yields the best agreement between theoretical and experimental values. This indicates that Se^{76} exhibits characteristics intermediate between SU(5) and O(6) dynamical symmetries. On the other hand, Se^{78} predominantly exhibits O(6)-like gamma-unstable behavior, with a_0 , a_1 and a_3 emerging as the most influential parameters in determining its energy structure. Additional energy levels that are not explicitly shown in Figure 1 have also been investigated, demonstrating strong agreement with experimental data. For Se^{74}, the calculated energy values for 2_2^+, 3_1^+, 6_1^+, 6_2^+, and 4_4^+ are 1.268 MeV, 1.0904 MeV, 2.294 MeV, 3.096 MeV, and 3.050 MeV, respectively. These results closely match the corresponding experimental values [15] of 1.269 MeV, 1.884 MeV, 2.232 MeV, 2.986 MeV, and 3.078 MeV. Similarly, for Se^{76}, the calculated energy levels for 2_2^+ and 4_3^+ are 1.216 MeV and 2.805 MeV, which align well with the experimental values [16] of 1.230 MeV and 2.840 MeV. For Se^{78}, the calculated energy values for 2_2^+, 4_2^+, 6_1^+, and 6_2^+, are 1.308 MeV, 2.191 MeV, 2.546 MeV, and 3.140 MeV, respectively. These values show excellent agreement with the experimental data [17], which are 1.378 MeV, 2.207 MeV, 2.464 MeV, and 3.123 MeV, respectively.

The energy levels of Ru^{104} and Ru^{106} are depicted in Figure 2 and compared with experimental data [18, 19], demonstrating excellent agreement.

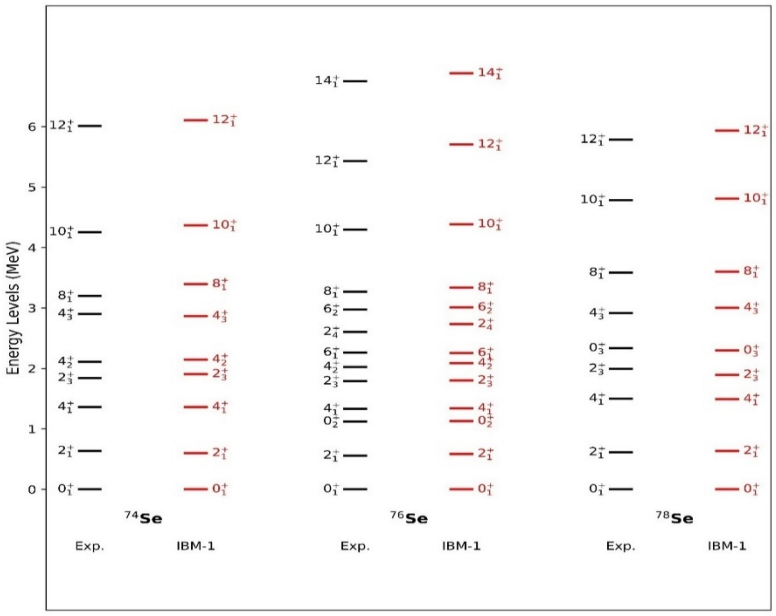

Figure 1. IBM-1 calculated energy level schemes for Se isotopes compared with experimental data [15-17].

The O(6) dynamical symmetry is predominant in Ru^{104}, making a_0 a highly sensitive parameter alongside a_3,. However, variations in the ε parameter can systematically alter the energy levels due to the vibrational nature of Ru^{104}, which aligns closely with SU(5) symmetry. In contrast, Ru^{104} also exhibits gamma-soft behavior, with O(6) symmetry remaining dominant. However, it slightly deviates from the O(6) group chain, displaying characteristics that gradually shift toward rotational motion. While maintaining the calibration of a_0 , a_1 and a_3, minor adjustments to the a_2, parameter is necessary. Additionally, in Figure 2, several energy levels have been analyzed using the optimized Hamiltonian parameterization. For Ru^{104}, the calculated values for 2_2^+, 0_2^+, 0_3^+, 4_2^+, 4_3^+, and 3_2^+ are 0.880 MeV, 0.899 MeV, 1.288 MeV, 1.451 MeV, 1.995 MeV, and 2.401 MeV, respectively, showing strong agreement with the experimental values [18] of 0.893 MeV, 0.988 MeV, 1.335 MeV, 1.502 MeV, 2.080 MeV, and 2.330 MeV, respectively. Similarly, for Ru^{106}, the calculated energy levels for 2_2^+, $0_2^+$and 4_2^+ are 0.702 MeV, 0.832 MeV, and 1.276 MeV, which align well with the experimental data [19] of 0.792 MeV, 0.991 MeV, and 1.306 MeV, respectively.

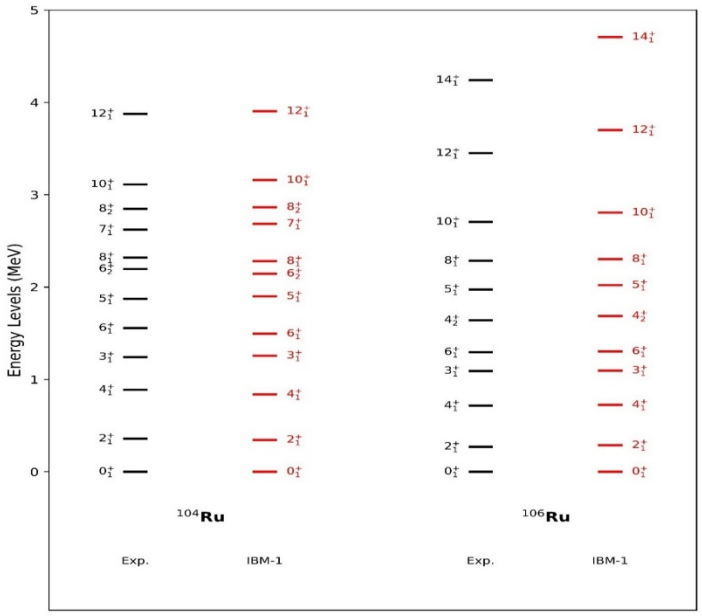

Figure 2. IBM-1 calculated energy level schemes for Ru isotopes compared with experimental data [18, 19].

The energy values of Mo^{106} and Mo^{108} are presented in Figure 3, demonstrating excellent agreement with experimental data [19, 20]. For Mo^{106}, the Hamiltonian parameters a_1 and a_2 exhibit the highest sensitivity, as the

nucleus is close to the SU(3) dynamical symmetry. Additionally, the parameters a_0 and a_3 show minor sensitivity, indicating the influence of O(6) dynamical symmetry. Consequently, $Mo^{106}$is positioned within the O(6)-SU(3) dynamical symmetry limit. On the other hand, Mo^{108} is highly sensitive to a_1 and a_2, confirming its strong proximity to SU(3) dynamical symmetry.

Furthermore, additional energy levels not listed in Figure 3 have been investigated. For Mo^{106}, the 4_2^+, 6_2^+, and the double gamma band state 7_1^+ are calculated as 1.105 MeV, 1.606 MeV, and 2.127 MeV, respectively, showing excellent agreement with the experimental values [19] of 1.068 MeV, 1.563 MeV, and 2.127 MeV. Similarly, for Mo^{108}, the 2_2^+, 4_2^+, and the two-phonon vibrational band state 9_1^+ are calculated as 0.644 MeV, 1.056 MeV, and 2.908 MeV, respectively, aligning well with the experimental data [20] of 0.586 MeV, 0.978 MeV, and 2.883 MeV.

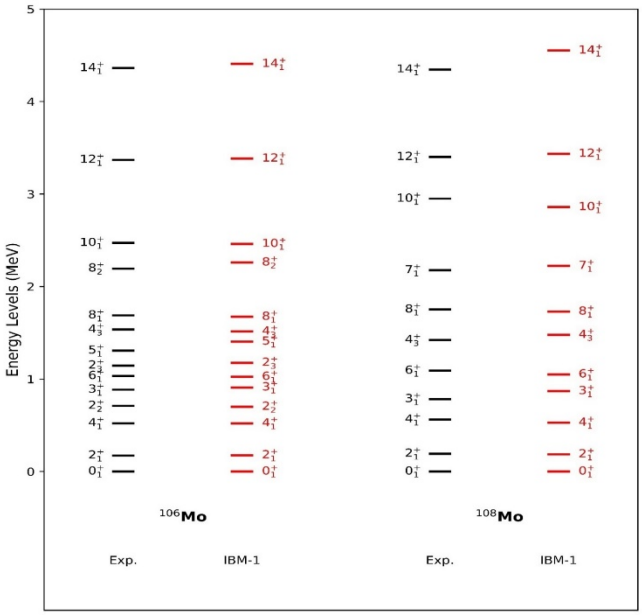

Figure 3. IBM-1 calculated energy level schemes for Mo isotopes compared with experimental data [19, 20].

The energy ratio $\frac{E4_1^+}{E2_1^+}$ plays a crucial role in diagnosing dynamical symmetry behavior. As previously mentioned, this ratio serves as a key indicator of nuclear structure: it is 2.0 for SU(5)-like vibrational nuclei, 2.5 for O(6) gamma-soft nuclei, and 3.33 for SU(3) rotational nuclei [21-24]. The calculated $\frac{E4_1^+}{E2_1^+}$ values for the investigated nuclei are presented in Figure 4. The figure reveals that these nuclei predominantly align with the SU(5) symmetry, deviating from the O(6) limit and gradually approaching the SU(3) region. Furthermore, the energy ratio $\frac{E4_1^+}{E2_1^+}$ provides insights into the evolution of Hamiltonian parameters, highlighting which interactions dominate within each symmetry group.

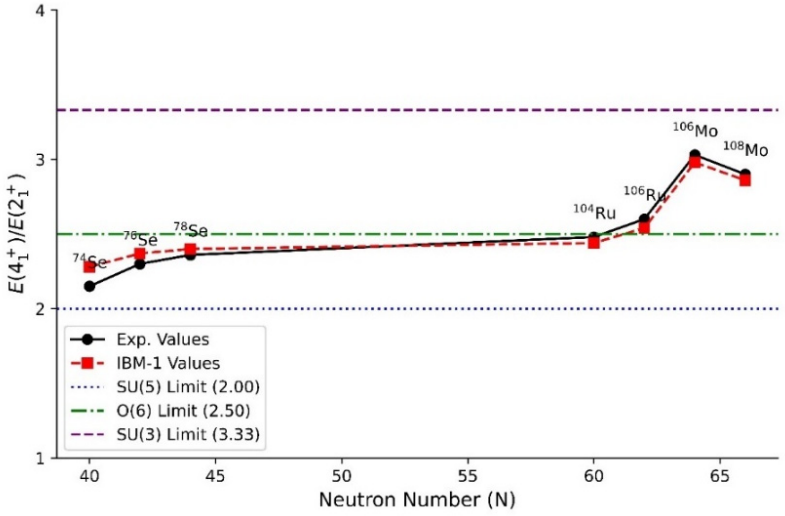

Figure 4. IBM-1 calculated value of $\frac{E4_1^+}{E2_1^+}$ compared with experimental data [20-25].

The energy ratio $\frac{E4_1^+}{E2_1^+}$ is crucial because it directly measures the collective motion inside the nucleus, differentiating between vibrational, gamma-soft, and rotational motions. Furthermore, it acts as a standard for verifying theoretical nuclear models, assisting in parameter refinement and improving the ability to predict of nuclear structure predictions.

CONCLUSION

This study systematically investigated the energy levels of even-even Se^{74-78}, $Mo^{106-108}$, and $Ru^{104-106}$ isotopes across the ground state, beta, and gamma bands using a specifically optimized IBM-1 Hamiltonian parameterization. Based on group theoretical analysis, the examined nuclei were categorized into three primary dynamical symmetry groups: SU(5) (vibrational), O(6) (gamma-soft), and SU(3) (rotational). The findings reaffirm that for SU(5) vibrational nuclei, the Hamiltonian parameters ε, a_1, a_3 and a_4 which correspond to the d-boson number, angular momentum, octupole, and hexadecapolar operators, respectively—are the most influential in accurately reproducing the nuclear energy spectra. In contrast, for O(6) gamma-soft nuclei, the dominant parameters are a_0 , a_1 and a_3, which are associated with pairing, angular momentum, and octupole interactions, respectively. Meanwhile, in the SU(3) rotational regime, the a_1 and a_2 parameters, linked to angular momentum and quadrupole operators, play the most significant role in Hamiltonian parameterization. This study highlights that ε (d-boson number operator) is the most sensitive parameter for vibrational nuclei, a_0 (pairing operator) is the key sensitivity factor for gamma-soft nuclei, and a_1 (angular momentum operator) is the dominant parameter for rotational nuclei. These insights contribute to a deeper understanding of nuclear structure and provide a refined approach for optimizing IBM-1 Hamiltonian parameterization in future nuclear physics research.

ORCID

Berun N. Ghafoor, https://orcid.org/0000-0003-0450-3919

REFERENCES

[1] A. Arima, and F. Iachello, "Interacting boson model of collective states I. The vibrational limit," Annals of Physics, **281**(1-2), 2-64 (2000). https://doi.org/10.1006/aphy.2000.6007
[2] P. Cejnar, and J. Jolie, "Dynamical-symmetry content of transitional IBM-1 hamiltonians," Physics Letters B, **420**(3-4) 241-247 (1998). https://doi.org/10.1016/S0370-2693(97)01533-5
[3] S.A. Abdulsahib, *et al*., "Explanation of the nuclear structure of even–even $^{76-82}$Se nuclei," International Journal of Modern Physics E, **32**(11), 2350055 (2023). https://doi.org/10.1142/S0218301323500556
[4] Heiyam Najy Hady, Mohsin Kadhim Muttalb, "Nuclear structure features in $^{72-80}$Se isotopes," Journal of Physics: Conference Series, **1664**, (2020). https://doi.org/10.1088/1742-6596/1664/1/012015
[5] F.I. Sharrad, *et al*., "U(5) symmetry of even ^{96,98}Ru isotopes under the framework of interacting boson model (IBM-1)," Brazilian Journal of Physics, **45**, 340-346 (2015). https://doi.org/10.1007/s13538-015-0302-6
[6] I. Stefanescu, *et al*., "IBM-1 description of the fission products ^{108,110,112}Ru," Nuclear Physics A, **789**(1-4), 125-141 (2007). https://doi.org/10.1016/j.nuclphysa.2007.03.007
[7] B.N. Ghafoor, F.H. Ali, and D.B. Ahmed, "Dynamical Symmetry and B (E2) Transitions of $^{94}_{42}$Mo by Utilizing (IBM-1)." Journal of University of Babylon for Pure and Applied Sciences, **32**(2), 24-34 (2024). https://doi.org/10.29196/jubpas.v32i2.5264
[8] B.N. Ghafoor, "A Study of Nuclear Structure of Mo^{96,98} by Using Interacting Boson Model-1," Tikrit Journal of Pure Science, **28**(6), 58-65 (2023). https://doi.org/10.25130/tjps.v28i6.1327
[9] B.N. Ghafoor, and Y.H. Shawn, "Study of Nuclear Structure of nucleus $^{100}_{42}$Mo Using Interacting Boson Model-1," Journal of University of Babylon for Pure and Applied Sciences, **31**(2), 176-182 (2023). https://doi.org/10.29196/jubpas.v31i2.4672
[10] B.N. Ghafoor, and Y.H. Shawn, "Dynamical symmetry of by utilizing (IBM-1)," Tikrit Journal of Pure Science, **29**, 2 (2024). https://doi.org/10.25130/tjps.v29i2.1550
[11] F. Iachello, and A. Arima, *The interacting boson model*, (Cambridge university press, 2006).
[12] A. Arima, and F. Iachello, "Interacting boson model of collective nuclear states II. The rotational limit," Annals of Physics, **111**(1), 201-238 (1978). https://doi.org/10.1016/0003-4916(78)90228-2
[13] O. Scholten, *Computer code PHINT, KVI*, (Groningen, Holland, 1980).
[14] R.F. Casten, and D.D. Warner, "The interacting boson approximation," Reviews of Modern Physics, **60**(2), 389 (1988). https://doi.org/10.1103/RevModPhys.60.389
[15] Nucl. Data Sheets, **107**, 1923 (2006). https://doi.org/10.1016/j.nds.2006.05.006
[16] Nucl. Data Sheets, **194**, 3 (2024). https://doi.org/10.1016/j.nds.2024.02.002
[17] Nucl. Data Sheets, **110**, 1917 (2009). https://doi.org/10.1016/j.nds.2009.08.001
[18] Nucl. Data Sheets, **108**,2035 (2007). https://doi.org/10.1016/j.nds.2007.09.001
[19] Nucl. Data Sheets, **109**, 943 (2008). https://doi.org/10.1016/j.nds.2008.03.002
[20] Nucl. Data Sheets, **91**, 135 (2000). https://doi.org/10.1006/ndsh.2000.0017
[21] A.M. Khalaf, *et al*., "Vibrational, rotational, and triaxiality features in extended O(6) dynamical symmetry of IBM using three-body interactions," Nuclear Science and Techniques, **31**(5), 47 (2020). https://doi.org/10.1007/s41365-020-00757-y
[22] H.N. Hady, and M.K. Muttal, "Investigation of Mixed Symmetry States in 170-178Yb isotopes," Journal of Physics: Conference Series, **1591**(1), (2020). https://doi.org/10.1088/1742-6596/1591/1/012016
[23] S. Lalkovski, and P. Van Isacker, "IBM-1 calculations towards the neutron-rich nucleus," Phys. Rev. C, **79**, 044307 (2009). https://doi.org/10.1103/PhysRevC.79.044307
[24] I. Hossain, *et al*., "Study on ground state energy band of even $^{114-124}$Cd isotopes under the framework of interacting boson model (IBM-1)," International Journal of Modern Physics E, **21**(08), 1250072 (2012). https://doi.org/10.1142/S0218301312500723

НОВА ГАМІЛЬТОНОВА ПАРАМЕТРИЗАЦІЯ IBM-1 НА ОСНОВІ ДИНАМІЧНОЇ СИМЕТРІЇ ДЛЯ ПАРНИХ-ПАРНИХ Se^{74-78}, $Ru^{104-106}$ ТА $Mo^{106-108}$

Берун Н. Гафур

Факультет фізики, Педагогічний коледж, Університет Сулеймані

У цьому дослідженні досліджуються динамічні симетрії парно-парних ізотопів Se^{74-78}, $Ru^{104-106}$ і $Mo^{106-108}$ у рамках моделі взаємодіючого бозона-1 (IBM-1). Аналіз досліджує три основні групи симетрії: SU(5) (вібраційна), O(6) (гамма-м'яка) і SU(3) (обертальна). Рівні енергії були розраховані з використанням нещодавно оптимізованих гамільтонівських параметризацій, заснованих на структурі унітарної групи U(6) у шести вимірах, і результати порівнювалися з експериментальними даними, демонструючи чудову узгодженість. Ключовим висновком цього дослідження є те, що для кожного ядра переважаючий параметр Гамільтона можна вибірково регулювати для досягнення оптимального теоретико-експериментального збігу, зокрема щодо $\frac{E4_1^+}{E2_1^+}$ співвідношення енергії. Цей підхід забезпечує систематичний та ефективний метод уточнення гамільтонівської параметризації, пропонуючи стандартизовану техніку для підвищення точності досліджень ядерної структури. Отримані результати сприяють глибшому розумінню колективного ядерного руху і можуть стати основою для подальшого прогресу в теоретичній ядерній фізиці.

Ключові слова: *IBM-1; динамічна симетрія, гамільтонова параметризація; рівні енергії; Se-ізотопи; Ru-ізотопи; Mo-ізотопи*

EAST EUROPEAN JOURNAL OF PHYSICS. **2.** 49-54 (2025)
DOI:10.26565/2312-4334-2025-2-06 ISSN 2312-4334

EXAMINATION OF (t, ^{3}He) CHARGE EXCHANGE REACTIONS: INCORPORATING KNOCK-ON EXCHANGE AND TENSOR FORCE TERMS EFFECTS

Ankita*, Pardeep Singh**
Department of Physics, Deenbandhu Chhotu Ram University of Science and Technology, Murthal, Sonipat 131039, Haryana, India
**Corresponding Author e-mail: *ankumehra531@gmail.com; **pardeep.phy@dcrustm.org*
Received February 4, 2025; revised March 16, 2025; accepted March 20, 2025

The present study employs DWIA (Distorted Wave Impulse Approximation) framework, allows to investigate the influence of knock-on exchange effects together with tensor force contributions while examining the charge exchange reactions. Here, the differential cross-section and unit cross-section for (t, ^{3}He) charge-exchange reactions on ^{12}C, ^{13}C, ^{26}Mg and ^{58}Ni targets have been computed. The obtained results demonstrate that consideration of knock-on exchange terms substantially decreases the estimated cross-section. Furthermore, the tensor forces contribution introduces an additional layer of complexity to the analysis of charge exchange reactions. Depending on the target nucleus, the tensor forces contribution produces either constructive or destructive interference effects, which leads to either increment or decrement in cross-section magnitude based on the target nucleus. The predicted unit cross-sections agree with corresponding experimental data but show specific deviations because of tensor interactions which are most pronounced in ^{58}Ni.
Keywords: *Gamow-Teller transitions; Charge Exchange Reaction; Tensor forces; Distorted Wave Impulse Approximation; Angular Distribution; Unit cross-section*
PACS: 25.55.-e, 25.45.Kk, 25.70.Kk, 25.40.Kv

INTRODUCTION

Spin-isospin excitations within nuclei at intermediate energies have been extensively studied through hadronic probe, involving (p, n) and (^{3}He, t) charge-exchange (CE) reactions along with their inverse reactions, (n, p) and (t, ^{3}He), during the past several decades [1]-[7]. Particularly, these reactions facilitate the exchange of nucleons (protons or neutrons) between interacting nuclei such as (t, ^{3}He) reactions and same process followed by β^+- decay shown below in Figure 1, thereby inducing isospin transitions ($\Delta T = 1$) with or without associated spin-flip processes ($\Delta S = 1$ or $\Delta S = 0$). This versatility has made them particularly effective for investigating Gamow-Teller (GT) transitions, Fermi (F) transitions, and higher-order excitations such as spin-dipole and quadrupole transitions, which are often remains inaccessible through conventional beta decay [8], [9].

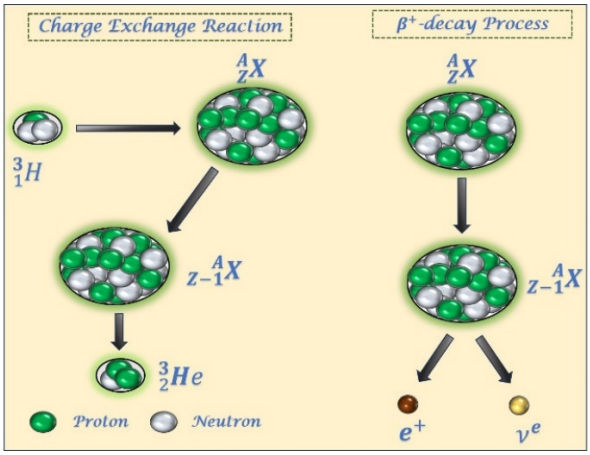

Figure 1. Illustration of (t, ^{3}He) charge exchange reaction and β^+- decay process

In recent decade, weak interaction research attracts the attention of scientists commonly around the globe, due to the fact that these processes determine fundamental explanations for nuclear physics and astrophysical phenomena. The mechanisms that control stellar evolution and initiate core-collapse supernovae remain governed by weak interaction processes. Furthermore, weak interactions play a critical role in rare nuclear processes like neutrino-less double-beta decay ($0\nu\beta\beta$), which has deep implications for understanding the nature of neutrinos and the asymmetry between matter and antimatter in the universe [10]-[13]. Additionally, weak interaction rates, particularly Gamow-Teller (GT) transition strengths characterised by changes in isospin ($\Delta T = 1$), spin ($\Delta S = 1$), and angular momentum ($\Delta L = 0$), are essential for modelling neutrino-driven nucleosynthesis pathways that contribute to the formation of heavy elements in astrophysical environments [14]-[17]. Charge exchange reactions like (t, ^{3}He) and (^{3}He, t) play a pivotal role in extracting these

Cite as: Ankita, P. Singh, East Eur. J. Phys. 2, 49 (2025), https://doi.org/10.26565/2312-4334-2025-2-06

transition strengths due to their ability to probe high-excitation energy states beyond the Q-value limitations inherent to β-decay, thereby allowing for comprehensive studies of weak interaction processes and their implications in stellar environments [18], [19]. These reactions offer high-resolution measurements, providing critical data for validating different theoretical models [20], [21].

As it is evident that at low momentum transfer, the differential cross-section measurements and GT transition strengths exhibit a well-documented proportionality, which is commonly called the unit cross-section ($\hat{\sigma}_{GT}$) [22], [23]. This relationship acts as an essential method for getting correct B(GT) values, which helps to validate theoretical models, including the shell model and quasiparticle random phase approximation (QRPA) [24]-[26]. Moreover, the experimental capabilities have been expanded through secondary triton beam developments to analyse GT strength distributions in various medium-mass nuclei [27]. Zegers et al. showed that (t, ^{3}He) along with (^{3}He, t) reactions provide effective GT probes that give matching experimental data with low probe sensitivity. The unit cross-sections $\hat{\sigma}_{GT}$ show equivalent mass dependency for nuclei having A ≥ 12, while following the relationship $\hat{\sigma}_{GT} = \frac{109}{A^{0.65}}$. This relation persists despite differences in beam energies between (t, ^{3}He) using 115 MeV/u and (^{3}He, t) using 140 MeV/u [20].

The accurate determination of Gamow-Teller strengths depends heavily on precise evaluation of knock-on exchange effects and tensor force interactions because due to approximate inclusion of these effects resulting in presence of systematic uncertainties to charge-exchange (CE) reaction results [22], [28]. However, experimental data matches more effectively with predications when antisymmetric DWIA models with precise knock-on exchange amplitudes are employed [21], [29]. Further, consideration of tensor interactions creates additional difficulties during GT strength measurements because it produces interference between the ΔL = 0 and ΔL = 2 multipoles. The interactions create systematic uncertainties reaching 20% for weak transitions [26]. Comparative studies, by Zegers et al., confirm that both (t, ^{3}He) and (^{3}He, t) reactions reliably extract Gamow-Teller (GT) strengths for weak-interaction. However, some inconsistencies arise due to consideration of higher multipole transitions (ΔL = 2) [29], systematic uncertainties from variations in optical model potentials and reaction dynamics leading to normalization discrepancies of 10–20% [14], and the pronounced impact of knock-on exchange effects requiring precise theoretical treatment for both the reaction [28].

Previously, we have examined (^{3}He, t) reaction on various targets using Distorted Wave Impulse Approximation (DWIA) at intermediate energy, wherein the importance of incorporation of knock-on exchange effects have been discussed [30]. However, in current work, we have examined (t, ^{3}He) charge exchange reaction at low and medium-mass nuclei at 140 MeV/nucleon for Gamow-Teller transitions. Both knock-on exchange effects and tensor force contributions have been incorporated to extract clearer and more precise information from these reactions.

RESULTS AND DISCUSSION

DWIA approach have been used in current work, which has been discussed in detail in refs. [30]-[32]. However, some important expressions used in calculations are discussed below. The differential cross-section may be computed by using below expression.

$$\frac{d\sigma}{d\Omega} = \frac{\mu_a \mu_b}{(2\pi\hbar^2)^2}\frac{k_b}{k_a}\left|\sum_{i=D,E}\sum_{k,l_1t_1}\alpha_{j_t s_t v_1}^{t_1 s_1 l_1 k l_t}\, T_i^{t_1 s_1 l_1 k l_t m_{l_t}}\right|^2. \quad (1)$$

In above, μ_a *and* μ_b are the reduced mass of reactants in incoming and outgoing channel while the wave number in incident and exit channel are accounted by k_a and k_b respectively. ($\alpha_{j_t s_t v_1}^{t_1 s_1 l_1 k l_t}$) is the expansion coefficient which is further formulated in terms of Racah coefficient (W).

Currently, there is no exact method available for calculating charge-exchange reactions involving composite particles. As a result, most calculations rely on pseudo-potential approximations whose accuracy can vary significantly depending on the projectile energy and target mass. Therefore, to gain clearer insights into the influence of exchange term and tensor force terms in distorted wave impulse approximation calculations, we present results for the differential cross-section of (t, ^{3}He) reactions on ^{12}C, ^{13}C, ^{26}Mg and ^{58}Ni at a beam energy of 140 MeV/nucleon focusing on Gamow-Teller (GT) transitions. The calculated differential cross-sections are illustrated in Figure 2 (a-d) for ^{12}C, ^{13}C, ^{26}Mg and ^{58}Ni respectively. To extract the cross-section at 0^o, the experimental differential cross-sections are fitted to the theoretical predictions obtained using the DWIA framework with the DCP-2 code. These calculations focus on transitions to final states with known GT strengths for the 1^+ ground state, as listed in Table 1. A key element in these calculations is the use of an effective nucleon-nucleon interaction potential (V), which plays a crucial role in accurately modelling the reaction dynamics and expressed as

$$V = \int dx_1 dx_2 dx_1' dx_2' \hat{\rho}_T(x_1 x_1')\hat{\rho}_P(x_2, x_2^1) v_{12}(x_1' x_2', x_1 x_2). \quad (2)$$

where, $x_i = (r_i, \sigma_i, \tau_i)$ stands for space, spin and iso-spin co-ordinate of i^{th} particle ($i = 1,2$) and x_i' co-ordinate denotes the x_i after the exchange of nucleons '1' and '2'. The interaction potential, expressed as $v_{12}(x_1' x_2', x_1 x_2) = x_1' x_2' V^D x_1 x_2 + (-)_l P^r x_1' x_2' V^E x_1 x_2$, with P^r as exchange operator, is a combination of direct and exchange part of the Love and Franey type effective interaction (V^i ($i = D$) for direct and ($i = E$) for exchange) [33], [34].

We also assume that the effective interactions contain both central and tensor terms. The tensor operator can be written as $\hat{S}_{12} = 3(\hat{\sigma}_1.\hat{r}\,)(\hat{\sigma}_2.\hat{r}\,) - (\hat{\sigma}_1.\hat{\sigma}_2\,) = \sum_q \sqrt{4\pi}\sqrt{\frac{2}{5}}\, Y^*_{2q}\hat{T}_{2q}$, where $\hat{T}_{2q}$ is a second rank tensor operator. The $\hat{\rho}_T(x_1, x_1')$ and $\hat{\rho}_P(x_2, x_2')$ respectively accounts the non-local densities for target and projectile. The value of B(GT) [14], [22] and the optical model potentials parameters (OMP) that are extracted from ^{3}He elastic scattering data are taken from refs. [35]-[38] while for outgoing channel (^{3}H) same parameters are used except potential depth which is modulated by multiplying with 0.85 [37]. The one body transition densities (OBTD's) give weight factors for each 1p-1h excitations and have been calculated using OXBASH code using sd-model space coupled with USD hamiltonian [39], while for heavier mass like ^{58}Ni, the pf-model space along with GXPF1 interactions has been used [40]. In addition, the radial wave functions used for the calculation of form factor are constructed with Woods-Saxon potential. The radial densities for the projectile (^{3}He) and ejectile (^{3}H), are obtained from Variational Monte Carlo calculations [41].

Table 1. Initial and final states of various systems excited by reaction (t, ^{3}He). B(GT) values tabulated below are calculated by employing method given in refs. [14], [22].

Initial (J^π, E)	Final (J^π, E)	B(GT)
$^{12}C(0^+, g.s.)$	$^{12}B(1^+, g.s.)$	0.99
$^{13}C(\frac{1}{2}^-, g.s.)$	$^{13}B(\frac{3}{2}^-, g.s.)$	0.711
$^{26}Mg(0^+, g.s.)$	$^{26}Na(1^+, 0.08)$	0.41
$^{58}Ni(0^+, g.s.)$	$^{58}Co(1^+, 1.87)$	0.72

Figure 2 presents the differential cross-section of (t, ^{3}He) charge exchange reaction for ^{12}C, ^{13}C, ^{18}O, ^{26}Mg, ^{58}Ni nuclei, focusing on their first Gamow-Teller (GT) states listed in Table 1.

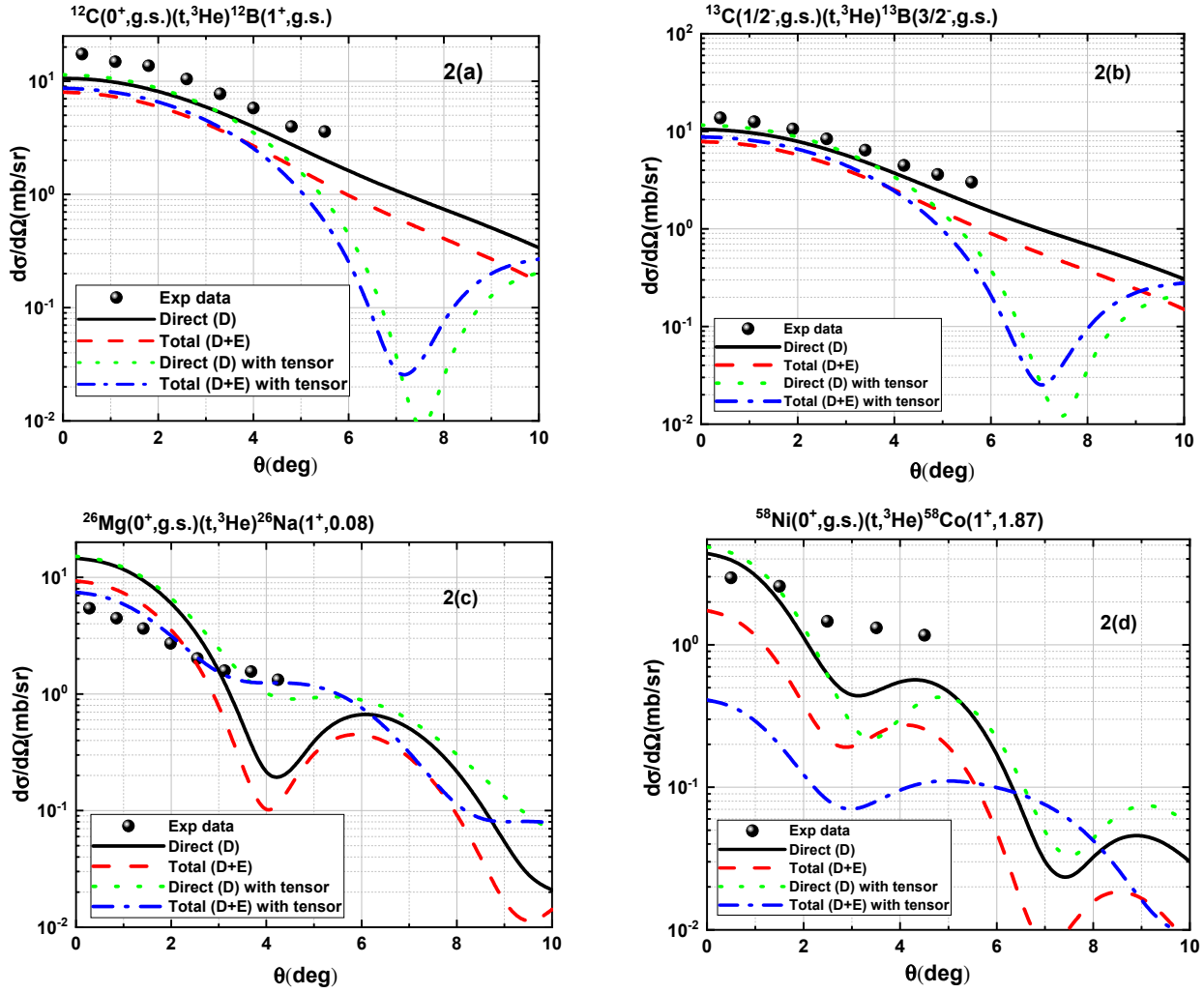

Figure 2. (Color online) The calculated differential cross-section for (t, ^{3}He) charge exchange reaction on ^{12}C, ^{13}C, ^{26}Mg and ^{58}Ni target using DWIA at 140 MeV/nucleon. The solid (black) and dashed (red) line represents the direct and total (D+E) contribution without tensor forces effect respectively. The dotted (green) and dash-dotted (blue) line represents the direct and total (D+E) contribution with tensor forces effect respectively. The solid (black) circle represents the experimentally measured data

For each target nucleus four sets of calculations were performed to evaluate the contributions of different interaction terms, (i) direct terms contributions without exchange terms calculations represented by Direct (D) (ii) direct terms with inclusion of knock-on exchange terms labelled as Total (D+E) (iii) while results obtained for tensor forces along with direct terms contribution represent are shown by Direct (D) with tensor (iv) the total contribution with tensor forces depicted by Total (D+E) with tensor. Quantitatively, the inclusion of exchange effects causes a significant reduction in the differential cross-section, in magnitudes up to 20% - 60% for all the targets considered in this work. Generally, calculations incorporating exchange terms effects, deviate from the experimental data, except for ^{26}Mg. A similar trend has been observed in earlier work performed with (^{3}He, t) reaction.

Furthermore, it is noticed that the inclusion of tensor force terms creates noticeable changes to the cross-sections, primarily in the forward scattering region. For ^{12}C and ^{13}C, the inclusion of tensor terms leads to a slight increase (up to 10%) in the differential cross-section at forward angles, constructively enhancing the cross-section and improving agreement with experimental data [22], [42]. In contrast, for ^{26}Mg and ^{58}Ni, the tensor forces interact destructively with the total (D+E) contributions. Although, for the case ^{26}Mg, tensor interference leads to a 20% reduction in the cross-section, narrowing the gap between theoretical predictions and experimental measurements [20]. For ^{58}Ni, the tensor contribution results in an even more pronounced reduction, up to 60%, which moves the theoretical predictions further away from the experimental data [14].

The variations in differential cross-sections across different nuclei can be explained by the role of the tensor component in the effective nucleon-nucleon interaction. This tensor force introduces interference between the $\Delta L = 0$ and $\Delta L = 2$ amplitudes, both contributing to $\Delta J = 1$ Gamow-Teller transitions. The nature of this interference is constructive as well as destructive, varies depending on the target nucleus and specific reaction conditions. These factors significantly influence the reaction mechanism and the degree of agreement between theoretical predictions and experimental data, depending on the target nucleus involved. To further analyze the reaction dynamics and quantify these effects, unit cross-sections have been calculated.

The unit cross-section $\hat{\sigma}_{GT}$ for charge-exchange (CE) reactions is determined using the relationship between the Gamow-Teller (GT) transition strength and the differential cross-section at zero momentum transfer, expressed as

$$\frac{d\sigma}{d\Omega}(q \to 0) = \hat{\sigma}_{GT} B(GT) \tag{3}$$

Calculating the unit cross-section typically requires known (B(GT) values, which are often obtained from β-decay measurements. In cases where such experimental data are unavailable, theoretical models must be employed to estimate the unit cross-section. Another approach involves using empirical formulas such as those presented in Ref. [20]. However, it is important to recognize that empirical methods have limited precision and theoretical calculations are generally necessary for more accurate determinations. However, we have calcuated the unit cross-section for (t, ^{3}He) charge exchange reactions and shows its variations over different target nuclei ^{12}C, ^{13}C, ^{26}Mg and ^{58}Ni.

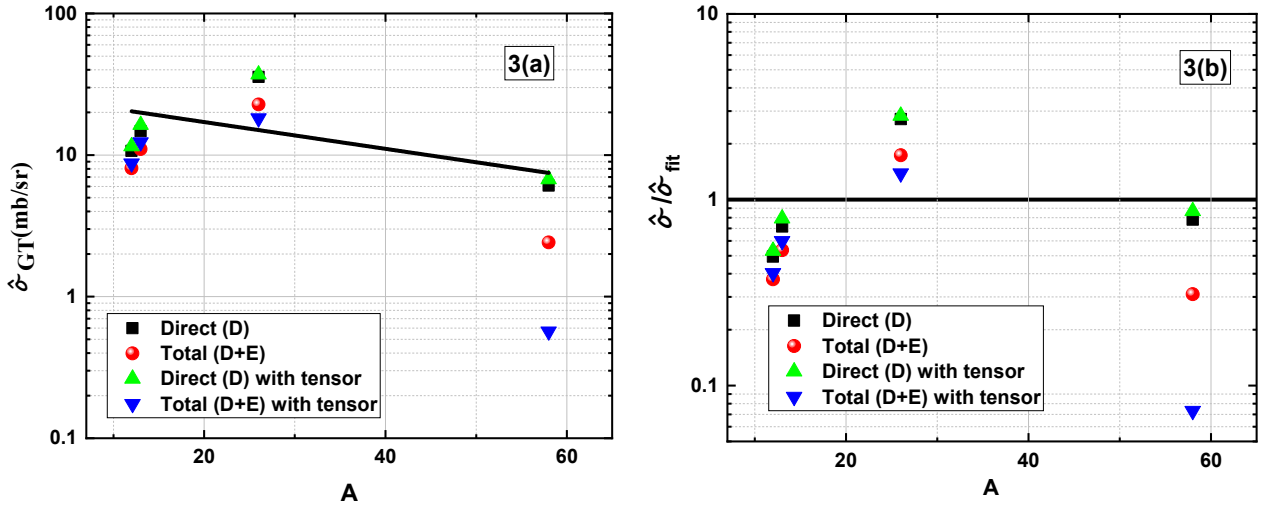

Figure 3. (Color online) (a) The calculated unit cross-section for (^{3}He, t) Charge exchange reactions on targets ^{13}C, ^{26}Mg, ^{58}Ni and ^{120}Sn for GT transitions. (b) shows the ratio of the calculated and experimental unit cross-sections relative to the fitted cross-section for Gamow-Teller transitions. In both figs., the solid square (black) and circle (red) shows direct and total (D+E) calculations without incorporating tensor forces. While upward triangle (green) and downward triangle (blue) is showing the results after consideration tensor forces in the calculation with direct and total (D+E) term respectively. The solid (black) line represents the unit cross-section obtained through fitted empirical function

Figure 3 presents four distinct calculations for each target along with the results obtained through empirical relation, $\hat{\sigma}_{GT,fit} = 109/A^{0.65}$, which is a power fit to experimental data [14]. In Figures 3 (a) and 3(b), respectively the solid square

(black) and circle (red) shows direct and total (D+E) calculations without incorporating tensor forces. While upward triangle (green) and downward triangle (blue) is showing the results after consideration tensor forces in the calculation with direct and total (D+E) term respectively. The solid (black) line in the figure corresponds to the unit cross-section obtained through empirical formula. To evaluate the reliability of the conclusions drawn from the empirical relation $\hat{\sigma}_{GT,fit} = 109/A^{0.65}$, Figure 3 (b) shows the ratio of the calculated and experimental unit cross-sections relative to the fitted cross-section for Gamow-Teller transitions. This comparison helps to validate the theoretical calculations, especially in cases where experimental data is lacking.

In Figure 3 (a) it is evident that for ^{12}C, ^{13}C and ^{58}Ni nuclei, both the direct and total (D+E) calculations without tensor forces underestimate the unit cross-section predicted by the empirical fit. Conversely, for ^{26}Mg, the calculated values overestimate the empirical data. Furthermore, when tensor forces are incorporated into the direct and total (D+E) calculations, there is a noticeable reduction in the differential cross-section, by up to a factor of 2 for ^{26}Mg and up to 4 for ^{58}Ni. In contrast, for ^{12}C and ^{13}C, the inclusion of tensor forces results in only a slight increase in the cross-section magnitude compared to the results without tensor forces. Overall, the addition of tensor forces tends to align the calculated results more closely with the empirical fit for ^{12}C, ^{13}C and ^{26}Mg, improving the agreement between theory and experiment. However, for ^{58}Ni, the results further deviate from the empirical fit upon including tensor contributions. These variations arise from the behavior of the tensor component in the effective nucleon-nucleon interaction, which eventually influences the charge-exchange reaction results. Specifically, this tensor force induces interference between the $\Delta L = 0$, $\Delta S = 1$ amplitudes (mediated by the $\sigma\tau$ component) and the $\Delta L = 2$, $\Delta S = 1$ amplitudes (mediated by the tensor-τ component). Since both of these transitions contribute to the $\Delta J = 1$ Gamow-Teller transitions, the nature of the interference can be either constructive or destructive, depending on the specific nuclear system and reaction conditions.

SUMMARY AND CONCLUSION

In this work, (t, ^{3}He) charge-exchange reactions at 140 MeV/nucleon on ^{12}C, ^{13}C, ^{26}Mg and ^{58}Ni targets have been examined. Differential cross-sections and unit cross-sections have been computed by incorporating both knock-on exchange effects and tensor force components through DWIA approach with computer code DCP-2. Calculations shows that knock-on exchange effects reduced the predicted cross-sections by 20% - 60%. Further, it has been also noticed that the incorporation of exchange terms produces better predictions of experimental results for ^{26}Mg nuclei. It is worth to mention here that the inclusion of tensor force terms produces intricate patterns of destructive and constructive interference between the $\Delta L = 0$ and $\Delta L = 2$ components. The destructive interference has been noticed in case of ^{26}Mg and ^{58}Ni which eventually causes to reduction cross-sections up to 60%. A good agreement between calculated unit cross-sections and experimental data has been found for all the targets considered here except ^{58}Ni.

In conclusion, the study establishes fundamental understanding of (t, ^{3}He) process behavior while demonstrating the requirement of considering advanced nuclear interactions for achieving accurate theoretical predictions.

Acknowledgment

The First author would like to acknowledge University Grant Commission (UGC) for providing the fellowship vide Ref. No. 19/06/2016(i)EU-V.

ORCID

Ankita, https://orcid.org/0000-0001-5769-2907; **Pardeep Singh,** https://orcid.org/0000-0003-2100-3772

REFERENCES

[1] T.N. Taddeucci, et al., Nucl. Phys. A **469**, 125 (1987), https://doi.org/10.1016/0375-9474(87)90089-3
[2] M.N. Harakeh, and A.V. Woude, *Giant Resonances: Fundamental High Frequency Modes of Nuclear Excitations*, (Oxford University, New York, 2001).
[3] B. Gao, et al., Phys. Rev. C **101**, 014308 (2020), https://doi.org/10.1103/PhysRevC.101.014308
[4] J. J. Li, et al., Phys. Rev. C **102**, 064601 (2020), https://doi.org/10.1103/PhysRevC.102.064601
[5] Y. Fujita, et al., Phys. Rev. C **67**, 064312 (2003), https://doi.org/10.1103/PhysRevC.67.064312
[6] B. T. Kim, et al., Phys. Rev. C **61**, 044611 (2000), https://doi.org/10.1103/PhysRevC.61.044611
[7] D. T. Khoa, et al., Phys. Rev. C **76**, 014603 (2007), https://doi.org/10.1103/PhysRevC.76.014603
[8] D. Vale, et al., Phys. Rev. C **103**, 064307 (2021), https://doi.org/10.1103/PhysRevC.103.064307
[9] D. Gambacurta, et al., Phys. Rev. Lett. **125**, 212501 (2020), https://doi.org/10.1103/PhysRevLett.125.212501
[10] F. T. Avignone, et al., Rev. Mod. Phys. **80**, 481 (2008), https://doi.org/10.1103/RevModPhys.80.481
[11] J. Engel, et al., Rep. Prog. Phys. **80**, 046301 (2017), https://doi.org/10.1088/1361-6633/aa5bc5
[12] J. Menendez, et al., J. Phys. G **45**, 014003 (2017), https://doi.org/10.1088/1361-6471/aa9bd4
[13] F. Cappuzzello, et al., Prog. Part. Nucl. Phys. **128**, 103999 (2023), https://doi.org/10.1016/j.ppnp.2022.103999
[14] A. L. Cole, et al., Phys. Rev. C **74**, 034333 (2006), https://doi.org/10.1103/PhysRevC.74.034333
[15] Y. Fujita, et al., Phys. Rev. C **70**, 011306(R) (2004), https://doi.org/10.1103/PhysRevC.70.011306
[16] F. Diel, et al., Phys. Rev. C **99**, 054322 (2019). https://doi.org/10.1103/PhysRevC.99.054322
[17] H. Fujita, et al., Phys. Rev. C **100**, 034618 (2019), https://doi.org/10.1103/PhysRevC.100.034618
[18] J. C. Zamora, et al., Phys. Rev. C **100**, 032801 (2019), https://doi.org/10.1103/PhysRevC.100.032801
[19] S. Noji, et al., Phys. Rev. C **92**, 024312 (2015), https://doi.org/10.1103/PhysRevC.92.024312
[20] R.G.T. Zegers, et al., Phys. Rev. C **74**, 024309 (2006), https://doi.org/10.1103/PhysRevC.74.024309

[21] T. Udagawa, A. Schulte, and F. Osterfeld, Nucl. Phys. A, **474**, 131 (1987). https://doi.org/10.1016/0375-9474(87)90197-7
[22] G. Perdikakis, *et al*., Phys. Rev. C, **83**, 054614 (2011). https://doi.org/10.1103/PhysRevC.83.054614
[23] R.G.T. Zegers, *et al*., Phys. Rev. Letts. **99**, 202501 (2007). https://doi.org/10.1103/PhysRevLett.99.202501
[24] R. Titus, *et al*., J. Phys. G: Nucl. Part. Phys. **45**, 014004 (2017). https://doi.org/10.1088/1361-6471/aa98c1
[25] R. Titus, *et al*., Phys. Rev. C, **100**, 045805 (2019). https://doi.org/10.1103/PhysRevC.100.045805
[26] A. L. Cole, *et al*., Phys. Rev. C, **86**, 015809 (2012). https://doi.org/10.1103/PhysRevC.86.015809
[27] G.W. Hitt, *et al*., Nuclear Instruments and Methods in Physics Research A **566**, 264 (2006). https://doi.org/10.1016/j.nima.2006.07.045
[28] B. T. Kim, *et al*., Phys. Rev. C, **61**, 044611 (2000). https://doi.org/10.1103/PhysRevC.61.044611
[29] A. Schulte, e*t al*., Phys. Lett. B, **183**, 243 (1987). https://doi.org/10.1016/0370-2693(87)90956-7
[30] Ankita, and P. Singh, Mod. Phys. Lett. A, **38**, 2350066 (2023). https://doi.org/10.1142/S0217732323500669
[31] Riken, https://www.nishina.riken.jp/researcher/archive/program., Nishina center for accelerator-based science.
[32] P. Singh, *et al*., Mod. Phys. Lett. A, **35**, 2020045 (2020). https://doi.org/10.1142/S0217732320500455
[33] W.G. Love, and M.A. Franey, *et al*., Phys. Rev. C, **24**, 1073 (1981). https://doi.org/10.1103/PhysRevC.24.1073
[34] M.A. Franey, and W.G. Love, *et al*., Phys. Rev. C, **31**, 488 (1985). https://doi.org/10.1103/PhysRevC.31.488
[35] H. Fujimura, et al., Phys. Rev. C **69**, 064327 (2004). https://doi.org/10.1103/PhysRevC.69.064327
[36] T. Yamagata, et al., Nucl. Phys. A **589**, 425 (1995). https://doi.org/10.1016/0375-9474(95)00071-8
[37] S. Y. Van Der Werf et al., Nucl. Phys. A **496**, 305 (1989). https://doi.org/10.1016/0375-9474(89)90177-2
[38] J. Kamiya, et al., Phys. Rev. C, **67**, 064612 (2003). https://doi.org/10.1103/PhysRevC.67.064612
[39] M. Honma, *et al*., Phys. Rev. C, **69**, 034335 (2004). https://doi.org/10.1103/PhysRevC.69.034335
[40] C.A. Douma, *et al*., Eur. Phys. J. A, **56**, 51 (2020). https://doi.org/10.1140/epja/s10050-020-00044-9
[41] S.C. Pieper, *et al*., Annu. Rev. Nucl. Part. Sci. **51**, 53 (2001). https://doi.org/10.1146/annurev.nucl.51.101701.132506
[42] C.J. Guess, *et al*., Phys. Rev. C, **80**, 024305 (2009). https://doi.org/10.1103/PhysRevC.80.024305

ДОСЛІДЖЕННЯ РЕАКЦІЙ ОБМІНУ ЗАРЯДУ (t, ^{3}He): ВРАХУВАННЯ ЧЛЕНІВ ОБМІНУ ВИБИВАННЯМ ТА ТЕНЗОРНОЇ СИЛИ

Анкіта, Пардіп Сінгх

Фізичний факультет, Університет науки та технологій імені Дінбанду Чхоту Рама, Муртал, Соніпат 131039, Харьяна, Індія

У цьому дослідженні використовується структура DWIA (Distorted Wave Impulse Approximation), яка дозволяє досліджувати вплив ефектів обміну вибиванням разом із внесками тензорної сили під час дослідження реакцій обміну зарядом. Тут було обчислено диференціальний переріз і одиничний переріз для (t, ^{3}He) реакцій обміну зарядом на мішенях ^{12}C, ^{13}C, ^{26}Mg і ^{58}Ni. Отримані результати демонструють, що врахування умов обміну суттєво зменшує розрахунковий переріз. Крім того, внесок тензорних сил вносить додатковий рівень складності в аналіз реакцій обміну зарядом. Залежно від цільового ядра, внесок тензорних сил створює або конструктивні, або деструктивні ефекти інтерференції, що призводить або до збільшення, або до зменшення величини поперечного перерізу на основі цільового ядра. Прогнозовані одиничні перерізи узгоджуються з відповідними експериментальними даними, але демонструють специфічні відхилення через тензорні взаємодії, які найбільш виражені в ^{58}Ni.

Ключові слова: *переходи Гамова-Теллера; реакція обміну заряду; тензорні сили; апроксимація спотвореного хвильового імпульсу; кутовий розподіл; поперечний переріз*

East European Journal of Physics. 2. 55–73 (2025)
DOI: 10.26565/2312-4334-2025-2-07 ISSN 2312-4334

GLOBAL COUPLED-CHANNELS PHENOMENOLOGICAL OPTICAL MODEL POTENTIAL FOR NEUTRON - NUCLEUS SCATTERING FROM ^{6}Li TO ^{238}U

Waleed Saleh Alrayashi*
Science Department, Faculty of Education, Sana'a University, Sanna'a, Yemen
*Corresponding Author e-mail: walrayashi@su.edu.ye
Received February 23, 2025; revised March 21, 2025; in final form April 2, 2025; accepted April 12, 2025

The neutron - nucleus scattering process is considered to develop smooth functional forms for the real and imaginary parts of the phenomenological optical potential using the formalism of coupled - channels analysis. We consider intermediate and heavy nuclear targets and investigate the possibility of extending the model to the usually excluded case of light nuclei. Using our model, we simultaneously predict elastic and inelastic angular distributions for neutron scattering from ^{6}Li to ^{238}U for various energies in the range 100 keV $< E <$ 30 MeV for which inelastic angular distributions data are available. We obtain smooth forms for the real and imaginary depths of the volume and surface potential terms as functions of energy, mass number and the asymmetry between the proton and neutron numbers in the target nucleus. The depths of the real and imaginary spin - orbit term, and all the geometry parameters of the potential are fixed. Our predicted elastic and inelastic differential cross sections are in very good agreement with the measured data. The calculated total elastic, total cross sections and the analyzing powers are in a fair overall agreement with the experimental values particularly for the intermediate and heavy nuclei.

Keywords: *Optical model potential; Elastic scattering; Inelastic scattering; Coupled channels; Differential cross section*

PACS: 24.10.Eq, 24.10.Ht, 25.40.Dn, 25.40.Ep, 24.10.-i

1. INTRODUCTION

The optical model describes the complicated interaction between the projectile and target in terms of a complex potential. This potential divides the reaction flux into a real part which corresponds to elastic scattering, and an imaginary part that corresponds to all competing inelastic channels [1]. The main goal of the optical model is to determine potential parameters that can reproduce smooth variations of the scattering differential cross section as a function of the energy of the incident particle and nucleon number of the target nucleus. Although the scattering process may be complicated, noticeable simplification may be achieved if one is only interested in the averaged properties, away from resonances and excitation channels that can be reached by direct reactions. For example, local and also global optical potentials for scattering of nucleons off spherical and approximately spherical nuclei were obtained for incident energies in the range 1 keV to 200 MeV, and target mass numbers that fall in the range $24 \leq A \leq 209$, for which the appropriate experimental data were available [2]. In addition, a global phenomenological optical potential for nucleon scattering off actinides for incident energies up to 300 MeV was developed by considering experimental data for nucleon scattering from ^{232}Th and ^{238}U [3]. Nuclei with charge and mass numbers $89 \leq Z \leq 100$ and $220 \leq A \leq 260$ respectively were included in the study. Furthermore, in Ref. [4], the authors developed optical potentials for medium- and heavy-weight nuclei from ^{54}Fe to ^{238}U corresponding to nucleons incident with energies in the 1 keV to 200 MeV range. Using coupled-channels analysis, the authors obtained smooth systematics for the potential parameters which have simple functional forms. Their results also confirmed that coupled-channels analysis were indispensable to achieving a global description of experimental data for wide ranges of energies and mass numbers $50 \leq A \leq 240$. Other more recent works considered nucleon scattering from light, intermediate and heavy nuclei using a velocity-dependent potential [8] - [11] that reproduced the elastic angular distributions and polarization data to a very good extent, particularly the prominent large angle minima that correspond to nucleon scattering off light $1p$-shell nuclei. Other works modeled the nucleon - nucleus scattering process using the nonlocal Perey and Buck (PB) potential [12] - [14]. The agreement between the predicted angular distributions and experiment was found to be quite satisfactory. Although the PB potential is a nonlocal potential, it was shown that nonlocality alone was not enough to completely describe the proton experimental data, and energy dependent parameters were needed to improve agreement with experiment [15].

In this work, we employ the coupled - channel analysis to develop an optical potential for neutron scattering off various nuclei from ^{6}Li to ^{238}U. This range includes light nuclei: ^{6}Li, ^{12}C and ^{16}O, which are usually excluded when global optical potentials are developed. Their diffuse edges complicate the process of predicting their angular distributions and total cross sections even when local optical potentials are attempted [16]. Despite such difficulties, in this work, we examine the possibility of extending our model to the case of light nuclei. Therefore, in our calculations we consider incident neutrons on nuclei with mass numbers that fall in the range $6 \leq A \leq 238$. The considered nuclei, coupled energy levels and best-fit deformation parameters are given in Table 1. Following the authors of Refs. [3] to [4] and [17], we fix

Cite as: W. S. Alrayashi, East Eur. J. Phys. 2, 55 (2025), https://doi.org/10.26565/2312-4334-2025-2-07

the values of the geometrical parameters and the depths of the spin - orbit term. In addition, we parametrize the real and imaginary parts of the potential as smooth functions of the incident neutron energy, mass number of the target nucleus and the asymmetry between the number of protons and neutrons of the target.

This article is structured as follows. In Section 2 we outline the coupled channels formalism, while Section 3.1 describes the process of deriving our optimal set of parameters. We discuss our results in Section 4. Finally, we present our conclusions in Section 5.

2. COUPLED REACTION CHANNELS FORMALISM

The coupled reaction channels (CRC) is essential for describing scattering processes. When the projectile interacts with the target, the interaction can result in elastic scattering, transitions to excited-state exit channels, or even rearrangement processes. The simplest case occurs when the spin of the target nucleus (I_t) is zero, which is true for even-even nuclei. However, for an odd-A nucleus, I_t is a half-integer, while for an even-A nucleus, I_t is an integer. In elastic scattering, the projectile and the target remain in their ground states after the reaction, and the corresponding Q-value is zero. In this case, the total kinetic energy of the system is conserved in the center-of-mass (C.M.) frame. The scattering potential merely redistributes the outgoing particles without any loss of incident flux. A clear example is:

$$\mathrm{p} + {}^{24}_{12}\mathrm{Mg} \longrightarrow \mathrm{p} + {}^{24}_{12}\mathrm{Mg} \tag{1}$$

In inelastic scattering processes, the kinetic energy of the system is not conserved. Both the projectile and the target retain their identities, but one or both may be excited to higher energy states. Part of the kinetic energy of the relative motion is transferred to internal excitation energy. Inelastic scattering typically occurs when one or both nuclei are deformed. An example of such a process is:

$$\mathrm{p} + {}^{24}_{12}\mathrm{Mg} \longrightarrow \mathrm{p} + {}^{24}_{12}\mathrm{Mg}^{*}(I^{\pi} = 2^{+}, 4^{+}, 6^{+}, \ldots) \tag{2}$$

The coupled-channel theory is a powerful method for incorporating inelastic channels, especially those arising from collective excitations. The formalism was first introduced by Bohr and Mottelson [18], and was later applied by Margolis et al. and Chase et al. [19]. Here, we provide a brief outline of the coupled-channel analysis. A more detailed description can be found in Ref. [20]. In the center-of-mass frame (C.M.), the Schrödinger equation for a nucleon scattered by a target nucleus takes the form:

$$\left[\hat{T}(r) + H(\xi_t) + V(r, \xi_t)\right]\Psi(\vec{r}, \xi_t) = E\Psi(\vec{r}, \xi_t), \tag{3}$$

where r is the radial coordinate from the target to the projectile, and $H(\xi_t)$ is the Hamiltonian for the internal motion of the target, while ξ_t represents the internal coordinates of the target. The interaction potential, $V(r, \xi_t)$ which can be expressed as [20]

$$V(r, \xi_t) = V_{diag} + V_{coupl}, \tag{4}$$

where V_{diag} is a scalar potential that simulates elastic scattering, while V_{coupl} represents the interaction that couples the initial and final states and therefore takes care of inelastic scattering. Further, $\hat{T}(r)$ is the total kinetic energy, which may be written as

$$\hat{T}(r) = -\frac{\hbar^2}{2\mu}\nabla_r^2, \tag{5}$$

where $\mu = \frac{m_p m_t}{m_p + m_t}$ is the reduced mass of the projectile and target, and ∇_r^2 is the Laplacian operator. where, E is the total energy, and $\Psi(\vec{r}, \xi_t)$ is the wave function of the whole system. Now we shall expand $\Psi(\vec{r}, \xi_t)$ in terms of the eigenstates of the total angular momentum $\psi_J^{\pi M}(\vec{r}, \xi_t)$ as follows [20]:

$$\Psi(\vec{r}, \xi_t) = \sum_{\pi J M} A_{JM}\, \psi_J^{\pi M}(\vec{r}, \xi_t), \tag{6}$$

For each channel $[(l_n s) j_n, I_n]$, where J is the total angular momentum of the whole system;

$$\vec{\mathrm{J}} = \vec{\mathrm{j}}_n + \vec{\mathrm{I}}_n, \tag{7}$$

such that $\vec{\mathrm{j}}_n = \vec{l}_n + \vec{\mathrm{s}}$, where l_n is the orbital angular momentum quantum number, s is the spin of the projectile and I_n is the target's spin, M is the projection of J in units of $\hbar$, and the factors A_{JM} are the amplitudes specifying how much of a total angular momentum state is present. In addition, the parity of the whole system has the form:

$$\pi = (-1)^{l_n}\pi_{I_n}, \tag{8}$$

where π_{I_n} is the parity of the target nucleus. Furthermore, we use the expansion

$$\psi_J^{\pi M}(\vec{r},\xi_t) = \sum_{n(l_n s)j_n I_n} \frac{1}{r} R^{\pi J}_{n(l_n s)j_n I_n}(r)\, \Phi^{JM}_{l_n j_n I_n}(\hat{r},\xi_t), \tag{9}$$

The nuclear wave functions are defined as:

$$\begin{aligned}\Phi^{JM}_{l_n j_n I_n}(\hat{r},\xi_t) &= \sum_{m_{j_n} m_{I_n}} \sum_{m_{l_n} m_s} < l_n s\, m_{l_n} m_s \mid j_n m_{j_n} >< j_n I_n m_{j_n} m_{I_n} \mid JM > \\ &\times\ i^{l_n} Y^{m_{l_n}}_{l_n}(\hat{r})\, \chi^{m_s}_s\, \phi^{m_{I_n}}_{I_n}(\xi_t),\end{aligned} \tag{10}$$

where $R^{\pi J}_{nl_n j_n I_n}(r)$ are the radial wave functions, while $Y^{m_{l_n}}_{l_n}(\hat{r})$ are the spherical harmonics. The matrix elements $< l_n s m_{l_n} m_s \mid j_n m_{j_n} >$ are the Clebsch-Gordon coefficients for coupling $l_n m_{l_n}$ and $s m_s$ to an intermediate angular momenta $j_n m_{j_n}$, while the the elements $< j_n I_n m_{j_n} m_{I_n} \mid JM >$ are the Clebsch-Gordon coefficients for coupling $j_n m_{j_n}$ and $I_n m_{I_n}$ to a total of angular momentum JM for the whole system. Finally, $\phi^{m_{I_n}}_{I_n}(\xi_t)$ and $\chi^{m_s}_s$ are the wave functions for the target and projectile, respectively. Now, by substituting Eqs. (6), (9), and (10) into Eq. (3) and noting that

$$H_t(\xi_t)\phi^{m_{I_n}}_{I_n}(\xi_t) = \epsilon_n \phi^{m_{I_n}}_{I_n}(\xi_t), \tag{11}$$

one obtains

$$\sum_{nl_n j_n I_n} \left[\hat{T}_{n\,l_n} + V(r,\xi_t) - E_n\right] R^{\pi J}_{nl_n j_n I_n}(r)\, \Phi^{JM}_{l_n j_n I_n}(\hat{r},\xi_t) = 0, \tag{12}$$

where

$$\hat{T}_{n\,l_n} = \frac{\hbar^2}{2\mu_n}\left[-\frac{d^2}{dr^2} + \frac{l_n(l_n+1)}{r^2}\right], \tag{13}$$

Here, ϵ_n is the eigenenergies for the target, and $E_n = E - \epsilon_n$ is the external energy for a given excited state. Multiplying Eq. (12) by $[\Phi^{JM}_{n' l_{n'} j_{n'} I_{n'}}(\hat{r},\xi_t)]^*$ from the left, and integrating over the internal coordinates except the radial variable r, leads to the following partial wave coupled differential equations:

$$\left[E_n - \hat{T}_{n\,l_n} - V_{diag}(r)\right] R^{\pi J}_{nl_n j_n I_n}(r) = \sum_{n' l_{n'} j_{n'} I_{n'}} \left\langle l_n j_n I_n | V_{coupl} | l_{n'} j_{n'} I_{n'} \right\rangle R^{\pi J}_{n' l_{n'} j_{n'} I_{n'}}(r). \tag{14}$$

The matrix elements for the coupling potential are given by

$$\left\langle l_n j_n I_n | V_{coupl} | l_{n'} j_{n'} I_{n'} \right\rangle = \left\langle [\mathcal{Y}_{l_n j_n}(\hat{r}) \otimes \phi_{I_n}(\xi_t)]^M_J | V_{coupl} | [\mathcal{Y}_{l_{n'} j_{n'}}(\hat{r}) \otimes \phi_{I_{n'}}(\xi_t)]^M_J \right\rangle. \tag{15}$$

Nuclear structure deformations affect the matrix elements on the right-hand side of Eq. (14). For a non-deformed target nucleus, the coupling potential vanishes, and the set of coupled differential equations reduces to that of the Schrödinger equation for a single channel. Deformed nuclei can be described using either the vibrational or rotational models. In this work, we use the optical model and coupled-channel analysis to couple the ground state to collective excited states of the target nucleus.

This coupling introduces off-diagonal elements in the interaction potential matrix, allowing the incident neutron to induce transitions from the ground state to inelastic states such as the 2^+ state at 4.44 MeV in ^{12}C. These coupling potentials, typically derived from nuclear deformation (e.g., using a deformation parameter β), significantly affect observables such as scattering cross sections and resonance structures. As a result, including channel coupling provides a more accurate description of the reaction dynamics, especially for deformed nuclei like ^{12}C.

3. THE OPTICAL POTENTIAL PARAMETERS

For nucleon-nucleus scattering, the phenomenological optical potential, $V(r,E)$, can be expressed as [20]

$$\begin{aligned}V(r,E) &= -\Big(V_v(E) + iW_v(E)\Big) f(r,R_v,a_v) + i4a_s W_s(E)\frac{d}{dr} f(r,R_s,a_s) \\ &+ \Big(V_{so} + iW_{so}\Big)\Big(\frac{\hbar}{m_\pi c}\Big)^2 \frac{1}{r}\frac{d}{dr} f(r,R_{so},a_{so})\vec{L}\cdot\vec{\sigma},\end{aligned} \tag{16}$$

where $V_v(E)$ and V_{so} are the real components of the volume-central and spin-orbit potentials, respectively. In addition, $W_v(E)$, $W_s(E)$ and W_{so} are the respective imaginary components of the volume, surface and spin-orbit potentials. E is the energy of the incident particle in the laboratory frame. The Woods-Saxon potential has the well-known form:

$$f(r,R_i,a_i) = \frac{1}{1+\exp\left[(r-R_i)/a_i\right]}, \quad i = v,s,so. \tag{17}$$

Deformed nuclei whose surfaces vibrate about an equilibrium shape are treated using the vibrational model. Here, the dynamic nuclear radius R_i is taken to be a function of the polar angles θ and ϕ according to:

$$R_i(\theta,\phi) = r_i A^{\frac{1}{3}}\left[1 + \sum_{\lambda\geq 1}^{\infty}\sum_{\mu=-\lambda}^{\mu=\lambda} \alpha_{\lambda\mu} Y_{\lambda\mu}(\theta,\phi)\right], \tag{18}$$

where $R_i(\theta,\phi)$ is the distance from the center of the nucleus to a point at its surface subtending polar and azimuthal angles (θ,ϕ). The spherical tensors $\alpha_{\lambda\mu}$ are the spherical harmonics $(Y_{\lambda\mu}(\theta,\phi))$ coefficients. However, some nuclei have permanent deformations about a symmetry axis and are treated using the rotational model. In this case the nuclear radius is expressed in the form:

$$R_i(\theta') = r_i A^{\frac{1}{3}}\left[1 + \sum_{\lambda} \beta_\lambda Y_{\lambda 0}(\theta')\right], \tag{19}$$

where, θ' is the polar angle in the body - fixed frame and β_λ is the deformation parameter.

When the vibrational or rotational models are used, one has to determine which parts of the potential are to be deformed. Since the nuclear force is a short range force the nuclear potential follows the shape of the nucleus. Therefore, it is a common practice to deform the volume term of the potential. Deforming the imaginary - surface part, however, is a matter of dispute. This issue has been discussed and arguments were presented in support and also against deforming the imaginary surface part [22]. However, in a later work [23], the authors stated that " to describe the inelastic scattering best, it is found necessary to deform the imaginary (as well as the real) part of the central potential". Furthermore, in Ref. [24] the authors used an optical model with channel coupling to analyze nucleon induced reactions. All parts of the nuclear potential were deformed except the spin-orbit term. In Ref. [21] we examined the effect of channel coupling on the variation of the potential parameters corresponding to nucleon scattering off light and heavy nuclei. We obtained excellent angular distribution fits for the elastic and inelastic channels by deforming both the real volume and imaginary surface terms. Therefore, in this work, we shall deform the surface imaginary term in addition to the real volume term. We did not deform the spin - orbit term as the effects of its deformation on the calculated differential cross sections were found to be insignificant [25].

3.1. Global Optical Potential Parameters

Following the parametrization of Refs. [3] and [17], we express the depths of the optical potential as functions of incident energy, the target's mass number and the asymmetry between the numbers of neutrons and protons $(N-Z)$ in the form:

$$\begin{aligned} V_v(E) &= v_0 + v_1 E + v_2 E^2 + v_3\frac{N-Z}{A} + v_4\frac{Z}{A^{\frac{1}{3}}}, \\ W_v(E) &= W_0 + W_1 E + W_2\frac{N-Z}{A}, \\ W_s(E) &= w_0 + w_1 E + w_2 E^2 + w_3\frac{N-Z}{A}, \end{aligned} \tag{20}$$

where N and Z are the neutron and proton numbers of the target nucleus, respectively, and E is the energy of the incident nucleon in the laboratory frame. Using the SFRESCO code [26] we performed a least-square fit analysis to search for best-fit parameters v_i, W_i and w_i that best reproduce the elastic, inelastic and polarization data for each of the considered nuclei. Following the works of Refs. [3], [4] and [17], we fixed the values of the radius and diffuseness parameters r_i and a_i given in Eq. (17) in addition to the values of the real and imaginary depths of the spin-orbit term as follows:

$$\begin{aligned} r_v &= r_s = 1.20 \text{ fm}, \qquad a_v = 0.65 \text{ fm}, \; a_s = 0.60 \text{ fm} \\ r_{so} &= 1.10 \text{ fm}, \qquad a_{so} = 0.60 \text{ fm} \\ V_{so} &= 6.0 \text{ MeV}, \qquad W_{so} = 0.5 \text{ MeV}, \end{aligned} \tag{21}$$

For each nucleus, we determined the values of the central volume and surface absorption depths for each incident energy by fitting the available corresponding elastic and inelastic angular distributions in addition to the polarization data. After determining the best values of the depths in Eq. (20), we used the OriginLab software to determine the optimum values of v_i, W_i and w_i that best describe the variation of the depths as a function of E, A and $N-Z$ as follows:

$$\begin{aligned} V_v(E) &= 53.54 - 0.102E - 0.00879E^2 - 20\frac{N-Z}{A} + 0.0656\frac{Z}{A^{\frac{1}{3}}}, \\ W_v(E) &= 0.6 + 0.14E - 7.4\frac{N-Z}{A}, \end{aligned}$$

$$\begin{aligned} W_s(E) &= 1.697 + 0.303E - 0.0054E^2 + 7.4\frac{N-Z}{A}, \\ W_s(E) &= -1.303 + 0.303E - 0.0054E^2 + 7.4\frac{N-Z}{A}, \quad \text{only for } ^{12}\text{C and}^{16}\text{O}, \end{aligned} \tag{22}$$

The contribution of compound nucleus formation to the scattering process becomes important at low energies. In addition, the low energy data is vital in testing the applicability of an optical potential. Therefore, we tested the accuracy of our model's predictions at low energies using the TALYS computer code [27], which accounts for the compound nucleus formation, but with our values for all the optical potential parameters. As we shall see below, the agreement between our predictions and the experimental data is quite reasonable at incident energies as low as 180 keV.

We note here that the deformation parameters β were included in the fitting procedure. The best fit values are shown in Table 1. The initial values for the deformation parameters were taken from Refs. [23] and [29] to [33].

Table 1. The coupled energy levels and the corresponding best-fit deformation parameter for each considered nucleus.

Target	Coupled levels I^π (Excitation energy in MeV)	deformation parameters
^{6}Li	1^+ (g.s), 3^+(2.186)	β_2=1.1006
^{12}C	0^+ (g.s), 2^+(4.438),	β_2 =0.655
^{16}O	0^+ (g.s), 3^-(6.129), 2^+(6.917)	β_2 = 0.364, β_3= 0.7243
^{24}Mg	0^+ (g.s), 2^+(1.368)	β_2 = 0.499
^{28}Si	0^+ (g.s), 2^+(1.779), 4^+(4.617)	β_2 = 0.40, β_4=0.25
^{32}S	0^+ (g.s), 2^+(2.230)	β_2 = 0.262
^{40}Ca	0^+ (g.s), 3^-(3.736)	β_3 = 0.359
^{51}V	$\frac{7}{2}^-$ (g.s), $\frac{3}{2}^-$(0.982)	β_2 = 0.157
^{52}Cr	0^+ (g.s), 2^+(1.434)	β_2 = 0.223
^{54}Fe	0^+ (g.s), 2^+(1.408)	β_2 = 0.176
^{56}Fe	0^+ (g.s), 2^+(0.846), 4^+(3.122)	β_2=0.243
^{58}Ni	0^+ (g.s), 2^+(1.454)	β_2 = 0.172
^{60}Ni	0^+ (g.s), 2^+(1.332)	β_2 = 0.192
^{63}Cu	$\frac{3}{2}^-$ (g.s), $\frac{7}{2}^-$(1.327)	β_2 = 0.231
^{65}Cu	$\frac{3}{2}^-$ (g.s), $\frac{7}{2}^-$(1.481)	β_2 = 0.228
^{76}Se	0^+ (g.s), 2^+(0.559)	β_2 = 0.256
^{80}Se	0^+ (g.s), 2^+(0.666)	β_2 = 0.230
^{90}Zr	0^+ (g.s), 2^+(2.19)	β_2 = 0.111
^{92}Zr	0^+ (g.s), 2^+(0.935)	β_2 = 0.103
^{94}Mo	0^+ (g.s), 2^+(0.871 MeV)	β_2= 0.176
^{116}Sn	0^+ (g.s), 2^+(1.293)	β_2 = 0.10252
^{118}Sn	0^+ (g.s), 2^+(1.229)	β_2 = 0.111
^{120}Sn	0^+ (g.s), 2^+(1.171)	β_2 =0.08448
^{208}Pb	0^+ (g.s), 3^-(2.615), 5^-(3.197)	β_3 =0.127, β_5= 0.06
^{238}U	0^+ (g.s), 2^+(0.045 MeV), 4^+(0.148 MeV)	β_2 =0.178 , β_4=0.06

The functional forms for the central volume and imaginary surface terms lead to the usual energy dependence as can be concluded by inspecting Fig. 1 that corresponds to neutron incident energy off ^{56}Fe. Clearly, the central potential depth $V_v(E)$ decreases with increasing incident energy, but the absorption term W_s which accounts for inelastic processes increases with energy. This behavior is anticipated as more inelastic channels become available with increasing values of E. In such a case, larger values of W_s are required to account for the increase in the flux that is removed form the elastic channel. It is also worth noting that to improve the description of the experimental data for ^{12}C, ^{16}O we found it necessary to shift W_s down by a constant compared to all the other considered nuclei as can be seen in Eq. (22).

One way to judge the quality of the fit to a given data set is by calculating the χ^2 value, which quantifies the difference between the theoretical angular distributions and the experimental data. For a given nucleus n, the χ^2 value can be defined as:

$$\chi^2_n = \frac{\frac{W_{n,non}}{N_{n,non}}\sum_{i=1}^{N_{n,non}}\left(\frac{\sigma^{th}_{non,i}-\sigma^{exp}_{non,i}}{\Delta\sigma^{exp}_{non,i}}\right)^2 + \frac{W_{n,el}}{N_{n,el}}\sum_{i=1}^{N_{n,el}}\frac{1}{N_{n,i}}\sum_{j=1}^{N_{n,i}}\left(\frac{(\frac{d\sigma(\theta_j)_i}{d\Omega})_{\text{theo}}-(\frac{d\sigma(\theta_j)_i}{d\Omega})_{\text{exp}}}{\Delta(\frac{d\sigma(\theta_j)_i}{d\Omega})}\right)^2}{W_{n,non}+W_{n,el}}, \tag{23}$$

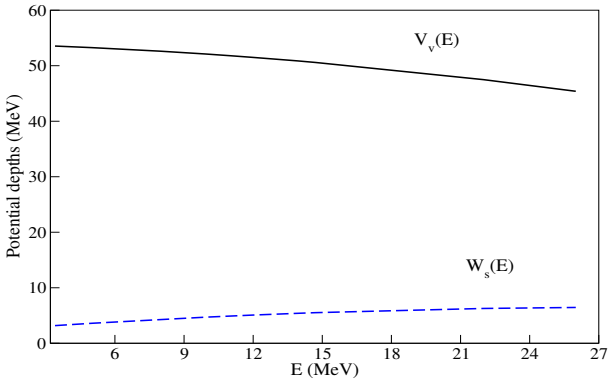

Figure 1. (Color online) Plots of the volume and surface absorption depths as a function of incident energy, see Eq. (22), corresponding to neutron scattering from ^{56}Fe.

where $(\frac{d\sigma(\theta_j)_i}{d\Omega})_{\text{theo}}$ and $(\frac{d\sigma(\theta_j)_i}{d\Omega})_{\text{exp}}$ are the calculated and measured angular distributions corresponding to the j^{th} angular momentum quantum number with the i^{th} incident energy. The subscripts 'el' and 'non' correspond to the elastic and nonelastic angular distribution data sets respectively. In addition, $(\Delta\frac{d\sigma(\theta_j)_i}{d\Omega})$ is the corresponding error on the experimental data, $N_{n,i}$ is the number of experimental data points for the n^{th} nucleus at the i^{th} incident energy. Furthermore, $N_{n,el}$ and $N_{n,non}$ are the numbers of elastic and nonelastic scattering cross section data points for the n^{th} nucleus, while $\sigma^{th}_{non,i}$ and $\sigma^{exp}_{non,i}$ are the calculated and measured nonelastic differential cross sections at the i^{th} incident energy, respectively, and $\Delta\sigma^{exp}_{non,i}$ is the corresponding error on experimental data. Finally, $W_{n,el}$ and $W_{n,non}$ are the weights of the elastic and nonelastic cross sections respectively. In addition, in this work, all the experimental data are assumed to be equally reliable. Equation (22) gives our best-fit global neutron-nucleus potential parameters, that we determined by minimizing the global value χ^2_{global} which is defined as:

$$\chi^2_{global} = \frac{1}{N}\sum_{n=1}^{N}\chi^2_n, \tag{24}$$

where $N = 25$ is the number of the target nuclei shown in Table 1.

Table 2. The χ^2_n values calculated using Eq. (23) for the shown nuclei and the global χ^2_{global} value as defined in Eq. (24) corresponding to our global potential set of parameters given in Eq. (22).

Nucleus	χ^2_n	Nucleus	χ^2_n	Nucleus	χ^2_n
^{6}Li	8.8	^{54}Fe	22.4	^{92}Zr	103
^{12}C	20.7	^{56}Fe	22.2	^{94}Mo	66
^{16}O	12.8	^{58}Ni	30.3	^{116}Sn	7
^{24}Mg	9.5	^{60}Ni	22.3	^{118}Sn	27
^{28}Si	27	^{63}Cu	5	^{120}Sn	12
^{32}S	28	^{65}Cu	3.5	^{208}Pb	30
^{40}Ca	90	^{76}Se	18.8	^{238}U	25
^{51}V	16	^{80}Se	63		
^{52}Cr	9.2	^{90}Zr	23.2		
χ^2_{global}			28.2		

4. RESULTS AND DISCUSSION

In this work, we have used the coupled - channels formalism to obtain an optical potential optimized set of parameters corresponding to neutron scattering from medium and heavy nuclei. We examined the applicability of the model to the case of light nuclei. The experimental elastic and inelastic differential cross section data are obtained from the Experimental Nuclear Reaction Data (EXFORE) [35] and the Computer Index of Nuclear Reaction Data (CINDA) [36]. As we mentioned earlier, for the nuclei considered in this work, all the inelastic angular distribution data in the relevant nuclear data libraries exist for incident neutron energies below 30 MeV, and has been fully used in this work. The only exception is for neutron inelastic scattering from ^{12}C at 94.8 MeV. Therefore, we limited our incident energy range to 100 keV $< E <$ 30 MeV.

Using the SFRESCO code, we simultaneously predicted the elastic and inelastic angular distributions by using our model parameters given in Eqs. (22) for incident neutron energies in the range 10 MeV $\leq E \leq$ 30 MeV. For permanently deformed nuclei, the non-diagonal part of the optical potential couples the ground state to the inelastic excited states

[20]. Consequently, we included the deformation parameters in the fitting the experimental data of the coupled channels differential cross sections for collective excitation. Our obtained best-fit values are shown in Table 1 together with the coupled excitation levels. Below 10 MeV, we used the TALYS code with our potential parameters given in Eq. (22) to predict the experimental data as TALYS uses the Hauser - Feshbach theory [28] to account for compound nucleus formation. To simplify the presentation we divide this section into two parts; the first deals with the results of the intermediate and heavy nuclei and the second part deals with extending our model to the case of light nuclei.

4.1. Medium and heavy nuclei

Unlike light nuclei, in this section we consider coupling the elastic channel to one and two excited states simultaneously for medium and heavy nuclei have skin thickness regions that form small part of the nuclear volume. Therefore, surface effects which usually result in potential parameters that show large energy dependence are expected to play a reduced role. For $24 \leq A \leq 238$, a volume imaginary part $W_v(E)$, as given in Eq. (22), resulted in a marked improvement in the overall agreement between the predictions of our model and the experimental data. In particular, it improved the predictions of the first elastic angular distribution minima especially for ^{54,56}Fe target nucleus. The volume term was also found important in improving the elastic angular distribution fits corresponding to neutron scattering from ^{208}Pb [38].

Coupling the elastic to inelastic channels for the medium from ^{24}Mg to ^{65}Cu nuclei

Here, For ^{24}Mg, the 0^+ ground state is coupled to the 2^+ (1.368 MeV) inelastic channel, For ^{28}Si the 0^+ ground state is coupled to the $2^+(1.779)$, $4^+(4.617$ MeV), and 3^- (6.878 MeV) inelastic channels, For ^{32}S the 0^+ ground state is coupled to the $2^+(2.230$ MeV), and 3^- (5.010 MeV) inelastic channels, For ^{40}Ca the 0^+ ground state is coupled to the $3^-(3.736$ MeV) inelastic channel. For ^{51}V the $7/2^-$ ground state is coupled to the $3/2^-(0.982$ MeV) inelastic channel. For ^{52}Cr the 0^+ ground state is coupled to the $2^+(1.434$ MeV) inelastic channel.

Our predictions for the elastic and inelastic differential cross sections are in very good agreement with the measured data as can be seen in Figs. 2 to 3. We have considered even - even and odd A target nuclei. Depending on the availability of the inelastic scattering data we have coupled the ground state to one, two and three inelastic excited channels. For low incident neutron energies, we found the vibrational model to result in a slightly better agreement with experiment than the rotational model. Also, For ^{54}Fe, the 0^+ ground state is coupled to the 2^+ (1.408 MeV) inelastic channel, For ^{56}Fe the 0^+ ground state is coupled to the $2^+(0.846)$, $4^+(3.122$ MeV), and $3^-(4.51$ MeV) inelastic channels, For ^{58}Ni, the 0^+ ground state is coupled to the $2^+(1.454$ MeV) inelastic channel, For ^{60}Ni, the 0^+ ground state is coupled to the $2^+(1.333$ MeV), and 3^- (4.039 MeV) inelastic channels For ^{63}Cu the $3/2^-$ ground state is coupled to the $7/2^-(1.327$ MeV) inelastic channel, For ^{65}Cu the $3/2^-$ ground state is coupled to the $7/2^-(1.481$ MeV) inelastic channel, Inspection of Figs. 4-9 shows that the predicted angular distributions are in very good agreement with experiment. We particularly note that the predictions of the first-order diffraction minima for ^{54}Fe and ^{56}Fe were significantly improved by introducing a volume imaginary term as given in Eq. (22). In addition, since experimental polarization data is available, we used the optimized optical potential parameters to calculate the analyzing power. As can be seen in Figs. 7 and 8 for ^{54}Fe and ^{58}Ni the theoretical predictions are in very good agreement with the data.

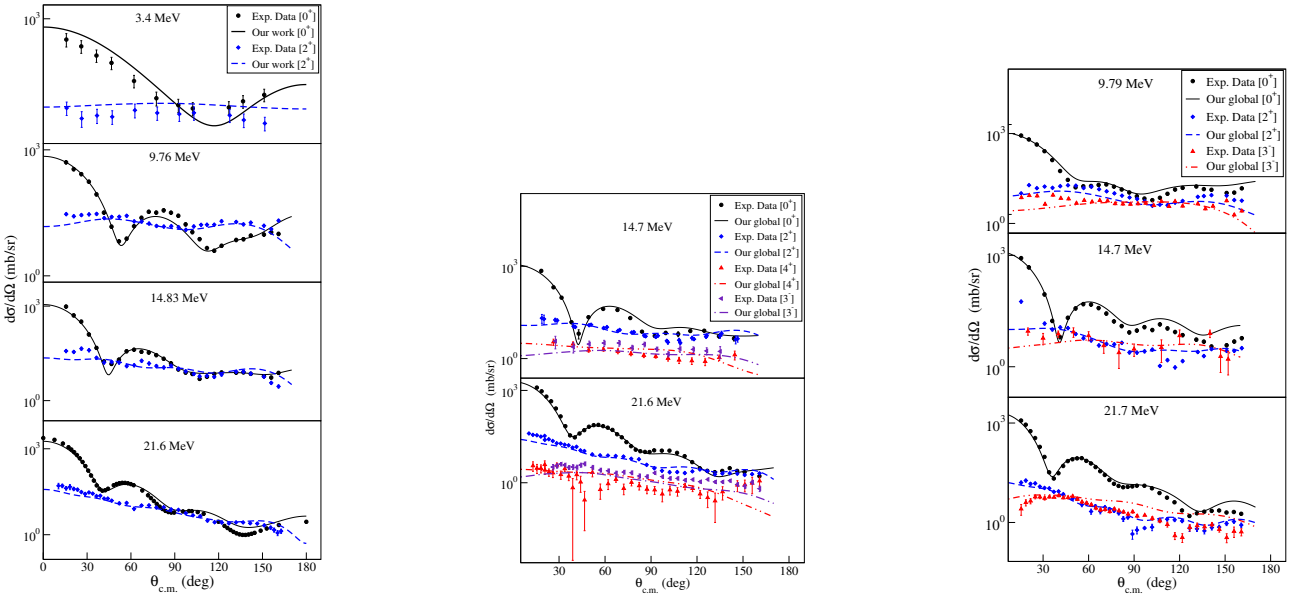

Figure 2. (Color online)Comparison between experimental angular distributions and results of OMP calculations with coupled channles computations for neutron elastic and inelastic scattering from ^{24}Mg (left), ^{28}Si (middle), and ^{32}S (right).

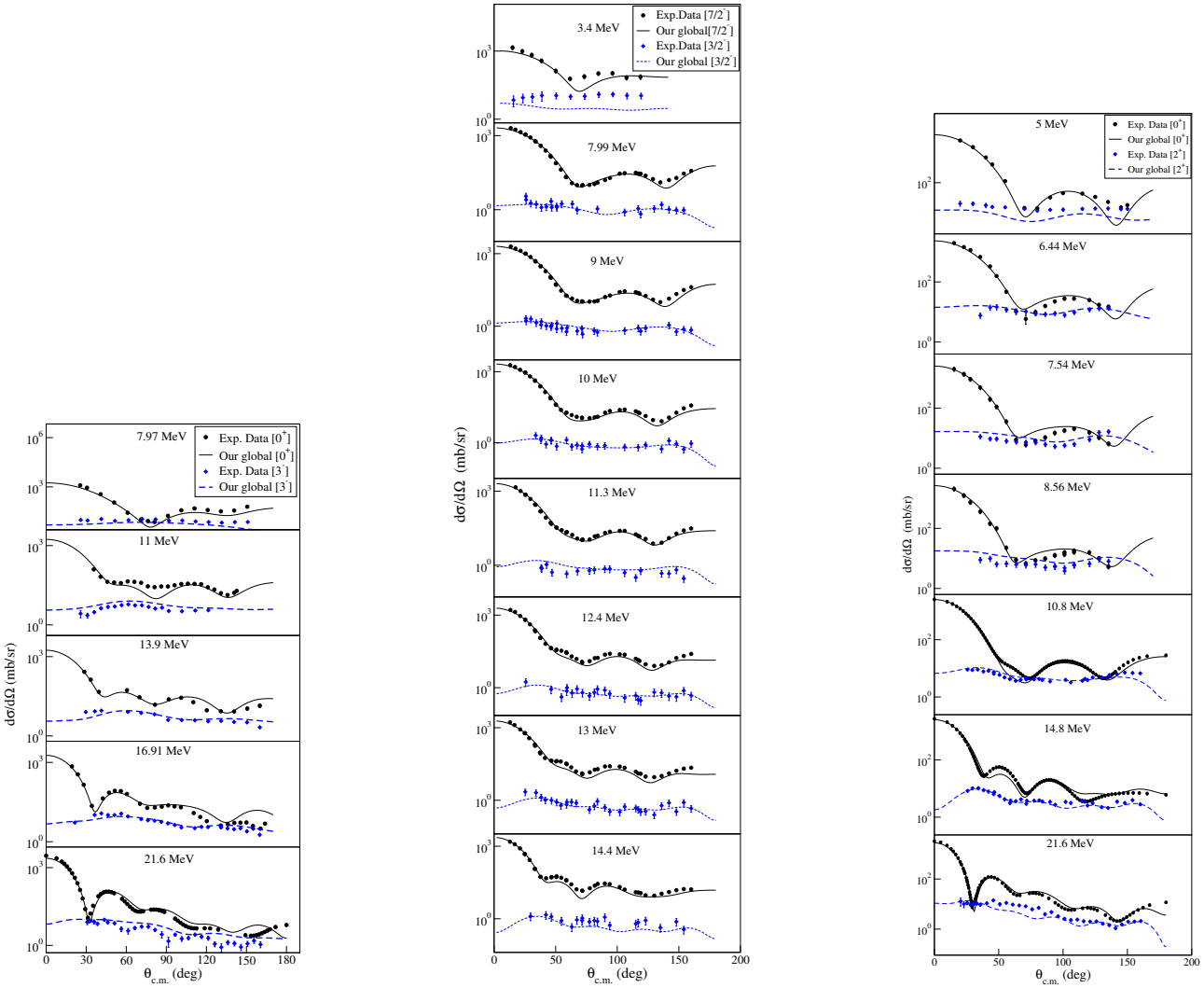

Figure 3. (Color online) Comparison between experimental angular distributions and results of OMP calculations with coupled channles computations for neutron elastic and inelastic scattering from ^{40}Ca (left), ^{51}V (middle), and ^{52}Cr (right).
.

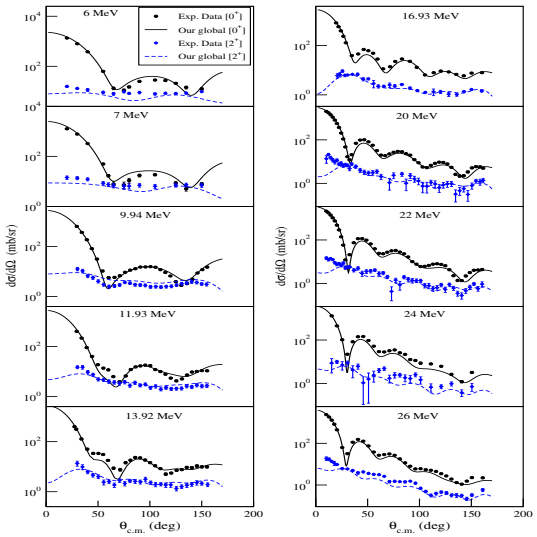

Figure 4. (Color online) Comparison between experimental angular distributions and results of OMP calculations with coupled channles computations for neutron elastic and inelastic scattering from ^{54}Fe.

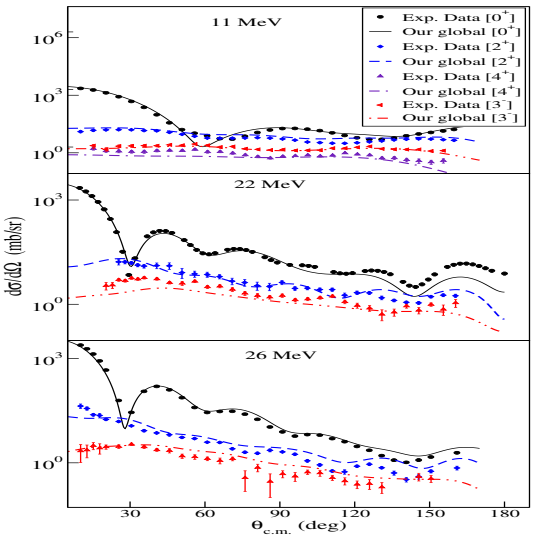

Figure 5. (Color online) Comparison between experimental angular distributions and results of OMP calculations with coupled channles computations for neutron elastic and inelastic scattering from ^{56}Fe.

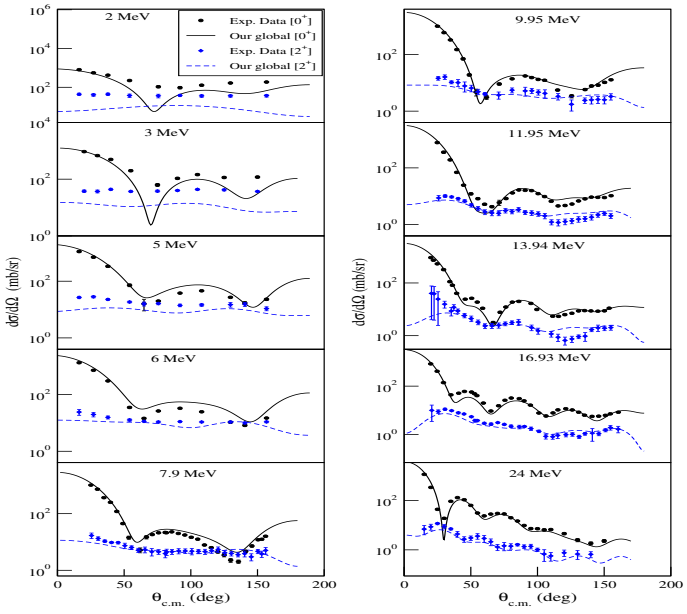

Figure 6. (Color online) Comparison between experimental angular distributions and results of OMP calculations with coupled channles computations for neutron elastic and inelastic scattering from ^{58}Ni.

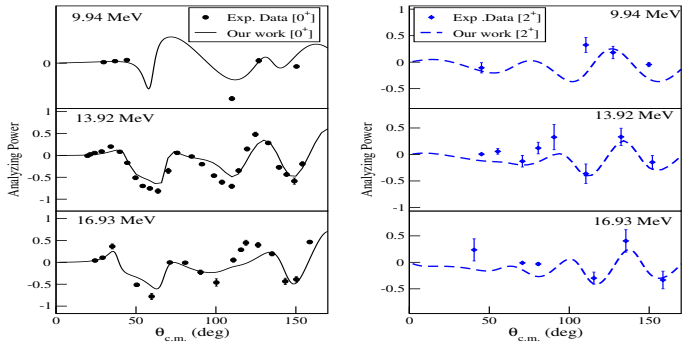

Figure 7. (Color online) Comparison of the theoretical predictions for the analyzing power with experimental data for ^{54}Fe$(n,n)^{54}$Fe*.

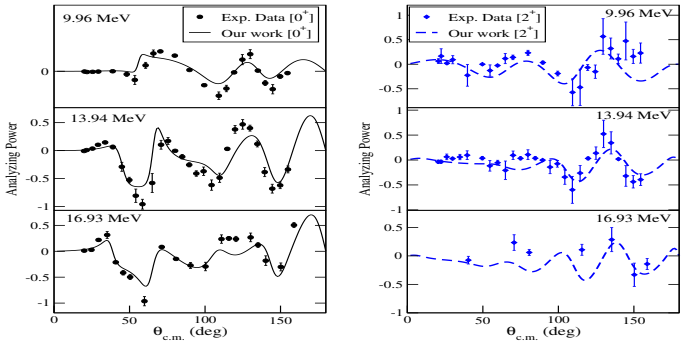

Figure 8. (Color online) Comparison of the theoretical predictions for the analyzing power with experimental data for ^{58}Ni$(n,n)^{58}$Ni*.

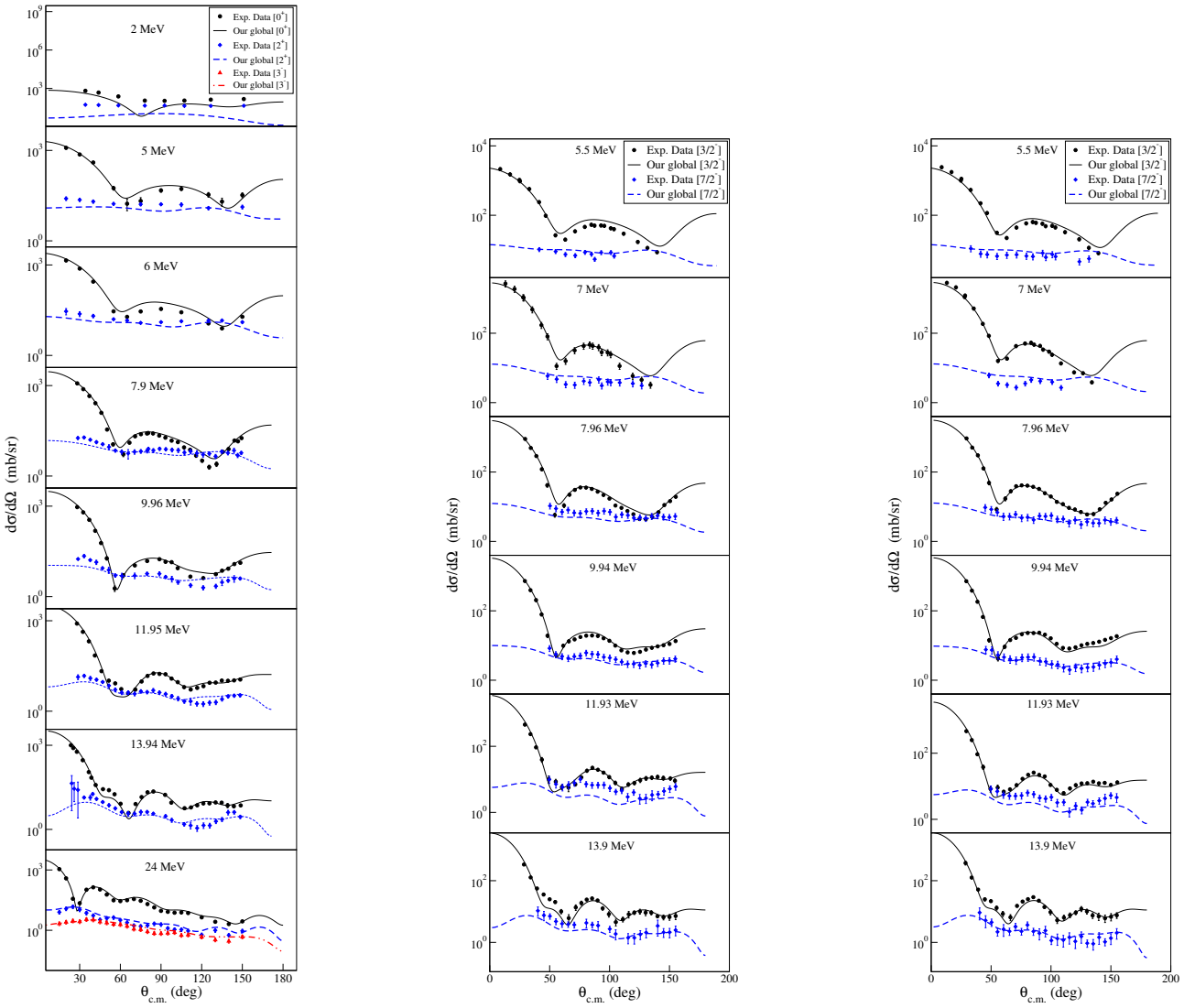

Figure 9. (Color online) Comparison between experimental angular distributions and results of OMP calculations with coupled channles computations for neutron elastic and inelastic scattering from ^{60}Ni (left), ^{63}Cu (middle), and ^{65}Cu (right).

Coupling the elastic to inelastic channels for the heavy from ^{76}Se to ^{238}U nuclei

In this section, for ^{76}Se, the 0^+ ground state is coupled to the 2^+ (0.559 MeV) inelastic channel, For ^{80}Se the 0^+ ground state is coupled to the 2^+(0.666) MeV inelastic channel, For ^{90}Zr the 0^+ ground state is coupled to the 2^+(2.19 MeV) inelastic channel, For ^{92}Zr the 0^+ ground state is coupled to the 2^+(0.935 MeV) inelastic channel, For ^{94}Mo the 0^+ ground

state is coupled to the 2^+(0.871 MeV) inelastic channel. As for the previous nuclei, our theoretically calculated angular distributions for neutron scattering off ^{76}Se, ^{80}Se, ^{90}Zr, ^{92}Zr, and ^{94}Mo nuclei are in good agreement with experimental data as can be seen in Figs. 10 - 11. Also, For ^{116,118,120}Sn, the 0^+ ground state is coupled to the 2^+ (1.293, 1.229, 1.171 MeV), and 3^- (2.266, 2.324, 2.400 MeV) inelastic channels respectively, For ^{208}Pb the 0^+ ground state is coupled to the 3^-(2.615) MeV, 5^-(3.197 MeV) inelastic channels, For ^{238}U the 0^+ ground state is coupled to the 2^+(0.045 MeV), and 4^+ (0.148 MeV) inelastic channels, Inspection of Figs. 12-13 shows that our predicted angular distributions for neutron scattering off ^{116,118,120}Sn, ^{208}Pb and ^{238}U nuclei are in good agreement with experiment.

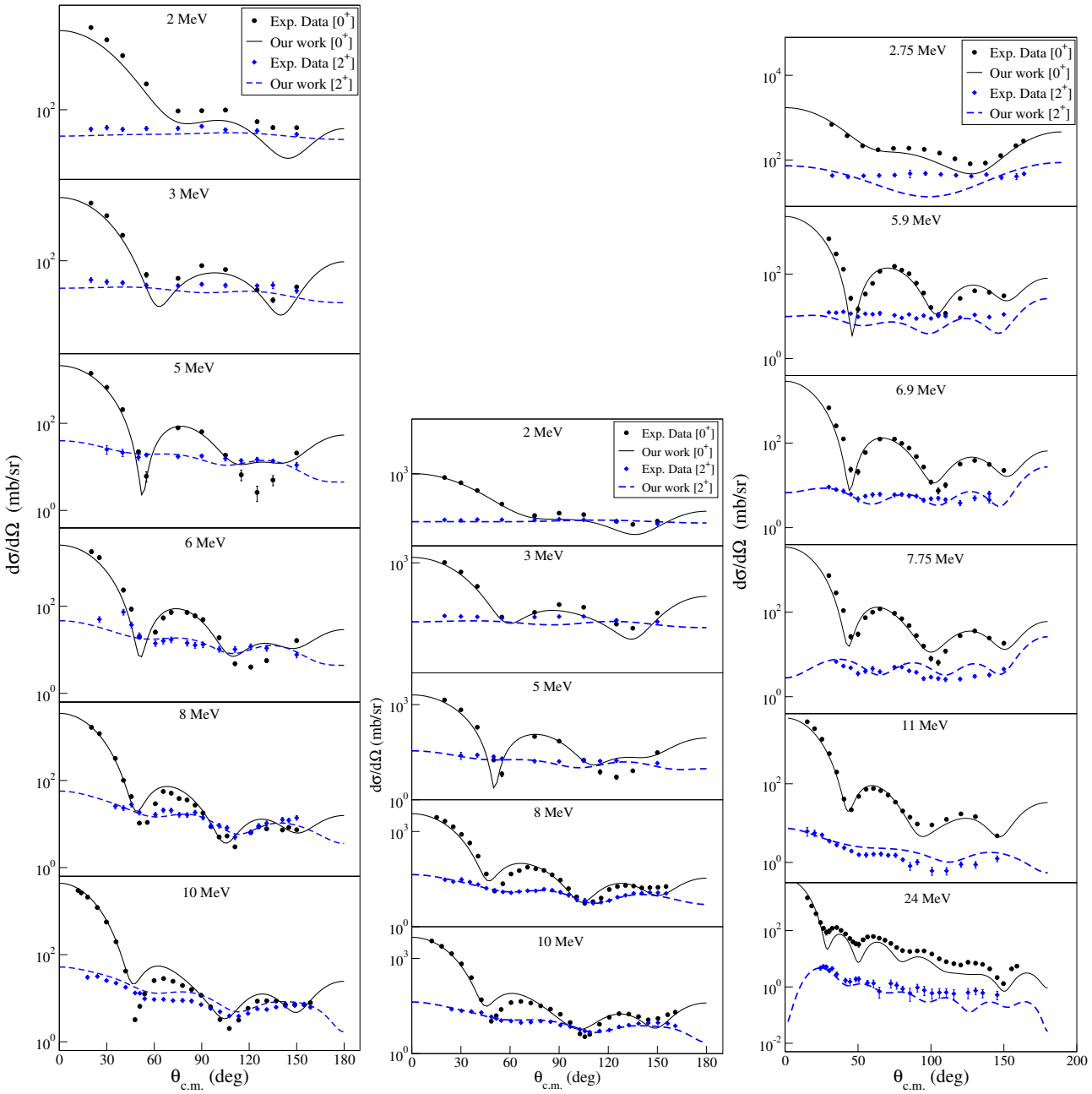

Figure 10. (Color online) Comparison between experimental angular distributions and results of OMP calculations with coupled channles computations for neutron elastic and inelastic scattering from ^{76}Se (left), ^{80}Se (middle) , and ^{90}Zr (right).

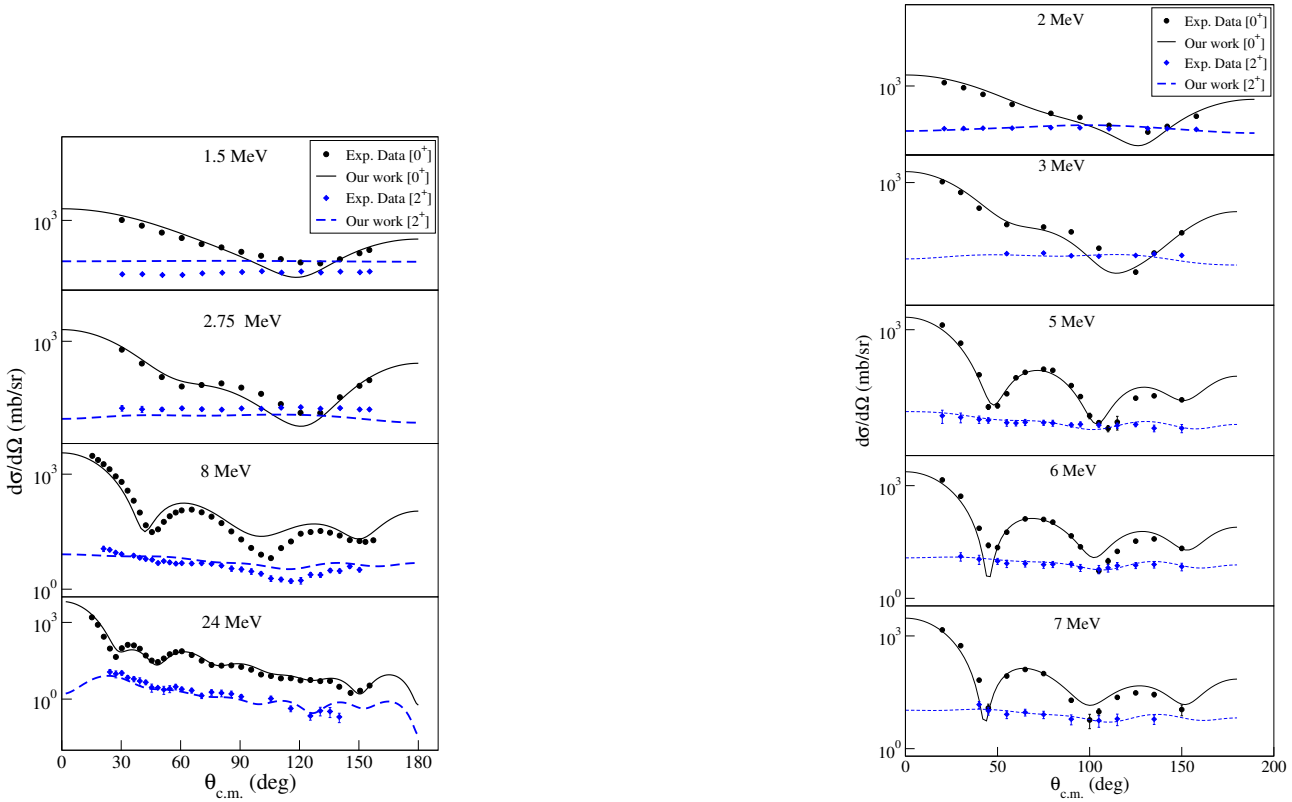

Figure 11. (Color online) Comparison between experimental angular distributions and results of OMP calculations with coupled channles computations for neutron elastic and inelastic scattering from ^{92}Zr (left) and ^{94}Mo (right).

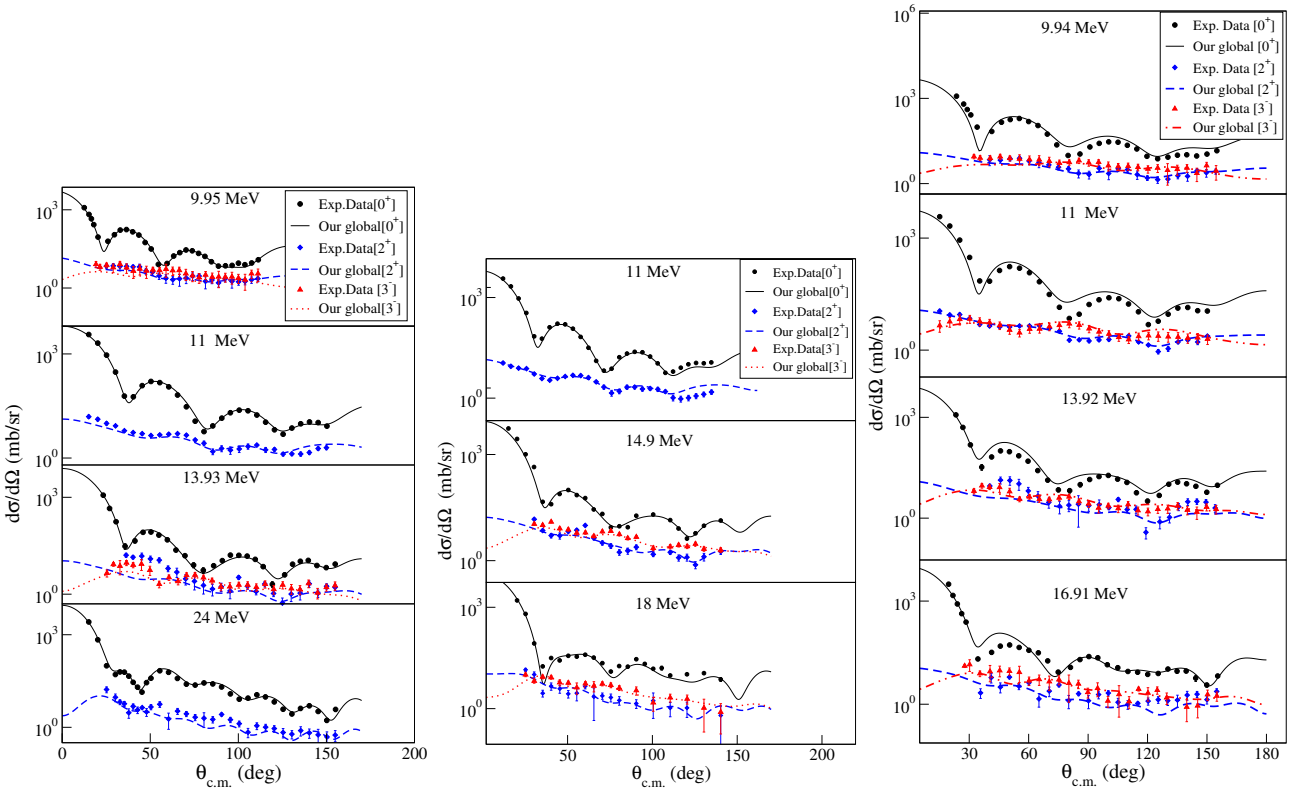

Figure 12. (Color online) Comparison between experimental angular distributions and results of OMP calculations with coupled channles computations for neutron elastic and inelastic scattering from ^{116}Sn (left) , ^{118}Sn (middle), and ^{120}Sn (right).

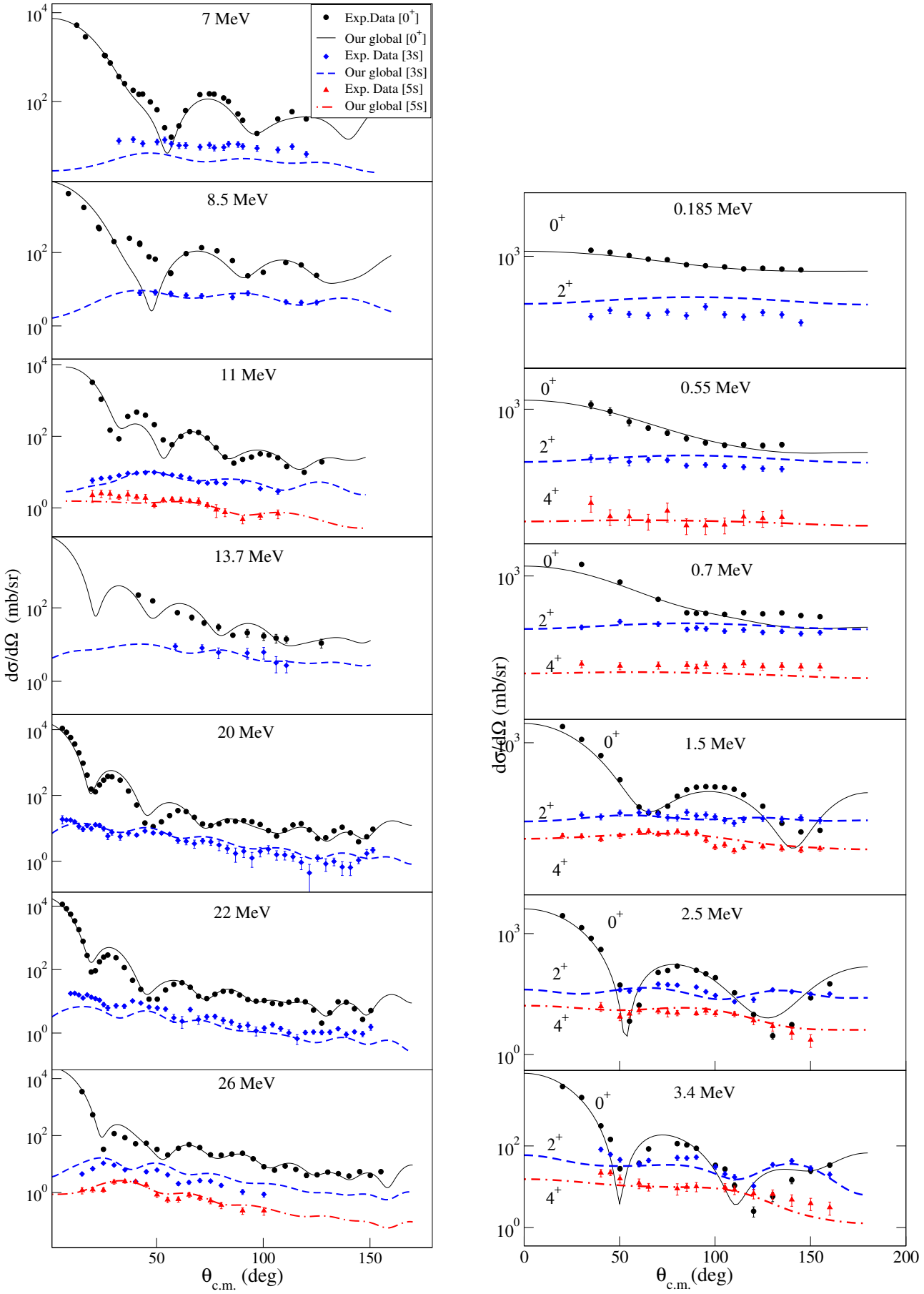

Figure 13. (Color online) Comparison between experimental angular distributions and results of OMP calculations with coupled channles computations for neutron elastic and inelastic scattering from ^{208}Pb (left) and ^{238}U (right).

4.2. Extending the model to the case of light nuclei

In this section we test the applicability of our model to the light ^{6}Li, ^{12}C and ^{16}O target nuclei, which differ from the intermediate and heavy ones in that the surface region makes up a large portion of the nuclear volume. For the $n - ^{6}$ Li scattering process, inelastic angular distribution data are available only for coupling the 1^{+} ground state to the 3^{+} (2.186 MeV) excited state. also we shall consider coupling the 0^{+} ground state of ^{12}C to the 2^{+} (4.438 MeV) and 3^{-} (9.641 MeV) excited states simultaneously. Similarly, the 0^{+} ground state of the ^{16}O nucleus is simultaneously coupled to the 3^{-} (6.129 MeV) and 2^{+} (6.917 MeV) excited states. This results in structural effects in the angular distributions that are manifested as prominent minima in the elastic angular distributions, particularly, at large scattering angles. This has always resulted in difficulties in predicting the experimental data even when developing local optical potentials [11] - [16]. As can be seen in Eq. (22), the smooth functional forms corresponding to ^{6}Li are the same as those for the intermediate nuclei. However, for ^{12}C and ^{16}O best predictions could only be obtained by shifting the imaginary surface absorption term by a constant compared to the rest of the nuclei considered in this work as displayed in Eq. (22). Despite the difficulties encountered when dealing with light nuclei, and taking into account that the spin - orbit depths and all the geometrical parameters are fixed, figures 14 - 15 show that our predictions for the angular distributions, particularly the elastic ones, are in very good overall agreement with the experimental data.

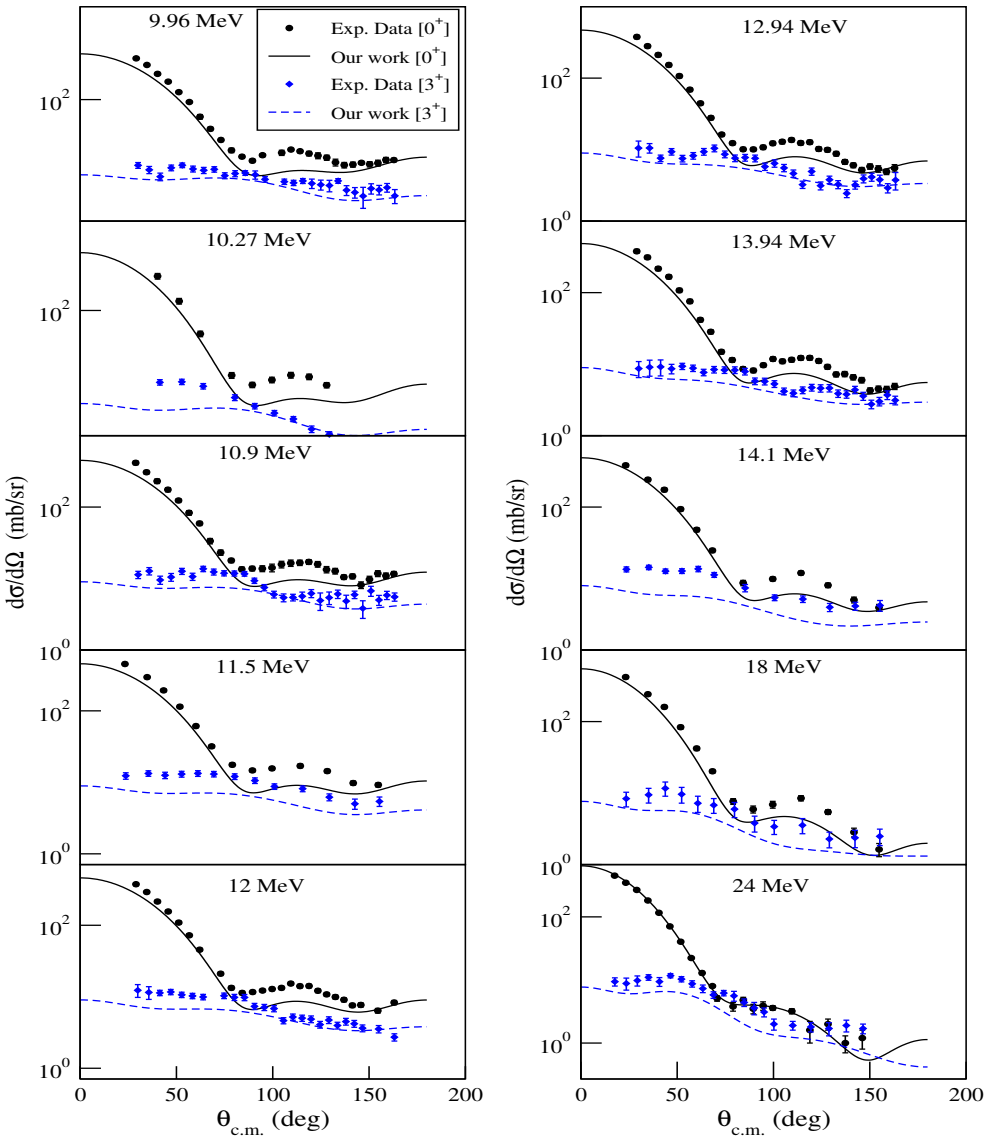

Figure 14. (Color online) Comparison between experimental angular distributions and results of OMP calculations with coupled channles computations for neutron elastic and inelastic scattering from ^{6}Li.

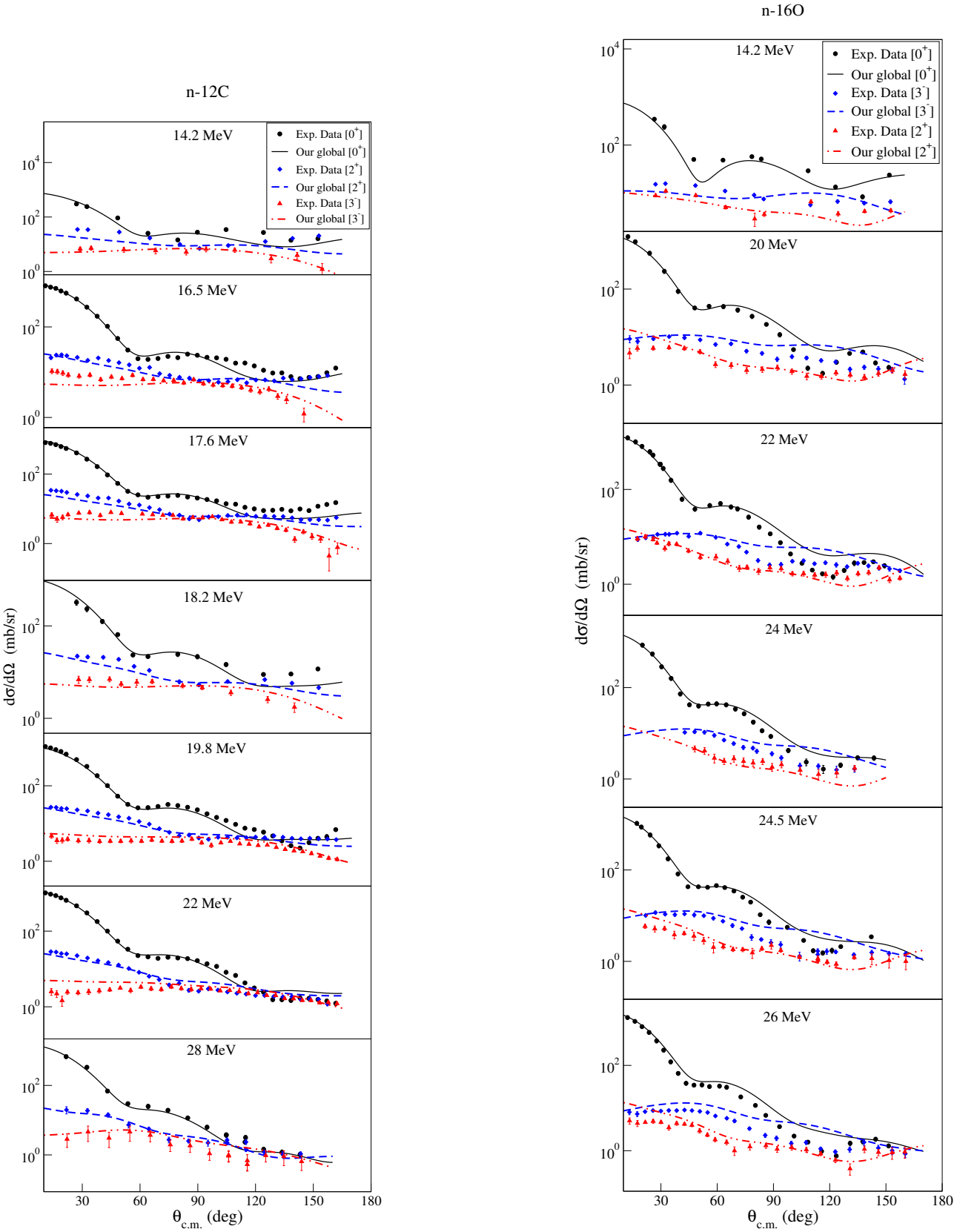

Figure 15. (Color online) Comparison between experimental angular distributions and results of OMP calculations with coupled channles computations for neutron elastic and inelastic scattering from ^{12}C (left) and ^{16}O (right).

5. TOTAL CROSS SECTIONS

In Figs. 16 and 17 we compare our predictions for the total and total elastic cross sections with the experimental values. For the medium and heavy nuclei, our theoretical predictions for the cross sections are in good overall agreement with the data. In general, the agreement becomes progressively better with increasing mass number of the target nucleus. It is also worth noting that the introduction of a volume imaginary term $W_v(E)$ for the nuclei $6 \leq A \leq 238$, as given in Eq. (22), significantly improved our predictions. The attempt to include light nuclei in our analysis has been more successful in predicting the angular distributions than predicting the total cross sections. For the light ^{6}Li nucleus, the agreement between the theoretical and experimental values is better at energies above 10 MeV as can be seen in Fig. 16. A similar behavior was also observed for the ^{12}C and ^{16}O nuclei. As we mentioned above, this could be a consequence of structural effects that play an important role in the nucleon scattering process from such light nuclei [21] and [37]. In fact, in an earlier work, we developed local optical potential fits where all the potential parameters were allowed to vary with energy and target mass number. The calculated total and total elastic cross sections for carbon and oxygen still showed some discrepancy with experimental data [21]. Clearly, our attempted case of developing smooth functional forms for the potential depths, keeping the geometrical parameters and spin -orbit term fixed is even more difficult. This difficulty is confirmed by noting that the differential cross section for nucleon elastic scattering from ^{16}O shows a minimum around 120^{0} which could not be fitted despite many attempts using local and microscopic optical potentials [39]. Finally, the measured data were taken from the Evaluated Nuclear Data File [ENDF] except the values of the total cross sections for ^{6}Li and ^{12}C which were obtained from [EXFOR].

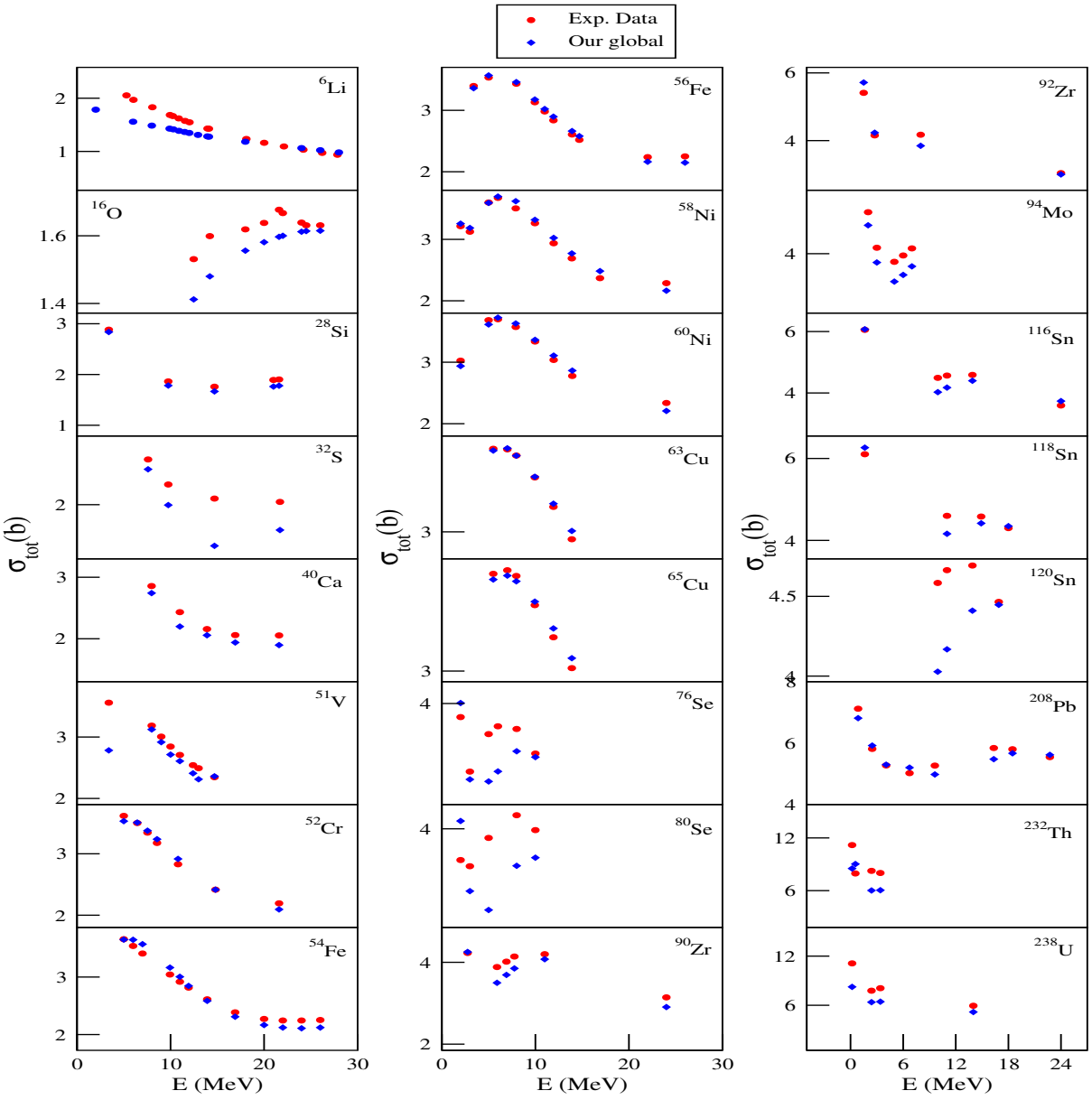

Figure 16. (Color online) Comparison of predicted neutron total cross sections and experimental data from ^{6}Li to ^{238}U.

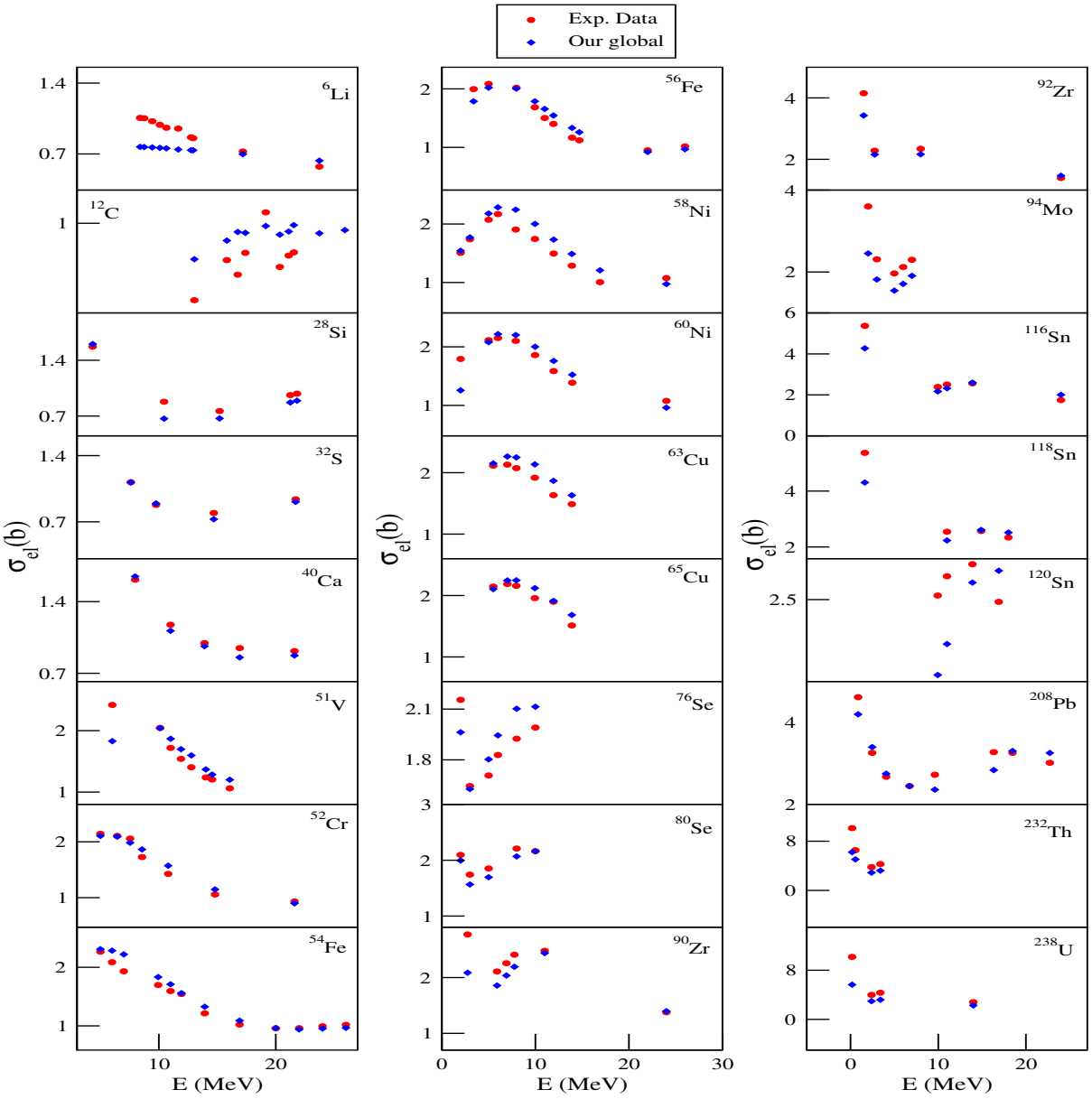

Figure 17. (Color online) Comparison of predicted neutron elastic cross sections and experimental data from ^{6}Li to ^{238}U.

6. CONCLUSIONS

In this work we investigated neutron scattering from medium and heavy nuclei using an optical model with channel coupling. We also tested the applicability of our model to the case of light nuclei. Therefore, we considered nuclear targets from ^{6}Li to ^{238}U and incident neutron energies in the range 180 keV $< E <$ 30 MeV. No higher energies were investigated as there are no experimental inelastic angular distribution data for the nuclei studied in this work. We obtained smooth functional forms for the real volume, imaginary volume and the imaginary surface depths as functions of energy, mass number and the neutron - proton asymmetry of the target nucleus as given in Eq. (22).

Using our optimized set of parameters, we simultaneously predicted the elastic and inelastic angular distribution data. As can be seen in Figs. 2 to 9 and 10 to 13, for the intermediate and heavy nuclei, our calculated values are in very good overall agreement with the experimental data. The predicted polarization data are also in very good agreement with the experimental values as can be seen in Figs. 7 and 8. Our model has also been extended to predict the elastic and inelastic angular distributions for the light ^{6}Li, ^{12}C and ^{16}O nuclei which, unlike intermediate and heavy nuclei, have diffuse edges and less uniform matter distributions that complicate the process of predicting the experimental data. Despite this, The calculated angular distributions show a very reasonable overall agreement with the experimental data as can be seen by inspecting Figs. 14 to 15.

In addition, we calculated total and total elastic cross sections. Our theoretical predictions are in good agreement with the corresponding experimental values particularly for the intermediate and heavy nuclei. This agreement becomes

increasingly better with increasing mass number of the target nucleus. In fact, the introduction of (i) an imaginary volume term W_v for the nuclei with mass numbers $6 \leq A \leq 238$ and (ii) shifting the imaginary surface term by a constant for light nuclei, as can be seen in Eq. (22), significantly improved the predicted angular distributions and total cross sections. As for the light ^{6}Li, ^{12}C and ^{16}O nuclei, our calculations show better agreement for incident energies above 10 MeV. The discrepancy below 10 MeV incident energy could be a result of structural effects playing an important role in the scattering process [21] and [37]. For light nuclei, our model has been more successful in predicting the elastic and inelastic angular distributions than total cross sections.

ORCID

Waleed Saleh Alrayashi, https://orcid.org/0009-0009-6440-8332

REFERENCES

[1] H. Feshbach, Ann. of Phys. **5**, 357 (1958). https://doi.org/10.1016/0003-4916(58)90007-1

[2] A.J. Koning, and J.P. Delaroche, Nucl. Phys. A, **713**, 231 (2003). https://doi.org/10.1016/S0375-9474(02)01321-0

[3] Y. Han, Y. Xu, H. Liang, H. Guo, and Q. Shen, Phys.Rev. C, **81**, 024616 (2010).https://doi.org/10.1103/PhysRevC.81.024616

[4] S. Kunieda, S. Chiba, K. shibata, A. Ichihara, and E.Sh. Sukhovitski, Journal of nuclear science and technology, **44**(6), 838 (2007). https://doi.org/10.1080/18811248.2007.9711321

[5] I.J.Thompson, and F.M. Nunes, *Nuclear reactions for Astrophysics*, (Cambridge University Press, 2009).

[6] G. Racah, Phys. Rev. **62**, 438 (1942). https://doi.org/10.1103/PhysRev.62.438

[7] J.M. Eisenberg, and W. Greiner, *Nuclear Models*, Vol. 1, Ch. 2, (North-Holland, 1970).

[8] A. Saleh, and M.I. Jaghoub, Phys. Rev. C, **109**, 034606 (2024). https://doi.org/10.1103/PhysRevC.109.034606

[9] A. Albelleh, M.I. Jaghoub, and W.S. Al-Rayashi, Nucl. Phys. A, **1024** , 122461 (2022). https://doi.org/10.1016/j.nuclphysa.2022.122461

[10] S. Alameer, M.I. Jaghoub, and I, Ghabar, J. Phys. G: Nucl. Part. Phys. **49**, 015106 (2022). https://doi.org/10.1088/1361-6471/ac38c2

[11] I.N. Ghabar, and M.I. Jaghoub, Phys. Rev. C, **91**, 064308 (2015). https://doi.org/10.1103/PhysRevC.91.064308

[12] M. Utoom, M.I. Jaghoub, and T. Aqel, Can. J. Phys. **100** , 015106 (2022). https://doi.org/10.1139/cjp-2021-0380

[13] T. Aqel, M.I. Jaghoub, Eur. Phys. J. A, **56**, 216 (2020). https://doi.org/10.1140/epja/s10050-020-00226-5

[14] T. Aqel, M.I. Jaghoub, Nucl. Phys. A, **989**, 145 (2019). https://doi.org/10.1016/j.nuclphysa.2019.06.005

[15] M.I. Jaghoub, A.E. Lovell, and F.M. Nunes, Phys. Rev. C, **98**, 024609 (2018). http://dx.doi.org/10.1103/PhysRevC.98.024609

[16] J. Klug, J. Blomgren, A. Atac, B. Bergenwall, A. Hildebrand, C. Johansson, P. Mermod, *et al.*, Phys. Rev. C, **68**, 064605 (2003). https://doi.org/10.1103/PhysRevC.68.064605

[17] H. An, and C. Cai, Phys. Rev. C, **73**, 054605 (2006). https://doi.org/10.1103/PhysRevC.73.054605

[18] A. Bohr, and B.R. Mottelson, Kgl. Danske Videnskab. Selskab, Mat. Fys. Medd. **27**(16), (1953). https://cds.cern.ch/record/213298/files/p1.pdf

[19] D.M. Chase, L. Wilets, and A.R. Edmonds, Rotational-Optical Model For Scattering of Neutrons Phys. Rev. **110**, 1080 (1985). https://doi.org/10.1103/PhysRev.110.1080

[20] T. Tamura, Rev. Mod. Phys. **37**, 679 (1965). https://doi.org/10.1103/RevModPhys.37.679

[21] W.S. Al-Rayashi, and M.I. Jaghoub, Phys. Rev. C, **93**, 064311 (2016). https://doi.org/10.1103/PhysRevC.93.064311

[22] B. Buck, Phys. Rev. **130**, 712 (1963). https://doi.org/10.1103/PhysRev.130.712

[23] M.P. Fricke, E.E. Gross, B.J. Mortgn, and A. Zucker, Phys. Rev. **156**, 1207 (1967). https://doi.org/10.1103/PhysRev.156.1207

[24] S. Chiba, K. Shibata, A. Ichihara, and F.Sh. Sukhovitsi $\tilde{i}$, Journal of nuclear sciences and technology, **44**(6), 838 (2007). https://doi.org/10.1080/18811248.2007.9711321

[25] G. Haouat, Ch. Lagrange, R. de Swiniarski, F. Dietrich, J.P. Delaroche, and Y. Patin, Phys. Rev C, **30**, 1795 (1984). https://doi.org/10.1103/PhysRevC.30.1795

[26] I.J. Thompson, Coupled Reaction Channels Calculations in Nuclear Physics, Computer Physics Reports, **7**, 167 (1988). https://doi.org/10.1016/0167-7977(88)90005-6

[27] A.J. Koning, S. Hilaire, and M.C. Duijvestijn, "TALYS-1.0", in: *Proceedings of the International Conference on Nuclear Data for Science and Technology*, edited by O. Bersillon, F. Gunsing, E. Bauge, R. Jacqmin, and S.Leray, (EDP Sciences, Nice, France, 2008), pp. 211-214. https://doi.org/10.1051/ndata:07767

[28] W. Hauser, and H. Feshbach, Phys. Rev. **87**, 366 (1952). https://doi.org/10.1103/PhysRev.87.366

[29] S. Cwiok, J. Dudek, W. Nazarewicz, J. Skalski, and V. Werner, Comput. Phys. Commun. **46**, 379 (1987). https://doi.org/10.1016/0010-4655(87)90093-2

[30] G.M. Crawley, and G.T. Garvey, Phys. Rev. **160**, 981 (1967). https://doi.org/10.1103/PhysRev.160.981

[31] S. Raman, C.W. Nestor, Jr.S. Kahane, and K.H. Bhatt, Phys. Rev. C, **43**, 556 (1991). https://doi.org/10.1103/PhysRevC.43.556

[32] L. Grodzins, Phys. Lett. **2**, 88 (1962). https://doi.org/10.1016/0031-9163(62)90162-2

[33] M.P. Fricke, and G.R. Satchler, Phys. Rev. **139**, B567 (1965). https://doi.org/10.1103/PhysRev.139.B567

[34] R.A. Zureikat, and M.I. Jaghoub, Nucl. Phys. A, **916**, 183 (2013). https://doi.org/10.1016/j.nuclphysa.2013.08.007

[35] EXFOR: Experimental Nuclear Reaction Data, https://www-nds.iaea.org/exfor/exfor.htm

[36] CINDA: Computer Index of Nuclear Reaction Data https://www-nds.iaea.org/exfor/cinda.htm

[37] A. Bonaccorso, and R.J. Charity, Phys. Rev. C, **89**, 024619 (2014). https://doi.org/10.1103/PhysRevC.89.024619

[38] R.W. Finlay, J.R.M. Armand, T.S. Cheema, J. Rapaport, and F.S. Dietrich, Phys. Rev. C, **30**, 796 (1984). https://doi.org/10.1103/PhysRevC.30.796

[39] G.H. Rawitscher, and D. Lukaszek, Phys. Rev. C, **69**, 044608 (2004). https://doi.org/10.1103/PhysRevC.69.044608

ПОТЕНЦІАЛ ФЕНОМЕНОЛОГІЧНОЇ ОПТИЧНОЇ МОДЕЛІ ГЛОБАЛЬНОГО ЗВ'ЯЗАНОГО КАНАЛУ ДЛЯ НЕЙТРОННО-ЯДЕРНОГО РОЗСІЮВАННЯ ВІД ^{6}Li ДО ^{238}U

Валід Салех Алраяші

Департамент науки, факультет освіти, Університет Сани, Сана, Ємен

Вважається, що процес нейтронно-ядерного розсіювання створює гладкі функціональні форми для реальної та уявної частин феноменологічного оптичного потенціалу з використанням формалізму аналізу зв'язаних каналів. Ми розглядаємо проміжні та важкі ядерні мішені та досліджуємо можливість розширення моделі на зазвичай виключений випадок легких ядер. Використовуючи нашу модель, ми одночасно прогнозуємо пружні та непружні кутові розподіли розсіювання нейтронів від ^{6}Li до ^{238}U для різних енергій у діапазоні 100 кеВ $< E <$ 30 МеВ, для яких доступні дані про непружні кутові розподіли. Ми отримуємо гладкі форми для реальних і уявних глибин об'ємних і поверхневих потенціалів як функцій енергії, масового числа та асиметрії між числами протонів і нейтронів у ядрі-мішені. Глибини реального та уявного спін-орбітального члена та всі геометричні параметри потенціалу фіксовані. Наші прогнозовані пружні та непружні диференціальні поперечні перерізи дуже добре узгоджуються з виміряними даними. Розраховані загальні пружні, загальні поперечні перерізи та аналізуючі здібності в цілому добре узгоджуються з експериментальними значеннями, особливо для проміжних і важких ядер.

Ключові слова: *потенціал оптичної моделі; пружне розсіювання; непружне розсіювання; зв'язані канали; диференціальний переріз*

East European Journal of Physics. 2. 74–83 (2025)
DOI: 10.26565/2312-4334-2025-2-08 ISSN 2312-4334

RELATIVISTIC IMPACT ON DUST-ELECTRON-ACOUSTIC SOLITARY WAVES IN AN UNMAGNETIZED PLASMA WITH NONEXTENSIVE IONS

Rafia Khanam[*a], **Satyendra Nath Barman**[b], **Muktarul Rahman**[a]
[a] *Department of Mathematics, Gauhati University, Guwahati-781014, Assam, India*
[b] *B. Borooah College, Guwahati-781007, Assam, India*
[*] *Corresponding Author e-mail: rafiakhanam353@gmail.com*
Received July 26, 2024; revised November 12, 2024; in final form March 26, 2025; accepted March 29, 2025

The nonlinear properties of the dust-electron-acoustic (DEA) solitary waves and their propagating behaviours are theoretically studied in an unmagnetized relativistic plasma model. Such plasma is composed by the weakly relativistic electrons, nonextensive distributed ions and negatively charged immobile dust particles. Staring from a set of unidirectional fluid equations for electrons and nonextensive distribution for ions with Poisson equation, the Korteweg-de Vries (KdV) and modified KdV (mKdV) equations are determined by using the reductive perturbation method technique and their soliton solutions, thus obtained, to analyse the existence regime and basic features of small amplitude DEA solitons. The effects of physical parameters namely ion-to-electron number density ratio (δ), relativistic streaming factor (v_0/c) and ion nonextensive parameter (q) on the dynamics of solitary formations are examined in detail. The result shows the existence of both compressive and rarefactive DEA KdV solitons and only compressive DEA mKdV solitons in the range $-1 < q < 3$, with various δ and v_0/c in the plasma. Additionally, the influences of all the physical parameters on the propagation of DEA solitary waves corresponding to the KdV and mKdV equations are numerically analysed within the paper. The results of this study might help clarify the basic characteristics of nonlinear travelling waves propagating in both laboratory and space plasma as well as astrophysical plasma environments.

Keywords: *Dust-electron-acoustic solitary wave; KdV and mKdV equations; Reductive perturbation technique; q-nonextensive ions; Relativistic plasma*

PACS: 52.35.Fp, 52.35.Qz, 52.27.Lw, 52.27.Ny
MSC: 35C08, 35Q51, 35Q53

1. INTRODUCTION

One of the most interesting and fascinating laboratories of nonlinear structures in space is the study of solitary waves in plasmas. Large dust grains in space plasma have a negative charge, while small grains have a positive charge. However, the polarity of the dust grains might differ. An exceptionally low-frequency dust wave mode known as dust acoustic waves (DAW) is produced by the new time scales connected to the slower dust component (larger).

It is found that the properties of plasma waves are significantly altered by the presence of dust charged particles. One intriguing area of current research is the study of electrostatic solitary waves in dusty plasma. An intriguing field of recent work has been the study of electrostatic solitary waves in dusty plasma.

The characteristics of plasma waves are discovered to be significantly altered by the presence of dust-charged particles.

Due to field emission, it is widely known that the presence of negatively charged dust particles with micrometer or sub micrometer sizes can alter the properties of plasma waves in space. Dusty plasmas are common in a wide range of astrophysical environments, including the interstellar medium, asteroid zones, cometary tails, planetary rings, the Earth's magnetosphere, and the vicinity of stars.

It's an intriguing application to evaluate low-frequency noise enhancement seen by the Vego and Goitto space missions in the dusty area of Haley's Comet. Dust density, temperature, particle size, and charge are just a few of the characteristics of dust grains that are reflected by the Cassini plasma spectrometer instrument over Saturn's major A and B rings. A wealth of knowledge regarding dusty plasmas can also be found in interstellar clouds in space. Many researchers [1–16] have provided a wonderful explanation of the role and influence of dusty plasma in astrophysical plasma and space environments. In dissipative plasma with superthermal electrons, Hanbaly *et al.* [17] studied nonlinear electron acoustic waves. Singh and Lakhina [18] have investigated the generation of electron-acoustic waves (EAWs) in the magnetosphere. Bansal *et al.* [19] have discussed the subject of oblique modulation of electron acoustic waves in nonextensive plasma. The research paper titled Dust-electron-acoustic shock waves originating from changes in dust charge was written by Mamun [20]. The relationship between electron-acoustic solitons in the auroral zone for an electron beam plasma system has been investigated by Jahangir *et al.* [21].

The relativistic effects are currently being incorporated into the research that is being done on solitary waves in plasmas that contain several components [22–33]. There have been a multitude of papers written over the course of the past few decades, each of which has a variety of compositions that cover a wide range of topics. The generation of weakly relativistic ion acoustic solitons in magnetized plasma is facilitated by unidirectional relativistic electrons with inertia, as

Cite as: R. Khanam, S.N. Barman, M. Rahman, East Eur. J. Phys. 2, 74 (2025), https://doi.org/10.26565/2312-4334-2025-2-08

researched by Kalita and Choudhury [34]. Kalita & Kalita [35] have investigated the mild relativistic effects of electrons and the implicit role of Cairns dispersed ions in the generation of dust acoustic waves in plasma. Moreover, Kalita and Das [36] have studied in a comparative analysis of modified Korteweg-de Vries solitons and dust ion acoustic Korteweg-de Vries solitons in dusty plasmas with different temperatures.

It is commonly known that the macroscopic ergodic equilibrium state is uniformly represented by the Maxwell distribution for ions. Over the last few decades, Maxwellian particle distributions have been utilized by many researchers. However, there has been a noticeable growth in interest in nonextensive statics, also known as Tsillis statistics, which are based on the Boltzmann-Gibbs-Shannon (BGS) method for studying particle dispersion in plasma in recent years. In the field of statistics, Renyi [37] and Tsallis [38] first introduced an appropriate nonextensive generalization of the BGS entropy. In this system, the entropic index q represents the degree of non extensivity. Currently, numerous researchers are examining the number density of particle plasma in the $q-$nonextensive distribution by referencing the following sources: [39–47]. Numerous important aspects of conventional statistical mechanics are still present in nonextensive statistics. Superextensivity is defined as having a composite system's generalized entropy greater than the sum of the entropies of its constituents; subextensivity is defined as having a composite system's generalized entropy smaller than the sum of its subsystems. A generalized particle distribution known as the q distribution function is the outcome of Tsallis nonextensive statistical mechanics. When $q < -1$ and the q-nonextensive distribution cannot be normalized, it might be helpful. Once more, the distribution function reduces to the typical Maxwellian-Boltzmann velocity distribution if $q = 1$. Dai *et al.* [48] investigated in nonextensive statistics the dust ion-acoustic instability with q-distribution. Awady & Moslem [49] carried out numerical studies on a plasma that contained nonextensive electrons and positrons. Amour & Tribeche [50] conducted research on Collisionless damping of dust-acoustic waves in a dusty plasma with nonextensive ions that varies in charge. Thus, our aim is to study the formation and properties of DEA solitary waves in an ummagnetized plasma in which electrons are relativistic and ions are nonextensive, in the presence of static dusts. Small amplitude DEA solitons are studied using the reductive perturbation approach. Our results should help to understand the basic features of nonlinear travelling waves propagating in dusty plasmas with relativistic and nonextensive particles. The paper is organized as follows: Section-1 contains the formal introduction; Section-2 contains basic equations governing the plasma model. The KdV and mKdV equations for DEA solitary waves has been derived respectively in Section-3 and Section-4. Results and parametric discussions are made in Section-5, while Section-6 presents a summary of our results.

2. BASIC GOVERNING EQUATIONS

We consider an unmagnetized homogeneous warm dusty plasma system comprising of electrons with weak relativistic effect, $q-$nonextensive ions and static dusts with negative charge. Also, the dust charge number z_d is taken to be constant [51], and their impacts of the dynamics of DEA waves is neglected. Therefore, in such a plasma system the dynamics of nonlinear one-dimensional DEA waves motion is governed by the following unnormalized fluid equations:

$$\frac{\partial N_e}{\partial T} + \frac{\partial}{\partial x}\left(N_e V_e\right) = 0 \tag{1}$$

$$\left(\frac{\partial}{\partial T} + V_e \frac{\partial}{\partial X}\right)(\gamma V_e) + \frac{k_b T_e}{N_e m_e}\frac{\partial N_e}{\partial X} = \frac{e}{m_e}\frac{\partial \Phi}{\partial X} \tag{2}$$

$$\frac{\partial^2 \Phi}{\partial X^2} = 4\pi e\left[N_e + z_d n_{d0} - N_i\right] \tag{3}$$

where N_e, V_e, and Φ are respectively the electron number density , electron fluid velocity and electrostatic potential. To normalize the set of equations (1)-(3), we consider the scaling variables as: $n_e = \frac{N_e}{n_{e0}}$; $n_i = \frac{N_i}{n_{i0}}$; $v_e = \frac{V_e}{C_e}$; $\phi = \frac{e\Phi}{k_b T_e}$; $x = \frac{X}{\lambda_D}$; $t = \frac{T}{\omega_{pe^{-1}}}$, and the normalized form of equations (1)-(3) can be written as

$$\frac{\partial n_e}{\partial t} + \frac{\partial}{\partial x}\left(n_e v_e\right) = 0 \tag{4}$$

$$\left(\frac{\partial}{\partial t} + v_e \frac{\partial}{\partial x}\right)(\gamma v_e) + \frac{1}{n_e}\frac{\partial n_e}{\partial x} = \frac{\partial \phi}{\partial x} \tag{5}$$

$$\frac{\partial^2 \phi}{\partial x^2} = n_e + \mu - \delta n_i \tag{6}$$

Here $C_e = \sqrt{K_B T_e/m_e}$ is the electron acoustic speed; $\omega_{pe} = \sqrt{4\pi n_{e0} e^2/m_e}$ the electron plasma frequency and $\lambda_D = \sqrt{K_B T_e/4\pi n_{e0} e^2}$ the electron Debye length, and $m_e,\ T_e,\ e,\ K_B$ are the electron mass, characteristic electron temperature, electronic charge and the Boltzmann constant. Also, the relativistic factor for electrons $\gamma = \left(\sqrt{1-\frac{v^2}{c^2}}\right)^{-1} \approx 1 + \frac{v^2}{2c^2}$, for weakly relativistic regime, c (normalized with C_e) speed of light. Moreover, we have defined $\mu = z_d n_{d0}/n_{e0}$ and $\delta = n_{i0}/n_{e0} > 1$. The overall charge neutrality condition that is $n_{i0} = n_{e0} + z_d n_{d0}$, gives $\mu = \delta - 1$.

The presence of ion density is assumed through the $q-$nonextensive distribution function [52–54], which is one dimensional equilibrium in nature and given as

$$f(v_i) = C_q \left[1 + (q-1)\left\{\frac{m_i v_i^2}{2T_i} - \frac{e\phi}{T_i}\right\}\right]^{\frac{1}{q-1}} \tag{7}$$

where the normalization constant C_q indicated by

$$C_q = n_{i0}\frac{\Gamma\left(\frac{1}{q-1}\right)}{\Gamma\left(\frac{1}{q-1}-\frac{1}{2}\right)}\sqrt{\frac{m_i(1-q)}{2\pi K_B T_i}}, \quad \text{for} \quad -1 < q < 1$$

$$C_q = n_{i0}\left(\frac{1+q}{2}\right)\frac{\Gamma\left(\frac{1}{q-1}-\frac{1}{2}\right)}{\Gamma\left(\frac{1}{q-1}\right)}\sqrt{\frac{m_i(1-q)}{2\pi K_B T_i}}, \quad \text{for} \quad q > 1$$

Here Γ is the well-known gamma function, the parameter q measures the ion nonextensivity of the system and the remaining parameters or variables maintain their usual meaning. As the gamma function is undefined for negative numbers, so for $q < -1$, the function (7) cannot be normalized, and it is noted that the function (7) is the specific distribution which optimizes the Tsallis nonextensive entropy and, as a result it follows to the laws of thermodynamics. Moreover, the distribution (7) reduces to the standard Maxwell–Boltzmann velocity distribution due to the limiting case $q \to 1$.

Integrating the distribution function (7), the expression for ion number density is obtained as

$$n_i = n_{i0}\left[1 - (q-1)\frac{e\phi}{K_B T_i}\right]^{\frac{1}{q-1}+\frac{1}{2}}$$

Hence, the normalized form of ion number density is

$$n_i = [1 - \sigma(q-1)\phi]^{\frac{q+1}{2(q-1)}} \tag{8}$$

Here, q is a real parameter that is higher than -1 and $\sigma = T_e/T_i$. For $\phi \ll 1$, expanding (8) upto the third order and substitution of (6), gives

$$\frac{\partial^2\phi}{\partial x^2} = n_e - 1 + k_1\phi - k_2\phi^2 + k_3\phi^3 + \ldots \tag{9}$$

where

$$\left.\begin{aligned} k_1 &= \frac{\delta\sigma(1+q)}{2} \\ k_2 &= \frac{\delta\sigma^2(1+q)(3-q)}{8} \\ k_3 &= \frac{\delta\sigma^3(1+q)(3-q)(5-3q)}{48} \end{aligned}\right\} \tag{10}$$

3. THE KDV EQUATION AND ITS SOLUTION

To derive KdV equation for small amplitude DEA solitary wave, the reductive perturbation approach is used. In resent times, reductive perturbation technique becomes very popular to study the nonlinear electrostatic waves of small amplitude limit in the field of plasma. To investigate the DEA solitary waves propagating through KdV equation, stretching and writing the independent variables as

$$\xi = \epsilon^{1/2}(x - Vt)\,, \quad \tau = \epsilon^{3/2}t \tag{11}$$

where ϵ is a small dimensionless parameter and V the phase velocity of DEA waves. And the dependent variables are expanded about the equilibrium states in power series of ϵ as

$$\left.\begin{aligned} n_e &= 1 + \epsilon n_1 + \epsilon^2 n_2 + \epsilon^3 n_3 + \ldots \\ v_e &= v_0 + \epsilon v_1 + \epsilon^2 v_2 + \epsilon^3 v_3 + \ldots \\ \phi &= \epsilon\phi_1 + \epsilon^2\phi_2 + \epsilon^3\phi_3 + \ldots \end{aligned}\right\} \tag{12}$$

Substituting, the transformation (11) and expression (12), into equations (4),(5) and (9), and then collecting the coefficients of lowest order terms in ϵ, and after integration with the boundary conditions: $n_1 = 0,\ v_1 = 0,\ \phi_1 = 0$ at $|\xi| \to \infty$, we obtain the first order terms as

$$\left.\begin{aligned} n_1 &= -k_1\phi_1 \\ v_1 &= -k_1(V - v_0)\phi_1 \end{aligned}\right\} \tag{13}$$

along with the linear phase velocity expression for DEA waves,

$$V = v_0 \pm \sqrt{\frac{1+k_1}{Ak_1}} \tag{14}$$

where $A = 1 + \dfrac{3v_0^2}{2c^2}$. The positive and negative sign respectively refers to the fast and slow DEA mode. Although, we assumed the case of fast DEA mode in our numerical simulations, whereas the slow DEA mode is entirely ignored.

Again, collecting the coefficients of second higher order terms in ϵ, we obtain the subsequent equations

$$-S\frac{\partial n_2}{\partial \xi} + \frac{\partial n_1}{\partial \tau} + \frac{\partial v_2}{\partial \xi} + \frac{\partial (n_1 v_1)}{\partial \xi} = 0 \tag{15}$$

$$-AS\frac{\partial v_2}{\partial \xi} + A\frac{\partial v_1}{\partial \tau} + (A - 2BS)v_1\frac{\partial v_1}{\partial \xi} - ASn_1\frac{\partial v_1}{\partial \xi} + \frac{\partial n_2}{\partial \xi} - \frac{\partial \phi_2}{\partial \xi} - n_1\frac{\partial \phi_1}{\partial \xi} = 0 \tag{16}$$

$$n_2 + k_1\phi_2 - k_2\phi_1^2 - \frac{\partial^2 \phi_1}{\partial \xi^2} = 0 \tag{17}$$

where $S = V - v_0$ and $B = 3v_0/2c^2$. Eliminating the terms n_2 and v_2 from equations (15)-(17) and after utilizing (13) and (14), the KdV equation for first order electrostatic potential $\phi_1 (= \varphi)$ is found as

$$\frac{\partial \varphi}{\partial \tau} + M\varphi\frac{\partial \varphi}{\partial \xi} + N\frac{\partial^3 \varphi}{\partial \xi^3} = 0 \tag{18}$$

with the constants M and N given by

$$M = \frac{1}{2ASk_1}\left[2\left(\frac{k_2}{k_1}\right) - k_1 - AS^2k_1^2 + 2BS^3k_1^2\right] \text{ and } N = \frac{1}{2ASk_1^2} \tag{19}$$

and called respectively nonlinear coefficient and dispersion coefficient of the KdV equation.

Equation (18) is a nonlinear partial differential equation, and is analytically solvable. To determine the stationary solitary wave solutions (18), we take a new transformation $\chi = \xi - C\tau$, where C is wave velocity in the linear χ-space. Using this variable, the KdV equation (18) can be integrated under the boundary condition: $\varphi = 0$, $d\varphi/d\chi = 0$ and $d^2\varphi/d\chi^2 = 0$ as $\chi \to \pm\infty$, to give the solitary wave solution as

$$\varphi = \varphi_0 \operatorname{sech}^2\left(\frac{\chi}{\Delta}\right) \tag{20}$$

where $\varphi_0 = 3C/M$ is the wave amplitude of the DEA soliton and it is proportional to the soliton speed C, and $\Delta = 2\sqrt{N/C}$ is the width of DEA soliton and it is inversely proportional to $\sqrt{C}$.

It reveals from equation (19) that the nonlinear coefficients M depends on the plasma parameters q, σ, δ and the electron relativistic streaming factor v_0/c. We find a compressive DEA solitary waves for $M > 0$, and while rarefactive for $M < 0$. Based on the Fig.-[1], we find a critical composition value of q_c (say) at a given value of parameters q, σ, δ and v_0/c, for which $M \approx 0$. As the nonliearity becomes zero at that critical point/region, as a result the amplitude $\varphi \to \infty$, thus the DEA solitary wave solution has infinite divergence. We can find the expression of q_c, by solving the equation $M = 0$, given in (19) for q and obtained as

$$q_c = \frac{-(a+\delta+1) \pm \sqrt{8a + (\delta+1)^2}}{a} \tag{21}$$

where $a = \sigma\delta^2S^2(A - 2BS)$. In this particular regime, the model is not adequately described by the KdV equation (18). In order to study the propagation properties of DEA solitary waves in the critical point/region, we take the higher order nonlinearity and proceed with modified KdV equation in the following section.

4. THE MODIFIED KDV EQUATION AND ITS SOLUTION

For the purpose of describing the system at or close to the critical nonextensive q_c given in (21), to derive modified KdV (mKdV) equation, for which we consider the same set of expression (9) but with different stretched coordinates as follows:

$$\xi = \epsilon(x - Vt)\ , \quad \tau = \epsilon^3 t \tag{22}$$

Therefore, Substituting (12) and (22) into equations (4),(5) and (9), and proceeding as in section-3, we obtain the same first order terms in ϵ as given in (13) and (14). For second order terms, collecting the coefficients of next higher order of

ϵ and then integrating with the boundary conditions: $n_2 = 0,\ v_2 = 0,\ \phi_2 = 0$ at $|\xi| \to \infty$, we obtain after the use of first order terms as

$$\left.\begin{aligned} n_2 &= k_2\phi_1^2 - k_1\phi_2 \\ v_2 &= S\left[(k_2 - k_1^2)\phi_1^2 - k_1\phi_2\right] \end{aligned}\right\} \tag{23}$$

along with the condition as follows

$$2\left(\frac{k_2}{k_1}\right) - k_1 - AS^2k_1^2 + 2BS^3k_1^2 = 0 \tag{24}$$

Finally, collecting the coefficients of third highest order in ϵ, we find the following equations

$$-S\frac{\partial n_3}{\partial \xi} + \frac{\partial n_1}{\partial \tau} + \frac{\partial v_3}{\partial \xi} + \frac{\partial (n_1 v_2)}{\partial \xi} + \frac{\partial (n_2 v_1)}{\partial \xi} = 0 \tag{25}$$

$$\begin{aligned} -AS\frac{\partial v_3}{\partial \xi} + A\frac{\partial v_1}{\partial \tau} - ASn_1\frac{\partial v_2}{\partial \xi} + A\frac{\partial (v_1 v_2)}{\partial \xi} + An_1v_1\frac{\partial v_1}{\partial \xi} - ASn_2\frac{\partial v_1}{\partial \xi} - 2BS\frac{\partial (v_1 v_2)}{\partial \xi} + \\ 2Bv_1^2\frac{\partial v_1}{\partial \xi} - 2BSn_1v_1\frac{\partial v_1}{\partial \xi} - \frac{3S}{2c^2}v_1^2\frac{\partial v_1}{\partial \xi} - \frac{\partial \phi_3}{\partial \xi} - n_1\frac{\partial \phi_2}{\partial \xi} - n_2\frac{\partial \phi_1}{\partial \xi} + \frac{\partial n_3}{\partial \xi} = 0 \end{aligned} \tag{26}$$

$$n_3 + k_1\phi_3 - 2k_2\phi_1\phi_2 + k_3\phi_1^3 - \frac{\partial^2 \phi_1}{\partial \xi^2} = 0 \tag{27}$$

Eliminating the terms n_3 and v_3 from equations (25)-(27) and making use of the terms from (13), second-order terms from (23) and the relations (14) and (24) as well, we get the following mKdV equation

$$\frac{\partial \psi}{\partial \tau} + M_1\psi^2\frac{\partial \psi}{\partial \xi} + N_1\frac{\partial^3 \psi}{\partial \xi^3} = 0 \tag{28}$$

where, $\phi_1 = \psi,\ N_1 = N$ and the higher order nonlinear coefficient M_1 is given by

$$M_1 = \frac{1}{2ASk_1}\left[6AS^2k_1k_2 - 3AS^2k_1^3 + 6BS^3k_1^3 - 6BS^3k_1k_2 - \frac{3S^4k_1^3}{2c^2} + 3\left(\frac{k_3}{k_1}\right) + k_2\right] \tag{29}$$

Now, using the same transformation and proceeding with the same procedure as given in section[3], we can determine the solitary wave solution of the mKdV equation(28) as

$$\psi = \psi_0 \operatorname{sech}\left(\frac{\chi}{W}\right) \tag{30}$$

Where $\psi_0 = \sqrt{6C/M_1}$ is amplitude and $W = \sqrt{N/C}$, the width of the of DEA solitary waves represented by the mKdV equation(28) and C is the velocity of soliton.

5. RESULTS AND DISCUSSIONS

In this modal of dusty plasma, the dynamical properties of small amplitude DEA solitary wave have been studied in the context of relativistic electrons and nonextensive distributed ions. The influences of various plasma parameters namely, the ion-to-electron number density ratio δ, relativistic electron streaming factor v_0/c and the degree of ion nonextensive parameter q on the DEA solitary waves are numerically analyzed. Throughout the graphical analysis, we have looked at the case for $\sigma(= T_e/T_i) = 1$.

The ion nonextensive parameter q have a notable effect over the nonlinear coefficient M and dispersion coefficient N of KdV equation. Fig-[1] shows the sketch of M for two scenarios, that is for distinct values of $\delta(= 1.1,\ 1.3,\ 1.5,\ 1.7)$ and $v_0/c(= 0.0,\ 0.3,\ 0.6,\ 0.9)$, as q increases in the range $-1 < q < 3$. It is clear from both Fig-[1a] and Fig-[1b] that the nonlinear coefficient M can have values that are both positive and negative, while the dispersion coefficient N is observed to take always positive values (figures not included). This change of signs of the nonlinearity indicates the existence of two kind of DEA solitary waves having a positive and a negative potentials. It is traced out that $M \approx 0$ at $q = q_c$, whereas $M > 0$ in the range $-1 < q < q_c$, which is the parametric domain where compressive DEA solitons occur. Again, $M < 0$ in the range $q_c < q < 3$, which is the parametric domain where rarefactive DEA solitons occur. Therefore, in the current KdV model of plasma, both compressive and rarefactive DEA solitary structures can exist.

Now, we illustrate how the various physical parameters influences over the behavior of propagating DEA solitary waves. It is seen from Fig.-[2a] that, when the ratio of ion-to-electron number density δ increases with fixed $q = 0.5,\ v_0/c = 0.3$ and $C = 0.005$, the rarefactive DEA solitons, and both its amplitude and width of the negative potential DEA solitary waves decreases. Here, it can predicted that the structure of rarefactive DEA solitary waves is broader when

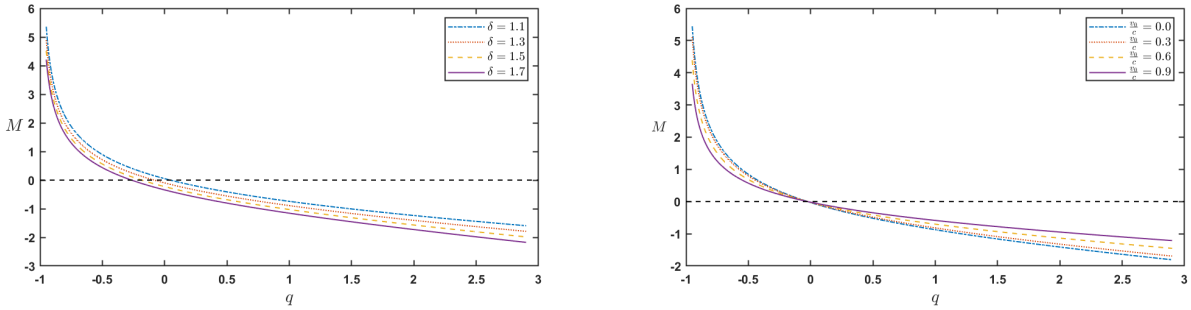

(a) **(b)**

Figure 1. **(a)** The variation of M with q for different δ and $\frac{v_0}{c} = 0.3$ and **(b)** The variation of M with q for different $\frac{v_0}{c}$ and $\delta = 1.2$. With $\sigma = 1$.

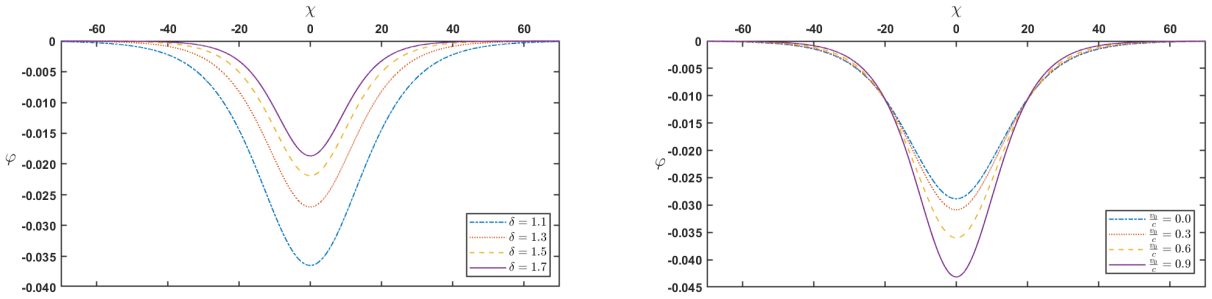

(a) **(b)**

Figure 2. **(a)** The variation of KdV solitons for different δ with $\frac{v_0}{c} = 0.3$ and **(b)** The variation of KdV solitons for different $\frac{v_0}{c}$ with $\delta = 1.2$. In both the panels, $q = 0.5(> q_c)$, $\sigma = 1$ and $C = 0.005$.

the population of ions and electrons are almost same in the present plasma. In Fig.-[2b], it is observed that when relativistic electron streaming factor v_0/c increases for fixed $q = 0.5$, $\delta = 1.2$ and $C = 0.005$, the DEA soliton is rarefactive and the amplitude (width) of the negative potential DEA solitary waves increases (decreases). That means the energy of the propagating DEA solitons enhances with increasing values of relativistic electron streaming factor in the present plasma.

For fixed parameters as $\delta = 1.2$, $v_0/c = 0.3$ and $C = 0.005$, how the ion nonextensive parameter q effects on the propagating DEA solitary waves are shown in Fig.-[3]. The soliton type is observed to have changed from compressive to rarefactive at q depending on δ and v_0/c. With rising values of $q < q_c$, the soliton is compressive (Fig.-[3a]) and amplitude of positive potential DEA solitary waves increases notably while width decreases slightly. Conversely, for increasing values of $q > q_c$, the soliton is rarefactive (Fig.-[3b]) and decreases the pulse of negative potential DEA solitary waves in both amplitude and width. Here, for $\delta = 1.2$, $v_0/c = 0.3$ and $q = 0.5$, we find from (18) that $q_c \approx 0.07$. Additionally, it is clear that $M \approx 0$ at $q \approx q_c$, as a result, the KdV equation fails and the system can not be described.

The change of second order nonlinear coefficient M_1 of mKdV equation (25) against q and v_0/c for distinct values of δ have been shown in Fig.-[4] at q_c. In both the cases the value of M_1 is found to be positive, which indicates only compressive mKdV solitons can propagates at or near the critical point q_c in the present plasma model. Fig.-[5] shows the graph of solitary wave potential ψ of mKdV equation against the linear parameters χ, for various q, δ and v_0/c. It

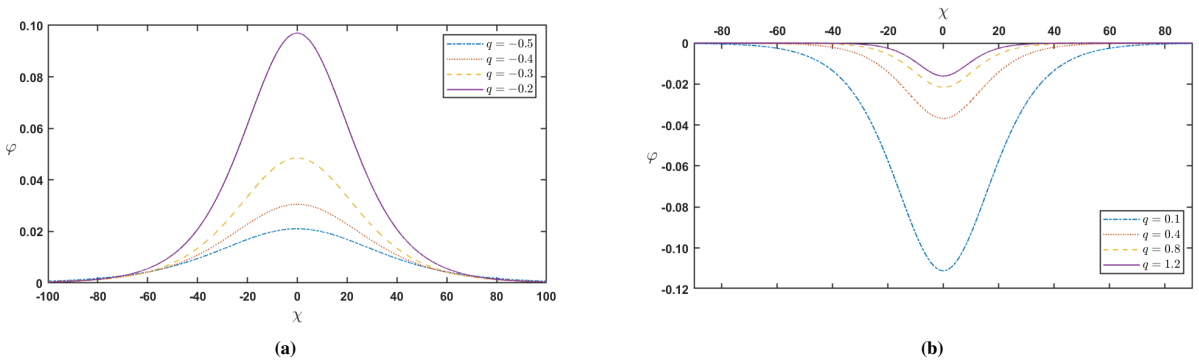

(a) **(b)**

Figure 3. The variation of KdV solitons **(a)** for different $q < q_c$ and **(b)** for different $q > q_c$. where $\frac{v_0}{c} = 0.3$, $\sigma = 1$, $\delta = 1.2$ and $C = 0.005$.

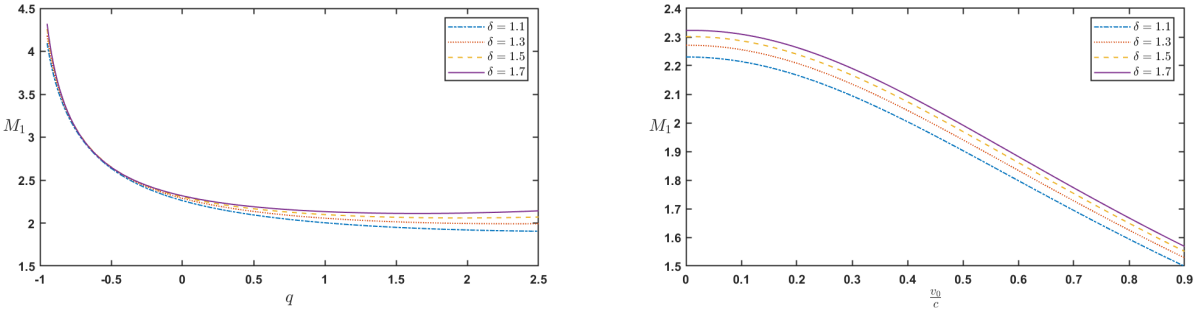

(a) **(b)**

Figure 4. The variation of higher order nonlinear term M_1 **(a)** with q, for $\frac{v_0}{c} = 0.3$ and different δ and **(b)** with $\frac{v_0}{c}$ for $q = 0.5$ and different δ at q_c and $\sigma = 1$.

is evident from Fig.-[5a] that, when the ratio of ion-to-electron number density δ increases with fixed other parameters, the amplitude as well as width of the compressive modified DEA solitary waves to decrease. Moreover, rising value of relativistic electron streaming factor v_0/c and fixed other parameters, enhance the amplitude while decreases the width of the compressive modified DEA solitary waves as shown in Fig.-[5b]. The change of modified DEA solitary wave pulses are shown in Fig.-[6] for distinct values of ion nonextensive parameter q, with fixed other parameters. It is seen that the amplitude of compressive DEA solitary waves increases while the width is not notably changes by the increasing values of q.

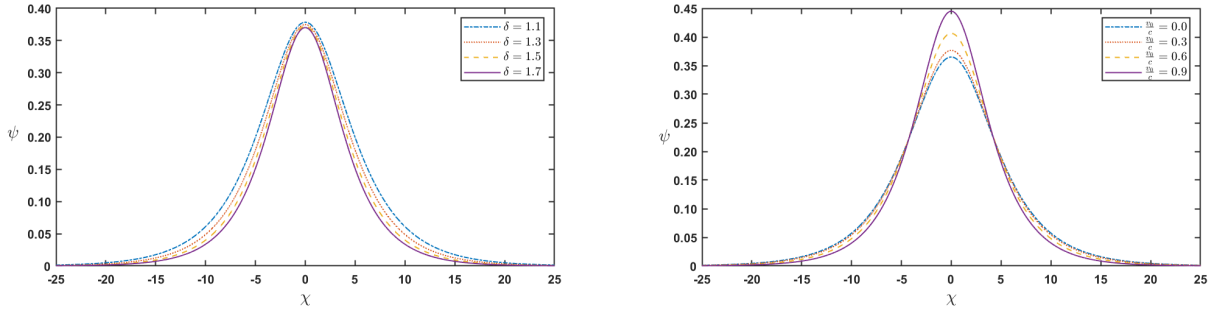

(a) **(b)**

Figure 5. The variation of mKdV solitons **(a)** for different δ with $\frac{v_0}{c} = 0.3$; and **(b)** for different $\frac{v_0}{c}$ with $\delta = 1.2$; at q_c. where $q = 0.5$, $\sigma = 1$, $C = 0.05$.

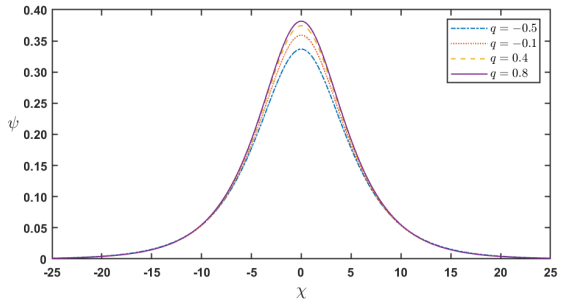

Figure 6. The variation of mKdV solitons for different q with $\delta = 1.2$, $\frac{v_0}{c} = 0.3$ at q_c. where $\sigma = 1$, $C = 0.05$.

6. CONCLUSION

In this manuscript, we have numerically analyzed the dynamical properties of the propagation of small amplitude DEA solitary waves in an unmagnetized plasma model, consisting of relativistic electrons, nonextensive ions and negatively charged static dust grains. Both the KdV and mKdV equations are determined using the reductive perturbation technique, and their solitary wave solutions are obtained. The effects of physical parameters such as ion-to-electron number density ratio δ, relativistic electron streaming factor v_0/c, and ion nonextensive parameter q over DEA solitary wave potentials

represented by the KdV and mKdV equations are discussed numerically in the case when electron-to-ion temperature ratio $\sigma = 1$. The outcomes that have been noticed in this study can be contracted as follows:

1. In the present plasma model, two distinct sorts of wave modes are found to exist, namely fast DEA acoustic mode and slow acoustic modes. But only fast DEA modes are considered in the extraction of KdV and mKdV equations.
2. First order nonlinear coefficient M in the KdV equation can be a positive and a negative quantity, while the second order nonlinear coefficient M_1 of mKdV equation is a positive quantity, depending on the plasma parametric values. Therefore, there exist both compressive and rarefactive KdV solitons in the present plasma system.
3. The change in the soliton types from compressive to rarefactive or vice-versa is predicting mainly through the variation of ion nonextensive parameter q, depending on δ and v_0/c. It is seen that compressive and rarefactive solitons show the range of ion nonextensivity $-1 < q < q_c$ and $q_c < q < 3$ respectively.
4. At the critical q_c, we consider a second order nonlinearity and determine mKdV equation. Only compressive DEA solitary wave structures are feasible in present plasma system.
5. The increasing of ion-to-electron number density ratio δ in the plasma, lead to decrease both the amplitude and width of the pulses of the propagating DEA solitons.
6. Moreover, with the rising values of relativistic electron streaming factor v_0/c, enhances the energies of the propagating DEA solitons.

Finally, we draw the conclusion that our present theoretical findings should be useful for better understanding the dynamical nature of small but finite amplitude DEA solitons in both astrophysical and space contexts as well as in future laboratory investigations in which the present plasma model are occurred.

ORCID

Rafia Khanam, https://orcid.org/0009-0006-8648-0827; **Satyendra Nath Barman**, https://orcid.org/0000-0003-1136-8364; **Muktarul Rahman**, https://orcid.org/0009-0000-3523-8412

REFERENCES

[1] S. Bansal, and M. Aggarwal, "Non-planar electron-acoustic waves with hybrid Cairns–Tsallis distribution," Pramana – J. Phys. **92**, 49 (2019). https://doi.org/10.1007/s12043-018-1713-z

[2] H.R. Pakzad, "Effect of q-nonextensive distribution of electrons on electron acoustic solitons," Astrophys Space Science, **333**, 247–255 (2011). https://doi.org/10.1007/s10509-010-0570-0

[3] H. Demiray, and C. Bayındır, "A note on the cylindrical solitary waves in an electron-acoustic plasma with vortex electron distribution," Physics of Plasmas, **22**, 092105 (2015). https://doi.org/10.1063/1.4929863

[4] P. Chatterjee, G. Mondal, and C.S. Wong, "Electron acoustic dressed soliton in quantum plasma," Indian J. Phys. **87**(8), 827–834 (2013). https://doi.org/10.1007/s12648-013-0292-6

[5] J. Goswami, J. Sarkar, S. Chandra, and B. Ghosh, "Amplitude-modulated electron-acoustic waves with bipolar ions and kappa-distributed positrons and warm electrons," Pramana – J. Phys. **95**, 54 (2021). https://doi.org/10.1007/s12043-021-02085-1

[6] S. Chandra, and B. Ghosh, "Modulational instability of electron-acoustic waves in relativistically degenerate quantum plasma," Astrophysics and Space Science, **342**, 417–424 (2012). https://doi.org/10.1007/s10509-012-1186-3

[7] S. Roy, S. Saha, S. Raut, and A.N. Das, "Studies on the effect of kinematic viscosity on electron-acoustic cylindrical and spherical solitary waves in a plasma with trapped electrons," Journal of Applied Mathematics and Computational Mechanics, **20**(2), 65-76 (2021). https://doi.org/10.17512/jamcm.2021.2.06

[8] M. Rosenberg, and G. Kalman, "Dust acoustic waves in strongly coupled dusty plasmas," Physical Rrview E, **56**(6), (1997). https://doi.org/10.1103/PhysRevE.56.7166

[9] H.J. Dehingia, and P.N. Deka, "Structural variations of dust acoustic solitary waves (DASWs) propagating in an inhomogeneous plasma," East European Journal of Physics, (1), 19-27 (2023). https://doi.org/10.26565/2312-4334-2023-1-02

[10] N.N. Rao, P.K. Shukla, and M.Y. Yu, "Dust-acoustic waves in dusty plasmas," Planetary and space science, **38**(4), 543-546 (1990). https://doi.org/10.1016/0032-0633(90)90147-I

[11] A. Barkan, R.L. Merlino, and N. D'angelo, "Laboratory observation of the dust-acoustic wave mode," Physics of Plasmas, **2**(10), 3563-3565 (1995). https://doi.org/10.1063/1.871121

[12] N. D'Angelo, "Coulomb solids and low-frequency fluctuations in RF dusty plasmas," Journal of Physics D: Applied Physics, **28**(5), 1009 (1995). https://doi.org/10.1088/0022-3727/28/5/024

[13] R. Jahangir, and W. Masood, "Interaction of electron acoustic waves in the presence of superthermal electrons in terrestrial magnetosphere," Physics of Plasmas, **27**, 042105 (2020). https://doi.org/10.1063/1.5143400

[14] A.M. El-Hanbaly, E.K.El-Shewy, A. Elgarayhi, and A.I. Kassem, "Propagation of Electron Acoustic Soliton, Periodic and Shock Waves in Dissipative Plasma with a q-Nonextensive Electron Velocity Distribution," Communications in Theoretical Physics, **64**(5), 529–536 (2015). https://doi.org/10.1088/0253-6102/64/5/529

[15] S. Chandra, and B. Ghosh, "Modulational instability of electron-acoustic waves in relativistically degenerate quantum plasma," Astrophys. Space Sci. **342**, 417–424 (2012). https://doi.org/10.1007/s10509-012-1186-3

[16] H. Asgari, S.V. Muniandy, and C.S. Wong, "Dust-acoustic solitary waves in dusty plasmas with non-thermal ions," Physics of Plasmas, **20**, 023705 (2013). https://doi.org/10.1063/1.4793743

[17] A.M. El-Hanbaly, E.K. El-Shewy, A.I. Kassem, and H.F. Darweesh, "Nonlinear Electron Acoustic Waves in Dissipative Plasma with Superthermal Electrons," Applied Physics Research, **8**(1), 1916-9639 (2016). http://dx.doi.org/10.5539/apr.v8n1p64

[18] S.V. Singh, and G.S. Lakhina, "Generation of electron-acoustic waves in the magnetosphere," Planetary and Space Science, 49(1), 107-114 (2001). https://doi.org/10.1016/S0032-0633(00)00126-4

[19] S. Bansal, T.S. Gill, and M. Aggarwal, "Oblique modulation of electron acoustic waves in nonextensive plasm," Physics of Plasmas, **26**, 072116 (2019). https://doi.org/10.1063/1.5094245

[20] A.A. Mamun, "Dust–electron-acoustic shock waves due to dust charge fluctuation," Physics Letters A, **372**, 4610–4613 (2008). https://doi.org/10.1016/j.physleta.2008.04.038

[21] R. Jahangir, W. Masood, and H. Rizvi, "Interaction of electron acoustic solitons in auroral region for an electron beam plasma system," Frontiers in Astronomy and Space Sciences, **9**, 1-13 (2022). https://doi.org/10.3389/fspas.2022.978314

[22] S. Das, and D.C. Das, "Higher-order nonlinear dust ion acoustic (DIA) solitary waves in plasmas with weak relativistic effects in electrons and ions," The European Physical Journal D, **77**, 39 (2023). https://doi.org/10.1140/epjd/s10053-023-00621-9

[23] S. Das, "Weak Relativistic Effect in the Formation of Ion-Acoustic Solitary Waves in Dusty Plasma," IEEE Transactions on Plasma Science, **50**(7), 2225-2229 (2022). https://doi.org/10.1109/TPS.2022.3181149

[24] T.F. Rahman, S. Tarofder, M.M. Orani, J. Akter, and A.A. Mamun, "(3+ 1)-dimensional cylindrical dust ion-acoustic solitary waves in dusty plasma," Results in Physics, **53**, 106907 (2023). https://doi.org/10.1016/j.rinp.2023.106907

[25] S. Benaiche, M. Bacha, A. Merriche, and R. Amour, "Effect of Tsallis–Gurevich distributed ions on nonlinear dust-acoustic oscillations in collisionless nonextensive plasma," Contributions to Plasma Physics, **63**(2), e202200132 (2023). https://doi.org/10.1002/ctpp.202200132

[26] R. Amour, and M. Tribeche, "Semi-analytical study of variable charge dust acoustic solitary waves in a dusty plasma with a q-nonextensive ion velocity distribution," Communications in Nonlinear Science and Numerical Simulation, **16**(9), 3533-3539 (2011). https://doi.org/10.1016/j.cnsns.2010.12.037

[27] M. Tribeche, and A. Merriche, "Nonextensive dust-acoustic solitary waves," Physics of Plasmas, **18**(3), 034502 (2011). https://doi.org/10.1063/1.3561789.

[28] S. Tarofder, A. Mannan, and A.A. Mamun, "Cylindrical Three Dimensional Dust–Ion–Acoustic Solitary Waves in Nonthermal Plasmas," Plasma Physics Reports, **49**, 1014–1022 (2023). https://doi.org/10.1134/S1063780X23600354

[29] S. Bhowmick, and B. Sahu, "Propagation properties of dust-electron-acoustic waves in weakly magnetized dusty nonthermal plasmas," Contributions to Plasma Physics, **61**(1), e202000091 (2021). https://doi.org/10.1002/ctpp.202000091

[30] B.C. Kalita, and S. Das, "Dust ion acoustic (DIA) solitary waves in plasmas with weak relativistic effects in electrons and ions," Astrophys. Space Sci. **352**, 585–592 (2014). https://doi.org/10.1007/s10509-014-1954-3

[31] B.C. Kalita, and M. Deka, "Investigation of solitary waves in warm plasma for smaller order relativistic effects with variable pressures and inertia of electrons," Astrophys. Space Sci. **343**(2), 609–614 (2013). https://doi.org/10.1007/s10509-012-1261-9

[32] R. Das, and K.C. Nath, "Modified Korteweg-de Vries solitons on dust ion acoustic waves in a warm plasma with electrons' drift motion," Advances and Applications in Fluid Mechanics, **19**(3), 541-553 (2016). http://dx.doi.org/10.17654/FM019030541

[33] B.C. Kalita, R. Das, and H.K. Sarmah, "Weakly relativistic solitons in a magnetized ion-beam plasma in presence of electron inertia," Physics of Plasmas, **18**(1), 012304 (2011). https://doi.org/10.1063/1.3536428

[34] B.C. Kalita, and M. Choudhury, "The role of unidirected relativistic electrons with inertia in the formation of weakly relativistic ion acoustic solitons in magnetized plasma," Astrophys. Space Sci. 346, 375–382 (2013). https://doi.org/10.1007/s10509-013-1468-4

[35] B.C. Kalita, and R. Kalita, "Implicit role of Cairns distributed ions and weak relativistic effects of electrons in the formation of dust acoustic waves in plasma," Journal of Plasma Physics, **82**(2), 905820201 (2016). https://doi.org/10.1017/S0022377816000167

[36] B.C. Kalita, and S. Das, "Comparative study of dust ion acoustic Korteweg–de Vries and modified Korteweg–de Vries solitons in dusty plasmas with variable temperatures," Journal of Plasma Physics, **83**(5), 905830502 (2017). https://doi.org/10.1017/S0022377817000721

[37] A. Renyi, "On a new axiomatic theory of probability," Acta Mathematica Academiae Scientiarum Hungarica, **6**, 285-335 (1955). https://doi.org/10.1007/BF02024393

[38] C. Tsallis, "Possible generalization of Boltzmann-Gibbs statistics," Journal of statistical physics, **52**, 479-487 (1988). https://doi.org/10.1007/BF01016429

[39] U.S. Kumar, A. Saha, and P. Chatterjee, "Bifurcations of dust ion acoustic travelling waves in a magnetized dusty plasma with a q-nonextensive electron velocity distribution," Physics of Plasmas, **20**(2), 022111 (2013). https://doi.org/10.1063/1.4791660

[40] A.A. Mahmoud, E.M. Abulwafa, A.A.F. Al-Araby, and A.M. Elhanbaly, "Plasma parameters effects on dust acoustic solitary waves in dusty plasmas of four components," Advances in Mathematical Physics, **1**, 7935317 (2018). https://doi.org/10.1155/2018/7935317

[41] F. Araghi, S. Miraboutalebi, and D. Dorranian, "Effect of variable dust size, charge and mass on dust acoustic solitary waves in nonextensive magnetized plasma," Indian Journal of Physics, **94**, 547-554 (2020). https://doi.org/10.1007/s12648-019-01488-6

[42] P. Eslami, M. Mottaghizadeh, and H.R. Pakzad, "Nonplanar dust acoustic solitary waves in dusty plasmas with ions and electrons following a q-nonextensive distribution," Physics of Plasmas, **18**(10), 102303 (2011). https://doi.org/10.1063/1.3642639

[43] A. Saha, and P. Chatterjee, "Propagation and interaction of dust acoustic multi-soliton in dusty plasmas with q-nonextensive electrons and ions," Astrophysics and Space Science, **353**, 169-177 (2014). https://doi.org/10.1007/S10509-014-2028-2

[44] F.J. Lin, Z.H. Chen, X.Q. Li, J.J. Liao, and Z. Yun, "Generation and evolution of magnetic field in the relativistic plasma following q-nonextensive distribution," Physics of Plasmas, **24**(2), 022120 (2017). https://doi.org/10.1063/1.4976981

[45] M. Rahman, and S.N. Barman, "Existence of Small Amplitude KDV and MKDV Solitons in a Magnetized Dusty Plasma with $q-$Nonextensive Distributed Electrons," East European Journal of Physics, (2), 74-89 (2024). https://doi.org/10.26565/2312-4334-2024-2-06

[46] U.N, Ghosh, P. Chatterjee, and S.K. Kundu, "The effect of q-distributed ions during the head-on collision of dust acoustic solitary waves," Astrophysics and Space Science, **339**, 255–260 (2012). https://doi.org/10.1007/s10509-012-1009-6

[47] W.F. El Taibany, and M. Tribeche, "Nonlinear ion-acoustic solitary waves in electronegative plasmas with electrons featuring Tsallis distribution," Physics of Plasmas, **19**(2), (2012). https://doi.org/10.1063/1.3684232

[48] J.W. Dai, X.C. Chen, and X.Q. Li, "Dust ion acoustic instability with q-distribution in nonextensive statistics," Astrophysics and Space Science, **346**, 183–190 (2013). https://doi.org/10.1007/s10509-013-1440-3

[49] E.l. Awady, and W.M. Moslem, "On a plasma having nonextensive electrons and positrons: Rogue and solitary wave propagation," Phys. plasmas, **18**, 082306 (2011). https://doi.org/10.1063/1.3620411

[50] R. Amour, and M. Tribeche, "Collisionless damping of dust-acoustic waves in a charge varying dusty plasma with nonextensive ions," Physics of Plasmas, **21**(12), 123709 (2014). https://doi.org/10.1063/1.4903208

[51] P.K. Shukla, and A.A. Mamun, *Introduction to dusty plasma physics*, (CRC press, 2015). https://doi.org/10.1201/9781420034103

[52] R. Silva Jr., A.R. Plastino, and J.A.S. Lima, "A Maxwellian path to the q-nonextensive velocity distribution function," Physics Letters A, **249**(5-6), 401-408 (1998). https://doi.org/10.1016/S0375-9601(98)00710-5

[53] H.R. Pakzad, "Effect of q-nonextensive electrons on electron acoustic solitons," Physica Scripta, **83**(1), 015505 (2011). https://doi.org/10.1088/0031-8949/83/01/015505

[54] P. Chatterjee, K. Roy, and U.N. Ghosh, *Waves and wave interactions in plasmas*, (World Scientific Publishing Co. Pte. Ltd., 2022).

РЕЛЯТИВІСТСЬКИЙ ВПЛИВ НА ПИЛОВО-ЕЛЕКТРОННО-АКУСТИЧНІ САМІТНІ ХВИЛІ В НЕНАМАГНІЧЕНІЙ ПЛАЗМІ З НЕЕКСТЕНСИВНИМИ ІОНАМИ

Рафія Ханам[a], **Сатьендра Натх Барман**[b], **Муктарул Рахман**[a]

[a] *Департамент математики, Університет Гаухаті, Гувахаті-781014, Ассам, Індія*

[b] *В. Бороа коледж, Гувахаті, Ассам, Індія*

Теоретично досліджено нелінійні властивості пилово-електронно-акустичних (DEA) одиночних хвиль та поведінку їх поширення в моделі ненамагніченої релятивістської плазми. Така плазма складається із слаборелятивістських електронів, невеликих розподілених іонів і негативно заряджених нерухомих частинок пилу. Виходячи з набору односпрямованих рівнянь рідини для електронів і неекстенсивного розподілу для іонів з рівнянням Пуассона, рівняння Кортевега-де Фріза (KdV) і модифіковані рівняння KdV (mKdV) визначаються за допомогою методу редуктивного збурення та їх солітонних рішень, отриманих таким чином, для аналізу режиму існування та основних характеристик солітонів DEA малої амплітуди. Детально розглянуто вплив фізичних параметрів, а саме співвідношення густини іонів до електронної кількості (δ), релятивістського коефіцієнта потоку (v_0/c) та параметра неекстенсивності іонів (q) на динаміку солітарних утворень. Результат показує існування як стислих, так і розріджених солітонів DEA KdV і лише стиснутих солітонів DEA mKdV в діапазоні $-1 < q < 3$, з різними δ і v_0/c у плазмі. Крім того, у статті чисельно проаналізовано вплив усіх фізичних параметрів на поширення одиночних хвиль DEA, що відповідають рівнянням KdV та mKdV. Результати цього дослідження можуть допомогти прояснити основні характеристики нелінійних або нелінійних біжучих хвиль, що поширюються як у лабораторній, так і в космічній плазмі, а також у астрофізичному плазмовому середовищі.

Ключові слова: *пило-електронно-акустична одиночна хвиля; рівняння KdV і mKdV; техніка відновного збурення; q-неекстенсивні іони; релятивістська плазма*